Development of the X-ray Camera System for NASA's OGRE Sounding Rocket

Thesis

Development of the X-ray camera system for NASA's OGRE Sounding Rocket

Thesis submitted for the degree of

Master of Philosophy

at The Open University

February 2020

by

Matthew Richard Francis Lewis

Centre for Electronic Imaging

Discipline of Space Instrumentation

School of Physical Sciences

Development of the X-ray camera system for NASA's OGRE Sounding Rocket

Matthew Lewis

Abstract

This thesis discusses the developments of the EM-CCD camera system for the Off-plane Grating Rocket Experiment, or OGRE mission. The key science accomplishments look at the characterisation of devices of the same architecture as those to be used on the mission flight, a model of the complete project payload to determine its mission effectiveness, and an event processing system designed to find events within the images acquired as well as methods to identify events of interest. Chapters 1-4 focus on the backgrounds of x-ray spectroscopy and the OGRE project detailing knowledge required for understanding the work carried out. As the model created is based on the theories and fundamental science behind the OGRE system, this section, chapter 5, is before the experimental set-up discussed in chapter 6. The model based on ideal scenarios highlighted a need to restructure the mission payload as the initial design failed to reach the minimum mission requirements unless changes were implemented. These suggestions were passed on and design changes implemented based on these findings. Chapter 7 details the characterisation of the CCD207-10, and EM-CCD similar to the flight detectors for the project, showing the standard format for incident X-rays, as well as finding offsets present in the device and looking at other significant factors which any affect observations such as dark current, giving confidence the flight devices will operate satisfactorily. The event processing is discussed in chapter 8 with comparisons of observations for X-rays from two different sources with methods of identifying the source based on the observed signal looked at.

Declaration

I hereby declare that no part of this thesis has been previously submitted to this, or any other, university as part of the requirement for a higher degree. The work described herein was conducted solely by the undersigned except for those colleagues and other workers acknowledged in the text.

Dedication

To my mother, father, and my sister

Acknowledgements

There are a great number of people I would like to acknowledge for their help, support, and much needed company throughout the duration of this thesis.

Thanks to my supervisors Matthew Soman, Andrew Holland, Monica Grady, and Neil Murray for their support in the projects progression and for helping me with a new technological area.

Thanks to all the former and current CEI members. Firstly, to the fellow PhD students Alice Dunford, Anton Lindley-Decaire, Daniel-Dee Lofthouse-Smith, James Ivory, Chris Davis, Tom Buggey, Harry Fox, Joseph Rushton, and Daniel Weatherill for the support, laughs, encouragement and for sharing the journey with me. Thanks to the staff, Ben Dryer, Chiaki Crews, Edgar Allanwood, Nathan Bush, David Hall, Oliver Hetherington, Julian Heymes, Michael Holland, Jonathan Keelan, Steven Parson, George Randall, Jesper Skottfelt, Konstantin Stefanov, Philippa Smith, and Jason Gow for the support over the years.

Thanks also to everyone involved with the DPS House Band for the great way to pick up my creative side again and for giving me the confidence to rock out in front of people! Also, to the Friday drinks crew for providing a nice social event to look forward to at the end of each week. I would also like to thank Candice Bedford, Andy Davies, and Ben Rozitis for helping make our year of running Hooke Soc a great one. I would also like to thank Alexandra Loupas and Roy Adkin for the many hilarious conversations as well as the support I have needed.

Thanks to the team at Penn State University, James Tutt, Randall McEntaffer, Ted Schultz, Drew, Ben Jammin', and everyone else for the technical support and for making me feel like one of the team as soon as I arrived. A massive thanks to James and Helen for having me for several weeks.

Thanks to David Burt and David Lumb for their omniscient knowledge on anything I have ever enquired about and doing so in such a useful and friendly manner.

I would also like to thank the Science and Technology Facilities Council for funding this project, XCAM Ltd for their assistance with the camera system and for funding this project, and Teledyne e2v for providing the EM-CCDs used throughout this project.

Finally I would like to thank my mother, father, and sister, as well as my friends for being there to pick me up when I was at me lowest and for helping me see this through to the end when I had lost sight of the finish and beyond.

Table of Contents

1 Introduction

1.1 X-ray astronomy and spectroscopy

Astronomical observations have occurred for millennia using visible light with William Herschel's discovery of infrared in 1800 leading to more regions of the electromagnetic spectrum being found and eventually used for astronomical observations. However, there was one area which took considerably longer to create a method of observation for. X-ray mania took the medical world by storm in 1896 when it was discovered that they passed through bodies allowing observations of potentially broken bones (Stanton 1896). But this posed a question to potential astronomers, how could X-rays be observed when they pass through the usual observational instrumentation? It was also found that X-rays were heavily absorbed by the Earth's atmosphere highly limiting astronomical X-ray observations from the ground.

The late 1920s saw X-ray experiment proposals and it was not until 1948 that experimental setups were being launched above the atmosphere on-board rockets (Keller 1995). In 1962, the first stellar X-rays were detected from outside of our solar system by a sounding rocket (Giacconi, Nobel Lecture: The dawn of x-ray astronomy 2003). 1978 saw the first fully imaging X-ray telescope launched into space, the Einstein Observatory. This utilised a Wolter type system, the same concept as that commonly used today (Giacconi 1980).

With vast advancements in many areas of technology over the past 60 years, the field of X-ray astronomy has grown considerably, however there are still a great number of observations astronomers hope to make, many of which could be done via X-ray observations. These new technologies need to be refined until they can be used for large scale missions and so tests of increasing complexity allow confidence in these technologies to be built up until they become the go to means of observation.

The Off-plane Grating Rocket Experiment, or OGRE, is one these tests. Building on the advancements seen in X-ray astronomy and pushing the limits of what we can achieve with the technology available in a new manner. The Wolter concept has been improved upon, with greater imaging areas, improved reflectivity, and high accuracy in shaping during manufacture. This has been combined with a spectrometer designed to provide the highest resolution X-ray spectrum seen to date of a far stellar source.

Finally, there is the X-ray camera system, the key part which makes all the manipulation of the target photons worthwhile and into a physical observation. This EM-CCD (Electron Multiplying Charge Coupled Device) powered camera system should read out the photons generated by X-rays which are incident upon its surface to a high degree of accuracy. Whilst Wolter telescopes and spectrometers have been used for astronomical observations, EM-CCDs have not yet been used in this field but are an enticing technology for future use with other experiments being carried out to check their suitability for the harsh environment of space.

1.2 Research goals

The main goal of this thesis is to determine the suitability of the EM-CCD for use in the OGRE project and to optimise its capabilities for the successful observations of the soft X-rays from Capella during the mission.

The research goal was achieved via the laboratory testing of the CCD207-10 utilising X-ray sources to investigate the system's properties and determine the ideal operating conditions of the camera system to best aid the project in meeting its success criteria. The experiments in the lab were conducted with devices different to the final flight detectors (CCD207-10's used instead of the final CCD207-40's) and outside the 600 eV – 1200 eV desired energy band, however outcomes are still reflective of the camera's suitability of use in this project due to the high degrees of similarity in the device structures.

A second study into the camera's place in the system originally intended to give a greater idea of the capabilities of each section of the whole OGRE telescope and to estimate the resultant spectrum that could be observed after the flight. A model simulation of the system's design specification, including the optical modules, diffraction gratings and the EM-CCD camera system. This allowed for a greater idea of the minimal capabilities required of the camera system in terms of the expected observations after any event photons had passed through the other key components of the OGRE payload.

A third study into how to determine the locations of X-ray events automatically as well as methods into characterising their sources was also looked at with work carried out using an iron-55 X-ray source and a strontium-90 source. These event detection algorithms need to be capable of operating to a high degree of accuracy in a short time frame to be used on the flight camera during the mission to allow for a data string to be telemetered to the ground allowing the status of the mission to be monitored and any changes implemented should complications arise.

The optimisation of this camera system should allow for a successful project upon launch, paving the way for further advancements in the field of X-ray astronomy leading to further major discoveries which will go on to captivate academics and future researchers.

1.3 Thesis Organisation

This thesis is split into 9 chapters including this introductory chapter. The earlier chapters (chapters 2 to 4) detail the background and key understandings needed. Chapter 2 looks at the history of X-ray astronomy and spectroscopy detailing the basics of this area of research. The sources of X-rays observed in astronomy are discussed with different designs enabling their observations and their implementation into previous missions used to give an idea of how the key technologies in the field have changed over time. This includes satellite missions as well as some prior sounding rocket test flights.

Chapter 3 focuses on the OGRE project itself and highlights the mission's key aims which may encourage the use of the key technologies in future missions. This section gives a background of these key technologies; the optics modules, the diffraction gratings and the EM-CCD camera system, and the reasons they were chosen for use in an X-ray spectrometry mission. This section focuses on the initial designs of the OGRE prototype which shaped the earlier approaches taken in the duration the preparation of this thesis.

Chapter 4 discusses the theory behind CCDs and EM-CCDs allowing an understanding of their use, operation and fundamental knowledge which is required for the later sections of this thesis. The chapter first begins by focusing on the Charge Coupled Device and its structure and abilities of transferring an incident photon into an observable image. The noise sources that are present within CCDs are also discussed. Once this underlying knowledge of CCDs is concluded, the EM-CCD is discussed as this adds to the basic principles of the CCD, allowing a simpler comparison of the reasons these devices were chosen for use in OGRE.

Chapter 5 is the first chapter demonstrating my original work on a model of the OGRE payload that I created to determine an ideal output spectrum. Data from Chandra's observation of the Capella system was fed into this model to determine how the optics module, diffraction gratings, and the EM-CCD camera system of OGRE would affect the number of observable X-rays. An addition is made to this model in the form of an optical-blocking filter which had not been decided upon at the time but was deemed a necessary addition to the system to allow for observations of soft X-rays. The results are shown and alternative variants to the design discussed to allow for an optimal mission launch. Conclusions from the studies presented in this chapter resulted in design changes to the instrument to improve the effective area and increase the number of expected photons to reach the sensors in the camera system.

Chapter 6 shows the experimental setups used for the duration of this work. The capabilities of the OGRE testing chamber and the equipment used to attain the desired operating conditions are shown. Two different variations of the setup are discussed, the iron-55 arrangement and the strontium-90 arrangement. Due to the dangers of using strontium-90 in the lab an alternative system was needed to decrease the hazards associated with its use.

Chapter 7 shows the results of the characterisation tests on the CCD207-10 and how these compare to the mission requirements. The observations of X-ray events are shown and key factors in the operation of the EM-CCD, such as gain and its variation with operating temperature, are shown. The nature of sounding rocket missions and observation times also highlights key areas and restrictions in the ideal operation of the camera system with limitations and factors discussed. Alternative operating methods are shown with advantages and drawbacks of each mentioned. The device is shown to be suitable in terms of operations and the gain that can eb achieved to amplify low level signals.

Chapter 8 shows the event processing algorithm and its principles as well as the effects of observing X-rays from the two different sources and how these detected events compare. An alternative operating method for the camera is discussed as well as the counting of X-rays with varying gain. The transferral of the event detections finding and how this can be condensed into a form ready for telemetry back to the ground using the available equipment is also shown to demonstrate how the data can be evaluated on-board the rocket and checked by the team on the ground, enabling possible changes of the operation of the whole OGRE system during the flight to compensate for any potential issues that could occur. A method of further distinguishing events of interest by comparing ratios of the charge distribution is observed with useful information observed on-board the rocket capable of being extracted and telemetered to the ground via the available system.

Chapter 9 brings together each chapter's finding and concludes the results of each research goal as well as discussing potential avenues of future work in this area and possible benefits for X-ray astronomy.

1.4 Publications

- Matthew R. F. Lewis, Matthew R Soman, Andrew D. Holland, Neil J. Murray, David Hall, Daniel P. Weatherill, James H. Tutt, Randall L. McEntaffer, Casey T. DeRoo, Ted B. Schultz, and Karen Holland "Development of the x-ray camera for the OGRE sub-orbital rocket", Proc. SPIE 9915, High Energy, Optical, and Infrared Detectors for Astronomy VII, 991506 (5 August 2016); https://doi.org/10.1117/12.2232812
- Lewis, M., Soman, M., Holland, A., Lumb, D., Tutt, J. H., McEntaffer, R. L., Schultz, T., Holland, K. (2017). "The simulated spectrum of the OGRE X-ray EM-CCD camera system", Journal of Instrumentation, 12(12), [C12020]. https://doi.org/10.1088/1748-0221/12/12/C12020
- James H. Tutt, Randall L. McEntaffer, Benjamin Donovan, Ted B. Schultz, Michael P. Biskach, Kai-Wing Chan, John D. Kearney, James R. Mazzarella, Ryan S. McClelland, Raul E. Riveros, Timo T. Saha, Michal Hlinka, William W. Zhang, Matthew R. Soman, Andrew D. Holland, Matthew R. F. Lewis, Karen Holland, and Neil J. Murray "The Off-plane Grating Rocket Experiment (OGRE) system overview", Proc. SPIE 10699, Space Telescopes and Instrumentation 2018: Ultraviolet to Gamma Ray, 106996H (6 July 2018); https://doi.org/10.1117/12.2311813
- Benjamin D. Donovan, Randall L. McEntaffer, James H. Tutt, Ted B. Schultz, Michael P. Biskach, Kai-Wing Chan, Michal Hlinka, John D. Kearney, James R. Mazzarella, Ryan S. McClelland, Raul E. Riveros, Timo T. Saha, William W. Zhang, Andrew D. Holland, Matthew R. Lewis, Matthew R. Soman, Karen Holland, and Neil J. Murray "Optical design of the Off-plane Grating Rocket Experiment", Proc. SPIE 10699,

Space Telescopes and Instrumentation 2018: Ultraviolet to Gamma Ray, 106993U (6 July 2018); https://doi.org/10.1117/12.2312219

- Benjamin D. Donovan, Randall L. McEntaffer, James H. Tutt, Bridget C. O'Meara, Fabien Grisé, Kim A. Allgood, Michael P. Biskach, Kai-Wing Chan, Michal Hlinka, John D. Kearney, James R. Mazzarella, Ryan S. McClelland, Ai Numata, Raul E. Riveros, Timo T. Saha, Peter M. Solly, William W. Zhang, Andrew D. Holland, Matthew R. Lewis, Matthew R. Soman, and Karen Holland "An updated optical design of the off-plane grating rocket experiment", Proc. SPIE 11119, Optics for EUV, X-Ray, and Gamma-Ray Astronomy IX, 1111911 (9 September 2019); https://doi.org/10.1117/12.2528858

2 X-ray spectroscopy missions

To better identify how the OGRE project is going to embrace new technologies to advance the field of X-ray astronomy it is important to look back at the history of X-ray spectroscopy and the missions that have advanced observations in this area.

2.1 Spectrometry

The study of different photon energies by dispersing light has been carried out for hundreds of years. The most basic form of this that many physicists would describe is light passing through a prism and creating a rainbow on the other side. Newton's experiments with a series of prisms showed the colours were already a part of the light by passing one part of the rainbow, i.e. the red light, through another prism and observing only one colour out of the second prism (Newton 1704). Thomas Young combined these findings with Huygens wave theory to show that the colours observed were due to the wavelength of the light (Barry 2008).

Quantum mechanics dictates that the energy levels within an atom's electron shells are restricted to certain values, i.e. quantised. The conservation of energy therefore means that if an atom absorbs or emits energy it must be moving from one energy level to another within the atom's electron shell. This difference in energy is known as the Bohr frequency condition (Bohr 1913). With the energy change for an atom changing from energy level E1 to energy level E2, v being the frequency of the radiation and h being Planck's constant (6.626×10^{-34} J s^{-1}):

$$\Delta E = E_2 - E_1 = hv \qquad 2\text{-}1$$

When it comes to electromagnetic radiation each wave has three properties which determine its' behaviour: wavelength, frequency, and amplitude. Focussing on a single

photon within this wave, therefore removing amplitude, and considering that the speed of light in a vacuum (c) is a constant gives:

$$c = \lambda v \qquad 2\text{-}2$$

Combining this with the Bohr frequency condition therefore gives

$$E = hv = \frac{hc}{\lambda} \qquad 2\text{-}3$$

This shows that light is quantised with only the frequency or wavelength being needed to determine the photon energy. Thus, by observing one of these properties in a photon from a source it is possible to know the energy change that occurred within the source.

This energy change can be brought about by either emission or absorption. When an orbiting electron absorbs a photon, it will shift to a higher energy level, however the atom wants to be at its ground level, i.e. the least energy possible, and so it can emit this energy if the excitation source is not maintained. This drop in energy causes the emission of a photon with energy equal to that of the transition. Observing this photon and determining its energy allows the atom the photon came from to be identified. The measuring of specific photon energies due to absorption or emission is known as spectrometry with the instrument used to make such measurements being known as a spectrometer.

The electromagnetic spectrum defines X-rays to be photons with a wavelength ranging from 0.01 nm to 10 nm and therefore possess energies from 100 eV to 100 keV. Photon sources can of course emit at other wavelengths and the study of different parts of the Universe at different photon energies gives a broader idea of the physics at work.

2.2 Cosmological photon sources

There are many different cosmological wonders in the Universe behaving in drastically different manners. Many of these are so far away, or appear so small, that even with the best telescopes they appear only as a single pixel in an output image, whilst other objects appear significantly larger to the point where a single detector may not be enough to fully observe it. These are known as point sources and extended sources respectively and the science behind these objects and how to observe them varies significantly.

The extent to whether a photon source is classified as a point source or extended source is dependent on the method of observation. A good example are planets; they appear as a single bright point to the naked eye however to a telescope the planet could be observed in detail. The rest of this chapter will generalise sources as being outside of the solar system and therefore at a great distance from Earth.

2.2.1 Extended Sources

When it comes to imaging in astronomy, many of the pictures seen will focus on one object. Object here is defined loosely as some larger bodies are comprised of many smaller bodies. Galaxies can house few hundred million to hundred trillion stars all orbiting a central point which could contain an active black hole. The main object of the observation is an extended source however and thus covers a large portion of the image.

Another extended source an astronomer may want to observe is a nebula. These large interstellar clouds are comprised of dust and gas in large structures which can stretch to be hundreds of light years across. Some are diffuse with no obvious boundaries, whilst others are formed from the remnants of a supernova. Nebulae are usually highly star forming as dust and gas particles start to clump together and thus create a greater gravitational potential causing more material to accrete towards the forming star or planet.

Whilst the stellar evolution of a galaxy cluster can be inferred the smaller bodies it comprises of are lost as their light is combined with other surrounding photon emitters. Some regions may be blocked out entirely if imaging at certain energies (Figure 2-1).

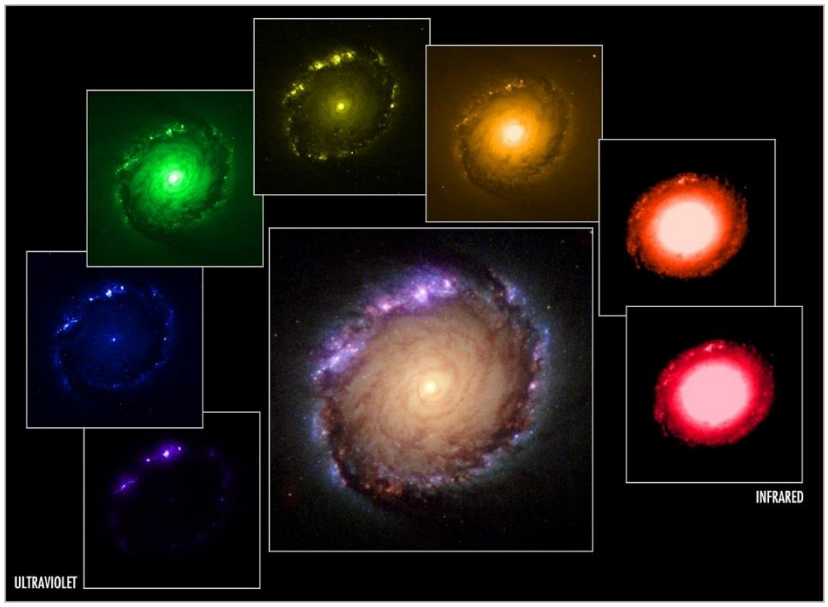

Figure 2-1: Panels of broad waveband observations of the galaxy NGC 1512 with Hubble over different sections of the EM spectrum highlighting the variations in observations depending on the desired energy range, colour mapped to allow for a composite image covering a greater region of the EM spectrum. (Image credit: NASA, ESA, Dan Maoz (Tel-Aviv University, Israel, and Columbia University, USA))

If astronomers would like a better idea of how some of the smaller scale things within the Universe formed or behave it is therefore better to observe point sources that are not part of these extended sources.

2.2.2 Point sources

As alluded to in the previous sections, some point sources can be observed within extended sources however their 'neighbourhood' can affect what is observed. Luckily, there are many point sources that can be observed within our own galaxy of which local interference is low. With the naked eye every star in the night sky is within our galaxy. Light from stars in other galaxies is reaching us but after travelling such a large distance it has spread out so much that the amount of incoming light per unit of time, or flux of the light,

is negligible. By observing local stars, i.e. stars in our galaxy a large range of astronomy becomes accessible.

2.2.3 X-ray sources

X-rays in astronomy originate from incredibly hot sources. The surface of the sun, which is 5,778 K, peaks in the visible region of the EM spectrum and so is incredibly bright and apparent to us, however the stellar corona is several million Kelvin and emits strongly in the X-ray waveband. Other sources of X-rays include pulsars, supernovae remnants and black hole accretion disks, all regions of high energy activity and therefore of significant astronomical interest.

2.3 Spectrometer designs

A collimator is a device that narrows a beam of particles or waves. To narrow can mean either to cause the directions of motion to become more aligned in a specific direction (i.e., make collimated light or parallel rays), or to cause the spatial cross section of the beam to become smaller (beam limiting device). This collimated light can then be passed to a diffraction grating, dispersing the collimated light by varying amounts depending on the photon energy. This can then be focussed towards a detector.

This general design can be used to separate photon energies with ease, however, with X-rays being known for passing through objects, X-ray spectrometers needed to be designed differently to focus the X-rays through multiple instruments towards a detection mechanism and ensure the number of X-rays passing through the individual components are minimised. There are a variety of potential layouts for a system capable of this, many of which have already been tested in space-based telescopes.

2.4 Notable missions

The lifetime of a space mission begins a long time before the instrument is on the launch pad. This section therefore looks at a variety of projects, some of which are well-known and currently operating, others which are on their way to the launch pad to demonstrate the currently used means of observing X-rays using space-based equipment.

2.4.1 Chandra

Launching on 23rd July 1999, Chandra has been NASA's main X-ray Observatory and is one of the most important telescopes in current astronomy. To detect X-ray emissions from very hot regions of the Universe such as exploded stars, clusters of galaxies, and matter around black holes a satellite telescope was needed due to X-rays being heavily absorbed by the Oxygen and Nitrogen in the Earth's atmosphere. Chandra has an elliptical orbit around the Earth with its furthest distance being 139,000 km. Chandra is controlled by and telemeters data to the Smithsonian's Astrophysical Observatory in Massachusetts, USA.

The mirror section of Chandra's X-ray telescope is known as the High-Resolution Mirror Assembly, or HRMA. This is a Wolter Type-1 style mirror arrangement comprising of a parabolic mirror reflecting at a shallow angle into an accompanying hyperbolic mirror. The HRMA consists of four 'nested' mirrors, i.e. the mirrors sit inside each other (Figure 2-2). These mirrors have diameters of 0.65 m, 0.87 m, 0.99 m, and 1.23 m (Gaetz and Jerius 2005) with each mirror fabricated from Zerodur glass, a low expansion, high-precision glass, and coated with iridium (Weisskopf, et al. 2000) to improve X-ray reflectivity.

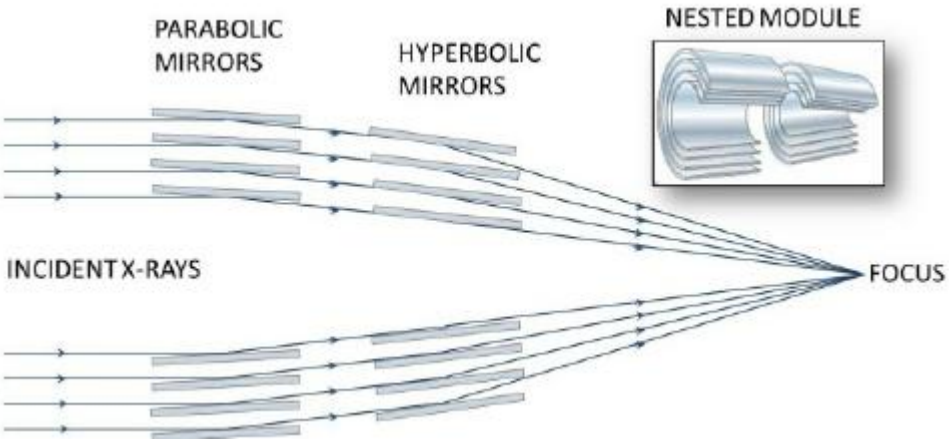

Figure 2-2: Wolter-1 optics system showing the parabolic/ hyperbolic mirror pair, the direction of incoming X-rays to a focus point and the nature of the nested optics. Image credit (Gaskin, et al. 2015)

Depending on the observation desired Chandra can move several different tools in place for the light to interact with after passing through the HRMA. Two different transmission gratings, a high energy and low energy grating, can be moved depending on the energy observation desired. The low energy grating is used for observing photons at energies between 0.07 keV and 0.2 keV whilst the high energy transmission grating can observe between 0.4 keV and 10 keV. These interferometers can also be left out of the light path if standard imaging is desired.

The photons then travel 10 m to the focal point where one of two instruments are used, the High-Resolution Camera (HRC) or the Advanced CCD Imaging Spectrometer (ACIS). The HRC features two detectors, HRC-I for imaging and HRC-S for spectroscopy whilst ACIS features 10 CCDs each consisting of 1024 x 1024 pixels. The arrangement of these 10 devices allows for imaging as well as spectrometer readings.

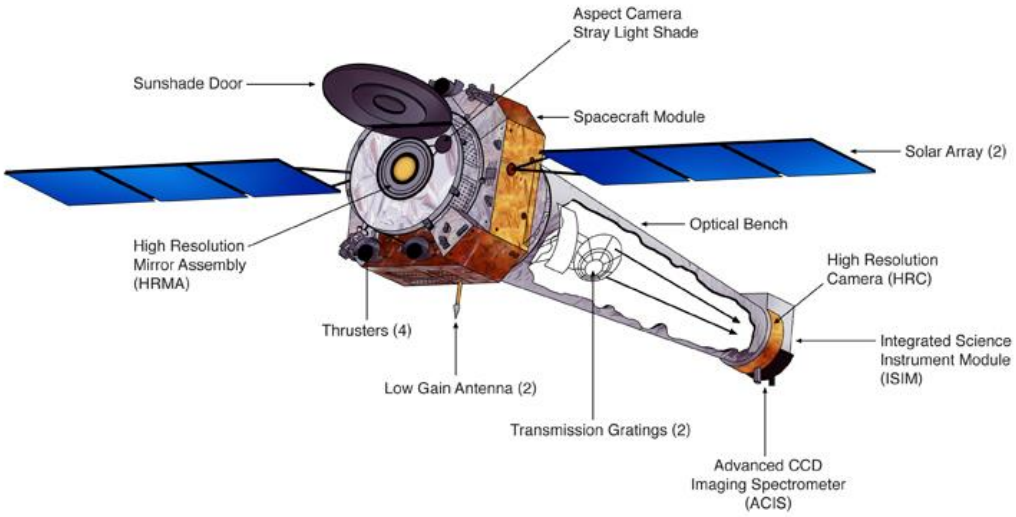

Figure 2-3: The Chandra space telescope labelled to show the main mechanisms allowing it to operate as an X-ray telescope. (Image credit: NGST & NASA/CXC)

2.4.2 XMM-Newton

XMM-Newton is an X-ray space observatory launched by the European Space Agency in December 1999, the same year as Chandra. XMM-Newton's main task was to investigate interstellar X-ray sources, perform narrow and broad-range spectroscopy of X-ray sources, and to capture images of objects in both X-ray and optical (visible and ultraviolet) wavelengths simultaneously.

XMM-Newton features 3 co-aligned telescopes, each featuring a Wolter-1 mirror assembly. The biggest difference between this optic system compared to Chandra is the XMM-Newton's three optical assemblies each feature 58 thin mirrors separated by only 25 microns. The radii of each of these mirrors is considerably smaller than Chandra with the inner diameter being 0.306 m and the outer radius 0.7 m. Each mirror is made of nickel with a thin gold coating (F. Jansen 2001).

Two different instruments are present within the observatory, the European Photon Imaging Camera (EPIC) and the Reflection Grating Spectrometer (RGS). EPIC allows for

sensitive imaging over a 0.15 keV to 15 keV energy range and features two Metal-Oxide Semiconductor (or MOS) cameras, each made up of 7 MOS-CCDs which are specially formatted for the detection of low-energy X-rays. The third EPIC instrument is a pn-CCD camera used for detecting high energy X-rays.

The RGS instrument is present on two of the three telescope systems and feature a set of on-plane gratings with varying line densities. There are 9 CCDs in each RGS positioned to detect the dispersed light.

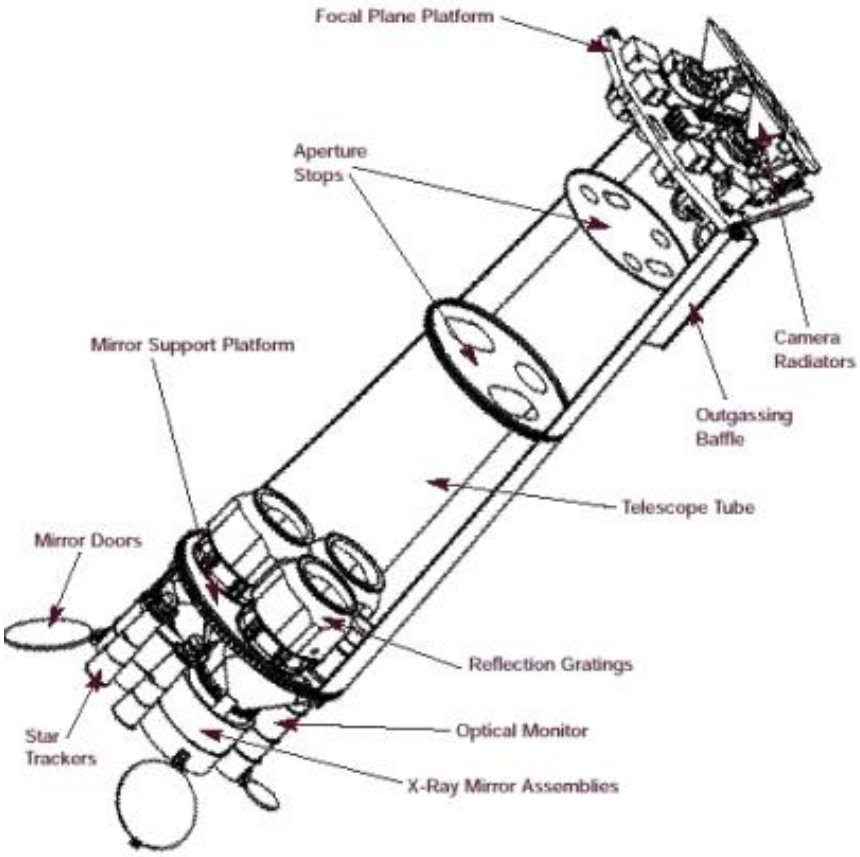

Figure 2-4: The design of the XMM-Newton telescope with labels showing the main components of the system. (Image credit: cosmos.esa.int)

Originally scheduled for a two-year mission, the spacecraft remains in good health and has received mission extensions through 2016. ESA plans to succeed XMM-Newton with the

Advanced Telescope for High Energy Astrophysics (ATHENA), the second large mission in the Cosmic Vision 2015-25 plan, to be launched in 2028.

2.4.3 Hitomi

Developed by the Japan Aerospace Exploration Agency, Hitomi (also known as ASTRO-H) featured a suite of instruments to image both soft and hard (>10 keV) X-rays. The intended observation targets of Hitomi were galaxy clusters where it was hoped that observations could allow for a better idea on the evolution of the Universe, as well as supernovae. The instruments on board allowed for imaging and spectroscopic measurements in a manner of different methods. Two soft X-ray telescopes allowed for soft X-rays (in this case approximately 0.4-12 keV) to be detected with one giving an image output and the other providing high resolution (energy resolution requirement of 7 eV and a goal of 4 eV) spectroscopy.

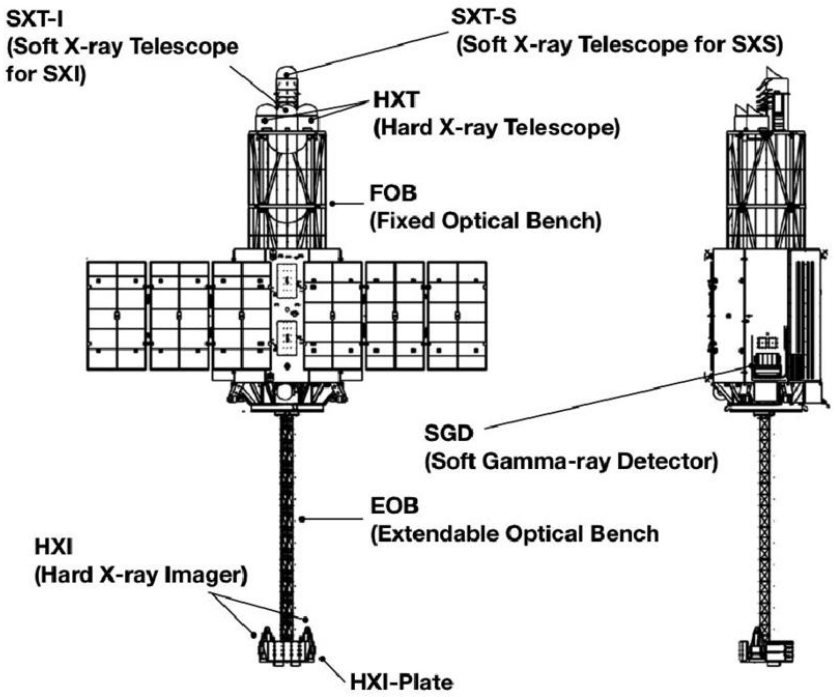

Figure 2-5: Schematic of the Hitomi space telescope with the extendable optical bench deployed and other key ares of the X-ray imaging system labelled (Takahashi, et al. 2016)

2.4.4 IXPE

The Imaging X-ray Polarimetry Explorer will be launched on or after November 20, 2020 from Kwajalein Atoll into a 540-km circular orbit at 0° inclination. During IXPE's two-year mission, targets such as active galactic nuclei (AGN), micro quasars, pulsars, and pulsar wind nebulae, magnetars, accreting X-ray binaries, supernova remnants, and the Galactic centre will be studied.

The cost of IXPE will be $188 million, which includes the cost of the launch vehicle and operations and data analysis after launch. The Principal Investigator is Dr. Martin Weisskopf of NASA and Marshall Space Flight Center (MSFC) is providing the spacecraft and the services of mission integration. The X-ray polarization detectors will be provided by the Italian Space Agency, Agenzia Spaziale Italiana (ASI). Dr. Brian Ramsey is leading the effort to produce the grazing-incidence X-ray mirrors at NASA/MSFC.

IXPE's payload is a set of three identical imaging X-ray polarimetry systems mounted on a common optical bench and co-aligned with the pointing axis of the spacecraft. Each system operates independently for redundancy and comprises a 4-meter focal length mirror module assembly that focuses X-rays onto a polarization-sensitive imaging detector developed in Italy. The focal length is achieved using a deployable boom.

The Gas Pixel Detectors (GPD) utilise the anisotropy of the emission direction of photoelectrons produced by polarized photons to gauge with high sensitivity the polarization state of X-rays interacting in a gaseous medium. Position- and energy-dependent polarization maps of such synchrotron-emitting sources will elucidate the magnetic field structure of the X-ray emitting regions. X-ray polarimetric imaging better indicates the magnetic structure in regions of strong electron acceleration. The system is capable to resolve point sources from surrounding nebular emission or from adjacent point sources.

2.5 Sounding Rockets

The previously described missions have all involved expensive satellites which require a long build time and result in a telescope which will operate over several years in space. The technology used must be tested in some way before being used in such a large-scale mission and whilst lab testing is enough for general ideas on the performance of the technology, other factors can come into play when it is put into space. Rather than gamble on the performance of an instrument in the lab being as effective elsewhere, it is better to test it on a small scale, space-based mission. This is where sounding rockets can be used. Named after the nautical term for taking measurements, ‘to sound’, these rockets allow for short flight times to demonstrate instrumental concepts on a reusable vessel.

Sounding rockets have been used to test X-ray instruments for over 40 years (Agrawal, et al. 1976) and have helped influence the designs of other projects by demonstrating effective technologies. The X-ray telescope discussed by Agrawal features a Wolter-1 optic comprising of two nested mirrors, a steppingstone on the way to the systems seen in some of the previously discussed satellite observatories. Whilst OGRE will be aiming to capture an accurate spectrum and thus promote the use of some of its key components in future missions, other recent sounding rocket experiments have helped advance X-ray astronomy in their own way.

2.5.1 OGRESS

The Off-plane Grating Rocket for Extended Source Spectroscopy, or OGRESS, was a collaborative project with input from the same team currently based at Penn State University (located at the University of Iowa at the time of launch), the University of Colorado, and NASA's Goddard Space Flight Center (Rogers, McEntaffer, et al. 2013). The observing target was the Cygnus Loop supernova remnant in the soft X-ray waveband (0.3 - 1.2 keV) and OGRESS aimed to perform moderate spectral resolution spectroscopy of this large diffuse source. It had been noted that previous missions designed for observing point sources with a high resolution (Chandra and XMM-Newton being named in some publications) could not obtain high resolution spectra of diffuse sources due to their wide line spread functions. The design of the OGRESS payload was meant to keep costs down to a low budget whilst meeting their scientific goal of determining the dominant emission mechanism and the equilibrium state and elemental abundances of the plasma within the Cygnus Loop.

The OGRESS design consists of two identical modules each consisting of three main components, some of which had been flown on previous sounding rockets. The first, the focusers, were a series of wire-grid nickel plates which were stacked in sequence and

arranged so that the light which passes through would all go to the same focus. This is achieved by having the plates converge over their 0.9 m length. Whilst the opening of the grid covered a 165 mm x 165mm area and featured wires that were 165 µm wide and spaced 889 µm, the end the light left at covered a 100 mm x 100 mm area and featured wires that were 145 µm wide and 500 µm apart. This system did not actively focus the light but instead destroyed light that was travelling in unwanted directions. The effectiveness of the system meant that for a point source, only one of the gaps would be illuminated but for extended sources all light that would go to the focus is able to cover a larger area. This was seen to be effective on the CODEX sounding rocket project (Zeiger, et al. 2011).

The light which passed through the focusers was then incident on an off-plane grating array, which diffracts the light into an arc. The gratings needed to fill the area of the focuser and were mounted at an angle of 4.4° to the light path allowing for efficient reflections at the X-ray energies. A total of 67 gratings were used in each module, each grating featuring 5670 grooves/mm and giving a cross-section to the light covering 104 mm by 1.53 mm.

The diffracted light travelled approximately 2 m before being incident upon a Gaseous Electron Multiplier (GEM) detector. These devices utilise a gas within the detector, which is ionised by incoming photons, thus liberating electrons. A series of plates held at sequentially lower negative voltages can then accelerate the resultant electrons towards an anode creating a cascade effect which multiplies the signal (Figure 2-6). An advantage of GEM detectors is that they have a high quantum efficiency meaning many of the incident photons are successfully observed. They are also quite large meaning a single device can cover a larger area than many other detectors. The GEM detectors used on OGRESS were 100 mm by 100 mm. The biggest disadvantage of using a GEM detector comes from the gas which needs to be ionised to work. This must be held at a constant pressure and so a gas

supply must be used alongside the detector so that after ionization occurs the supply is replenished.

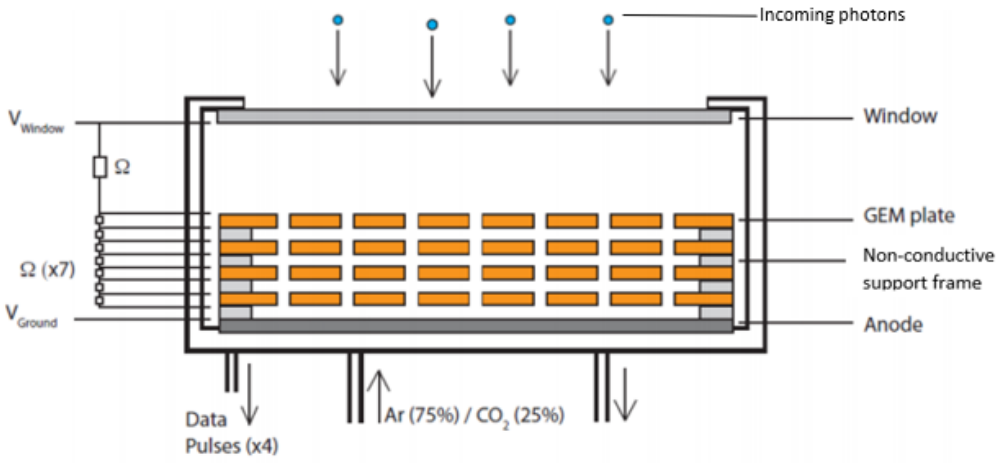

Figure 2-6: The schematic of a GEM detector. Adapted from (Rogers, McEntaffer, et al. 2013).

As OGRESS followed on from previous sounding rocket missions a series of factors had been considered to try and ensure a successful mission. Prior missions had combined the data from multiple sources into a single stream before digitisation whereas OGRESS parallelised and combined the data after digitisation (McCoy, Schultz, et al. 2015). This allowed for clarity on which of the two modules the data was from as well as the transmission of other diagnostic information, e.g. pressure of the GEM gas.

Whilst tested and calibrated on the ground the team felt it best to perform in-flight calibrations too as prior experience had shown the performance of scientific payloads on board sounding rockets had varied drastically from the performance observed in the lab. During the flight, the rocket was skewed to observe a ‘dark patch’ of the sky, then the Cygnus loop. The detectors were also kept on at the end of the observing period and after the shutter door on the craft closed to obtain a dark calibration of the noise from the rocket itself.

The Cygnus loop was observed for approximately 200 s with the raw data not showing any obvious sign of a spectrum being captured. It was evident that an unanticipated source of noise that exceeded the Cygnus signal was present. The favoured explanation was that X-rays were being generated within the interior of the telescope and were being detected in the expected manner resulting in the uniform signal they observed (Rogers, Schultz, et al. 2015). As the detectors were left on after the shutter doors closed, i.e. when Cygnus was no longer being observed, a decrease in the observed signal was observed suggesting light from the desired source was present in the data. Due to the noise present in the findings nothing conclusive could be drawn from the observation.

2.5.2 WRXR

The Water Recovery X-ray Rocket, or WRXR, is another previous sounding rocket mission developed by the Penn State University team. Like OGRESS, WRXR intended to observe an extended source, the Vela supernova remnant, in the soft X-ray bandpass (0.25 keV – 0.8 keV). The region of this large supernova remnant (located ~250 pc away yet covering an angle of around 8°) to be observed had been largely unexplored, providing new data for astronomers to use. The Vela remnant hosts a bright pulsar which would interfere greatly with X-ray observations and so the observing region was located far enough away for it not to be a factor. As suggested by the name, this was also to be the first NASA astrophysics sounding rocket to have a splash landing and be recovered from the sea.

The WRXR payload design follows a similar design as that of OGRESS. A slight variant on the focuser, now referred to as a collimator, is used to ensure only light travelling in a certain direction can pass through the telescope towards a certain focal point. This design again narrows down from 0.724 mm slit widths to 0.5 mm over a travel distance of 0.9 m. The overall field of view for the collimator is 3.25° however the design allows for each different element of the observable source to be sampled ~4.4 times (Miles, et al. 2017).

The light is then incident on the X-ray reflection gratings which disperse the photons varying amounts dependant on their energy. These gratings featured 5750 grooves/mm and a graze angle of 2.2° was used, a value decided upon to maximise the diffraction and geometric efficiencies of the telescope. Each of the 26 gratings used were coated in nickel which has a high reflectivity for soft X-rays.

After travelling around 2 m the light is incident upon the X-ray hybrid CMOS (Complementary Metal Oxide Semiconductor) Detectors (HCD). To improve the performance of the detectors an aluminium filter is used over the surface to prevent the detection of optical light whilst allowing X-rays to pass through largely unhindered (Figure 2-7). The X-rays are absorbed into a silicon substrate producing an electron charge via the photoelectric effect. Each 36 μm pixel in the detector has its own readout circuitry. The hybrid definition comes from the separation of the circuitry and sensor layers. Monolithic CMOS sensors feature the readout circuitry and photosensitive pixel elements manufactured within the same silicon wafer. The HCD features a separate substrate and circuit readout. The two are 'bump bonded' using indium allowing the charge to transfer from the silicon to the readout optics.

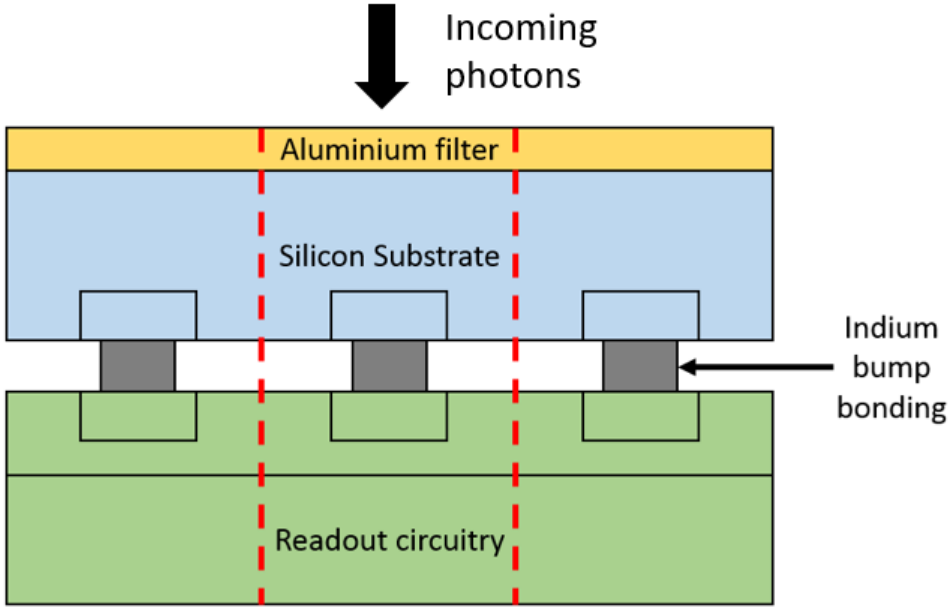

Figure 2-7: Hybrid CMOS Detector schematic

Occasionally a sounding rocket payload will allow for multiple experiments to be launched. This was the case for WRXR. The single collimator meant that an additional light-dependant experiment could be flown alongside the main payload experiment. An X-ray lobster eye telescope was designed and built to observe the same region of the Vela remnant but with a 1.5° by 1.5° field of view and imaging in the hard X-ray bandpass (3 keV to 60 keV).

A smaller 3D camera system was also flown on WRXR called SµGRE-1, or the Schools micro-Gravity Rocket Experiment. This aimed to observe interactions in micro-gravity between small, sugar-cube sized objects created by schools. These objects were kept behind a shutter which opened once the rocket reached a suitable altitude for micro-gravity observations.

Unfortunately, during the launch of the WRXR missions there was a large breach in the rocket payload due to a collision with some space debris. Some useful data was extracted from the mission, but this incident highlighted the difficulties with observing in space and testing technologies in this manner. The SµGRE camera operated throughout the flight and

despite being held in a fixed location and avoiding damage, captured the moment of decompression during the flight alongside some micro-gravity observations. The rocket was successfully recovered at sea after the flight. The construction of the WRXR payload, methods of grating module fabrication and the overall project process will aid in the running of the OGRE project.

2.6 Summary

X-ray astronomy can open many research areas for astronomers with many findings of significant interest currently hidden within this section of the electromagnetic spectrum. Imaging in the X-ray to a good deal of accuracy is a relatively new concept with many of the previous missions allowing glimpses and ideas of what more complex systems could be capable of seeing.

The previous systems employed have been able to detect X-rays and do some separation within the spectral resolution of the photon's source. Further improving this resolution will benefit researchers more allowing for more conclusive ideas of the complex mechanisms elsewhere in the Universe.

The systems used to obtain the data have a good amount of variation with the detectors used heavily influencing the capabilities of the entire system. Missions such as WRXR and OGRESS are therefore key to testing some of these systems before a high-profile project dedicated to these methods is committed to. These tests allow for better systems to be suggested and tested to determine suitability in future projects. Just as OGRESS and WRXR expanded on previous projects to see how best to further the field, OGRE aims to take these learning and implement a new system which could be of great benefit in a later large-scale mission.

3 The OGRE mission

The Off-plane Grating Rocket Experiment, or OGRE, is a joint project between three teams based at Penn State University (work on OGRE originally started whilst they were based at the University of Iowa), NASA's Goddard Space Flight Centre (GSFC), and a joint UK team of the Open University and XCAM Ltd. The key three technological components of the instrument are the silicon mirror optics system, the off-plane diffraction gratings, and an EM-CCD camera. The instrument design and arrangements described in this chapter are the initial designs and will be referred to as the 'first revision' throughout the rest of this chapter.

3.1 OGRE's key aims

OGRE was designed to demonstrate the performance of key technological components of a soft X-ray spectroscopy instrument suitable for the next generation of X-ray observatories. This will be achieved by collecting the highest resolution soft X-ray spectrum of Capella observed to date.

3.1.1 Technology Readiness Levels (TRLs)

OGRE will test three relatively new pieces of technology with the hopes of increasing their Technology Readiness Level (TRL, Table 3-1) upon the successful acquisition of an accurate high-resolution spectrum of Capella. The TRL of a technology is a helpful value that allows an at a glance idea of its maturity based on its previous use.

Table 3-1: The NASA Technology Readiness Levels. Credit to (Mankins 1995)

TRL value	**Level is successfully acquired when…**
1	Basic Principles have been observed and reported
2	Technology concept and/or application formulated
3	Analytical and experimental critical function and/or characteristic proof of concept
4	Component and/or breadboard validation in laboratory environment
5	Component and/or breadboard validation in relevant environment
6	System/ subsystem model or prototype demonstration in a relevant environment (ground or space)
7	System prototype demonstration in a space environment
8	Actual system completed and "flight qualified through tests and demonstrations (ground or space)
9	Actual system "flight proven" through successful mission operations

The TRL is based on the project type and environment, for example a new type of detector may have been used on a successful sounding rocket experiment and given good results but has only undergone laboratory test for use in a satellite observatory. The TRL for sounding rocket use would therefore be TRL 9 whilst its satellite use would be a TRL 4. The designer of a new satellite may consider this detector for use and can quickly see that some science that may be relevant has been successfully carried out (hence the TRL 9) but not have been fully optimised for a grander use (due to the TRL 4). Thus, the new satellite could implement a tested technology in a new way leading to new science.

The current TRL values of the OGRE technologies are around TRL 4-6 however a successful mission will see the TRL of each proceed to TRL 8-9 for sounding rocket use.

3.1.2 Minimum and comprehensive success criteria

To be classified as a minimum success, OGRE must achieve the following:

MS1) Proper functioning of the telemetry system and good digital data recording of the data produced.

MS2) Recovery of the payload with no water inside hermetically sealed on board storage computer/ electronic section.

MS3) At least 180 seconds of science target observation above 150 km.

MS4) Pointing accuracy of < 5 arcminutes (absolute) and knowledge of < 1 arcsecond per second (3- sigma, minimum 10 Hz) for the science target.

MS5) Temperature of the optics controlled to ± 1°C.

MS6) Temperature of the CCD maintained below -50°C during science and calibration target observation.

MS7) Minimum of one resolvable spectral line with 25 photons in the line.

To be classified as a comprehensive success, OGRE must achieve the following:

CS1) Proper functioning of the telemetry system and good digital data recording of the data produced. (MS1 & CS1 are identical)

CS2) Successful recovery of the payload with no water inside the telescope sections/ electronics module and all hermetic seals intact and functional.

CS3) Greater than 280 seconds with the shutter door open. These 280 seconds includes at least 240 seconds above 150 km, on the science target, and nominal slew/ settle times for the Attitude Control System.

CS4) Pointing accuracy of <2 arcminutes (absolute) and knowledge of < 1 arcsecond per second (3-sigma, minimum 10 Hz) for the science target.

CS5) Temperature of the optics controlled to ± 0.13°C.

CS6) Temperature of the CCD maintained below -80°C ± 1°C during science and calibration target observation.

CS7) Greater than one resolvable spectral line with 25 photons in the line.

Many of these conditions are being primarily worked on by the Penn State team (MS2, CS2, MS4, CS4) with a great deal of input on many of the other conditions coming from the OU/XCAM team who are responsible for the data collection and handling. Throughout this thesis these conditions will be referred to when relevant.

3.2 Capella

To the naked eye Capella appears to be a point source, i.e. it appears to be a single star, and is the sixth brightest star in the night sky, however, Capella is a small system comprising of four stars. The system, located 42.9 light years away, is best described as two binary star systems as each binary host similar type stars. The first binary system, and that which is generally referred to as Capella A, is comprised of two yellow giants (Capella Aa and Capella Ab). It is theorised that the corona of these two stars generate most of the X-rays observed (Mewe 1982). These stars are highly active with the most active star, Capella Aa having a luminosity roughly 80 times that of the Sun. Capella Aa and Capella Ab orbit each other at a distance of 0.74 au (1 au being the average distance from the Sun to the Earth) with one full rotation every 104 days. This orbit is non-eclipsing meaning both stars can be wholly observed from our observation point.

The second binary system in Capella are two red dwarf stars (Capella H and Capella L) which are fainter in the X-ray region but emit in the infrared. A separation of 10,000 au between the two binary systems has been observed. The luminosity of this second system is sufficiently lower than that of Capella Aa and Capella Ab so should not have any impact on the observed results.

Capella has been observed by several X-ray missions previously. Its high luminosity and non-eclipsing arrangement make it an ideal target for observations due to the large photon flux and low variation (due to all sources being unobstructed) and has been used previously as a calibration source for X-ray instruments. Due to the sounding rocket approach of the OGRE mission, Capella is the only observation target to be sued. A recent X-ray spectrum was captured by Chandra (Figure 3-1). The observation was carried out with an effective area of 0.04 m^2 and required 84597 s to capture.

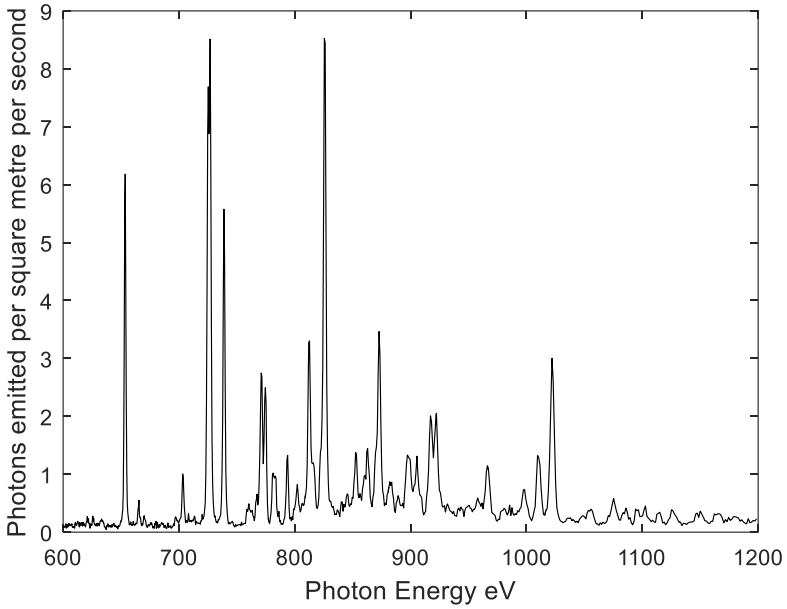

Figure 3-1: Capella spectrum constructed from the Chandra data set over the OGRE X-ray energy range and presented in terms of the photons emitted per second per metre of observation area for each distinct energy bin in the Chandra instrumentation. Data provided by (Lumb 2017).

3.3 Mission Operations

The actual operation of OGRE will be determined by several factors surrounding its launch. Capella is located at a declination of +45° 59’ 53’’ which restricts the launch sites and times available for use.

3.3.1 Launch date and site

The original launch location of the OGRE rocket was the Poker Flats launch site in Alaska, USA. This location restricted the launch date to the winter months of the year due to the need to point the rocket towards Capella after launch and the launch location meaning the Earth would be an obstruction. The rocket originally scheduled for launch in February 2018.

Changes in the OGRE design meant the launch date slipped. It was therefore decided that an alternative launch site should be used if possible, to allow for a scheduled launch throughout the year due to a better alignment with the Capella pointing that would be required. The launch location was therefore switched to Wallops Flight Facility located in Virginia, with a launch date scheduled for Q2 of 2020. At the time of writing, this launch date will slip further, and the launch location is likely to be reviewed again.

3.3.2 Launch vehicle: The Black Brant IX

The sounding rocket used by NASA for OGRE will be the Black Brant IX. This two-stage rocket is comprised of an adapted military surplus booster and a specially designed Black Brant motor. This is a relatively lightweight payload weighing 1333.6 kg of which 1014.7 is the fuel.

The maximum altitude the rocket will reach is dependant of the mass of the payload and angle of launch. To ensure the observation time conditions are met (MS3 and CS3) it is therefore important to ensure the mass of the OGRE payload is kept below certain masses depending on the launch configuration (Figure 3-2). To ensure the desired observation window is achieved alongside the time required to point the rocket towards Capella, the mass of the payload must be considered greatly, whilst also ensuring the equipment is rigid and capable of maintaining high accuracy observations after undergoing the large forces of

a rocket launch. This trade-off needs to be monitored to ensure the mission is not compromised in any regard.

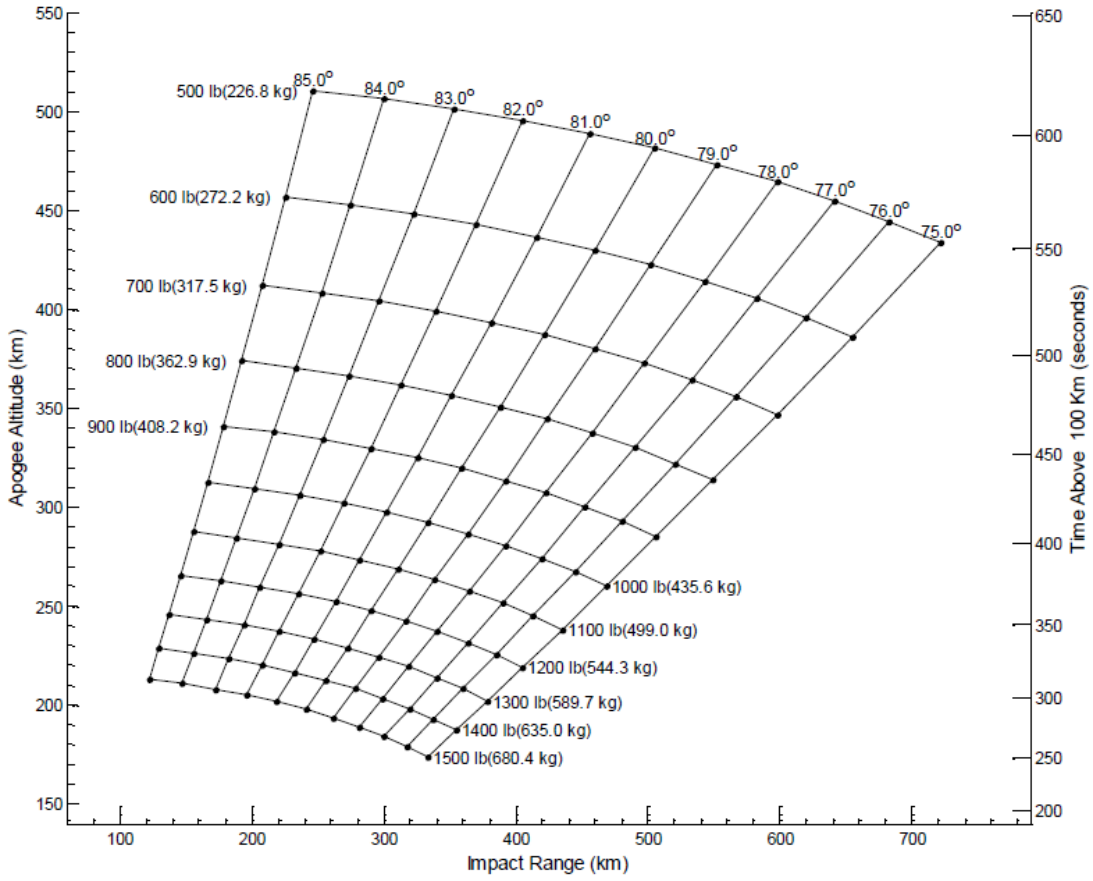

Figure 3-2: The Black Brant IX Launch vehicle performance when launched at sea level for varying payload masses when launched at different angles. Figure from (NASA Goddard Space Flight Center 2015)

3.3.3 The launch day procedure

On the launch day it is vital to check the operations of the payload before launch to ensure there is a good chance of a successful mission. Due to the nature of this experimental payload, time will be needed to set up the system before launch. Figure 3-3 shows a rough time plan of the launch day procedure, with indicative lines showing the temperature of the focal plane in the camera and vacuum pressure within the camera head unit. The critical pressure is the saturation vapour pressure as given by the Arden Buck equation, i.e.

the point at which water vapour becomes water (Buck 1981). Keeping the pressure below this point before cooling ensures no water will form on the detectors as they are cooled, and thus no ice once the temperature drops sufficiently.

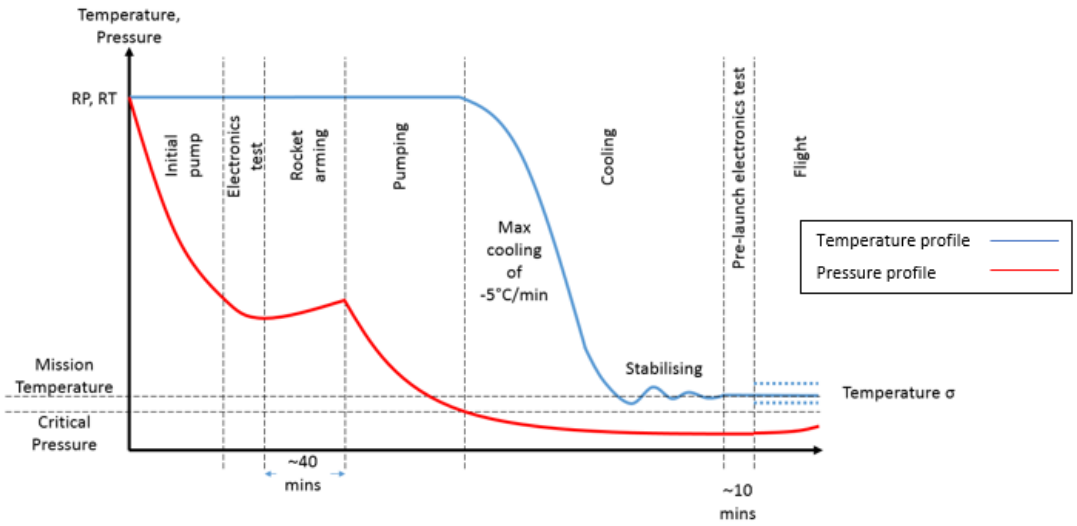

Figure 3-3: The launch day schedule with the blue line representing the camera temperature and the red line represents the camera pressure. This is assuming both pressure and temperature start at resting temperature and room pressure (RT and RP)

During the arming of the rocket all electronics, including the pumps used to create the vacuum, must be turned off. It has been assumed that some leakage will occur and so the pressure will go up slightly during this time. It is also of importance that the devices are cooled at an appropriate rate. The detector manufacturers, Teledyne-e2v, have advised that temperature changes on the device should not exceed 5°C per minute (e2v technologies 2007).

If both electronics tests are successfully passed the rocket will be primed for launch with data obtained whilst still on the launch pad to collect any background signals from the rocket before and during the flight before the scientific data collection begins.

3.4 OGRE design

The OGRE payload (Figure 3-4) consists of three main components: the silicon optics, off-plane diffraction gratings, and an EM-CCD camera. The whole payload must accommodate a 3.5 m throw. A long unobstructed region which allows the resultant arc of diffraction to spread out, along with the camera electronics, vacuum chamber, and device mount. The detectors will be held at a vacuum with gate valves being used once the payload is in space to allow the observations to be carried out.

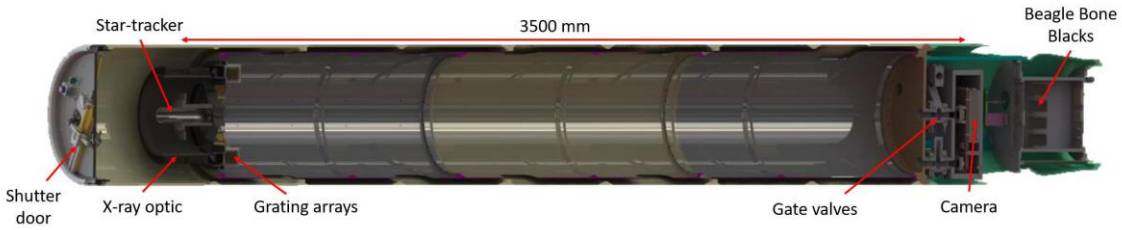

Figure 3-4: CAD of the OGRE payload. The light will enter from the left-hand side once the shutter door opens. Upon launch the right-hand side of this model will be orientated towards the top of the rocket. (Image credit: (Tutt, McEntaffer, et al. 2018))

3.4.1 Silicon optics

X-ray optics are required to focus the photons on a set focal point. The main difficulty with imaging X-rays comes from the angles required to reflect X-ray photons. Unless a shallow angle (usually < 2°) is used the photons will pass straight through or be absorbed by the mirror. The use of a Wolter optics system, where mirrors of varying curvatures are placed in sequence, allows the focusing of X-ray photons to a point. In the case of OGRE, a Wolter type-1 optics system was chosen and is currently being developed by the Goddard Flight Facility. Wolter type-1 optics use a parabolic mirror followed by a hyperbolic mirror to create a focal point with a small focal length (Werner, 1977). The shallow angles required mean a large area of mirror only results in a small collecting area available for the incoming light to be incident upon. To increase the effective collecting area, multiple mirrors are

nested, allowing more light to be focused. Usually these mirrors are made of, or coated with, high density metals such as gold, platinum or iridium, or slumped glass to allow for a higher efficiency in reflection as denser materials offer a greater interacting area to the photons. The OGRE optics, being developed by the NASA Goddard Flight Centre, will instead be made of silicon. With the current manufacturing process, the silicon lacks internal stresses meaning the mirrors will be less susceptible to distortion during the fabrication process and therefore giving a better-quality mirror (Riveros, Kolos, Mazzarella, McKeon, & Zhang, 2015).

Many previous missions have utilised wedge-shaped mirror modules to populate the entire optical layout, for example Astro-H used four quadrants (Soong, et al., 2014). Each wedge holds several nested mirrors with multiple wedges being placed next to each other to increase the collecting area. OGRE will feature a new layout known as a meta-shell which utilises layered mirrors stacked into specially constructed supports structures. This new technique has a lower tooling cost and offers a more precisely defined optical axis. OGRE will be the first use of this new arrangement with silicon mirrors (McClelland, Bonafede, Saha, Solly, & Zhang, 2016). This arrangement will be further discussed in section 5.10.1 of this thesis.

3.4.2 Off-plane gratings

Once the light has been reflected through by the two mirrors it will be sent towards the off-plane gratings. Diffraction gratings are placed perpendicular to the incident light, i.e. off-plane (Figure 3-5), with photons passing through them and creating a resultant arc of diffraction with the position along the arc being dependent on the photon energy. These gratings are easy to manufacture at a low cost however the transmitting nature causes some light to be lost as photons are likely to be absorbed by the material.

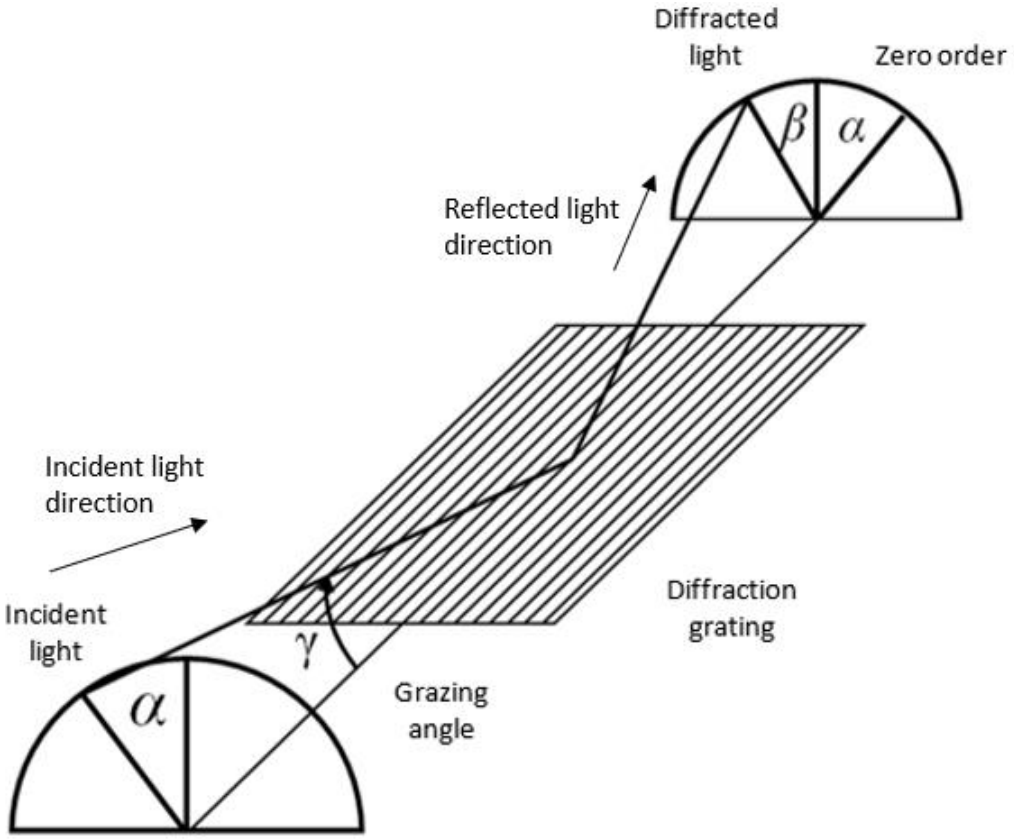

Figure 3-5: Light is incident upon the diffraction gratings at an angle α from the normal and approaching at a grazing angle γ from the plane of the grating. If the blaze angle of the grating is equal to α, the diffracted light will be incident between the zero order and angle β (Image credit: (DeRoo, et al. 2016)).

OGRE will use reflective gratings in an off-plane configuration. They are being developed by a team at Penn State University, the same group who worked on the off-plane gratings for the OGRESS mission who will be using their findings from that launch to improve the gratings used for OGRE. The gratings will be placed quasi-parallel (~2.5°) to the light path and will disperse the light into a diffraction arc.

Placing the gratings in an off-plane orientation provides several benefits over the on-plane arrangement. The off-plane gratings do not suffer from vignetting at higher orders resulting in a better resolving power for the spectrometer (Peterson, et al., 2015). Another advantage is that off-plane gratings allow the grooves to be fully illuminated when aligned

to the focal axis whereas in-plane gratings experience groove shadowing resulting in a drop in efficiency. Considering that Wolter telescopes lose some of the incoming light due to the nested optics it is crucial that the gratings efficiently handle the light that is incident upon them thus the off-plane approach is favoured. For this reason, these gratings are layered in a manner like the optics allowing each mirror to reflect onto its own grating. The stack of these gratings is referred to as a grating module.

One of the greatest benefits to the off-plane gratings is the fact that the light does not pass through them. This allows the gratings to be shaped in such a way that the light can be prioritised to certain parts of the arc of diffraction. Triangular grooves are etched into a silicon wafer causing the incident light to be preferentially focused to one side of the zeroth order creating what is known as a blazed profile.

By utilising this profile, the light will be diffracted to one side of the zeroth order rather than both sides (Figure 3-6). This is beneficial as the area of the focal plane is reduced without affecting the resolution of the arc, i.e. if the arc were fully populated you would now have twice as many photons at each point. As there will be a relatively low photon rate during the OGRE launch it is highly unlikely that two photons of the same energy will be incident at the same time so the main advantage from this is a reduction in the number of detectors needed.

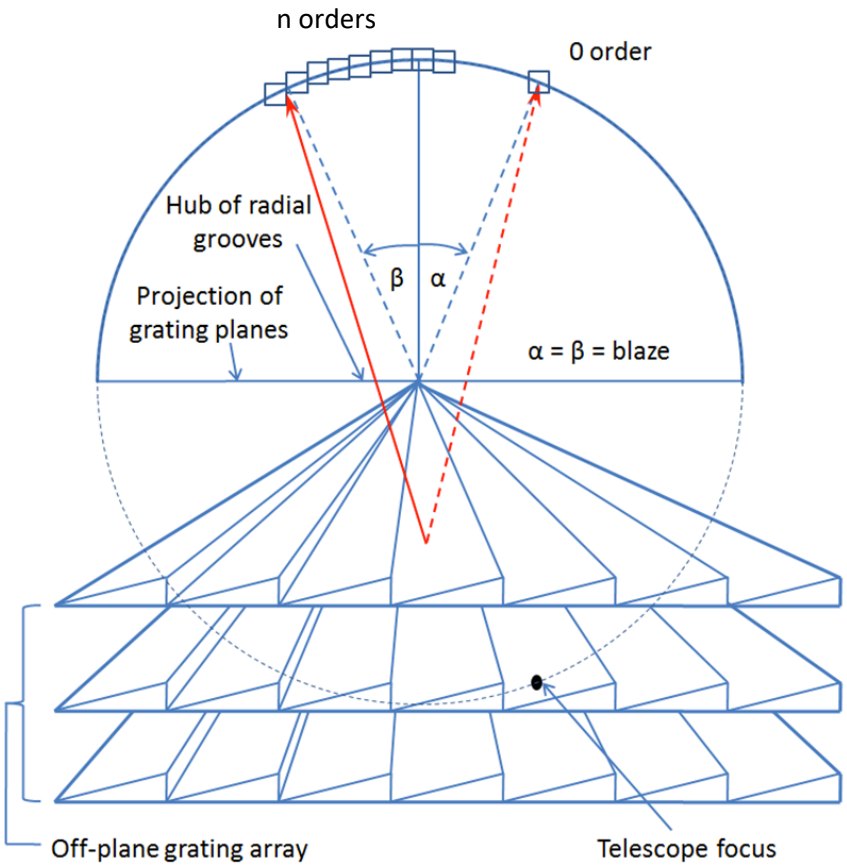

Figure 3-6: The light path as observed from the gratings showing the preferential dispersion towards one side of the zero-order due to the blazed profile. (Mcentaffer, et al. 2013)

3.4.3 The focal plane

The initial design of the OGRE focal plane would have seen three arcs of diffraction stacked vertically with a slight separation (Figure 3-7). This would allow for a large proportion of the arcs to be observed over multiple orders. One detector would be located at the zero-order location whilst the other two devices would be in regions where the desired photons were incident. The fourth detector could have been obscured from the light path and used as a background monitor.

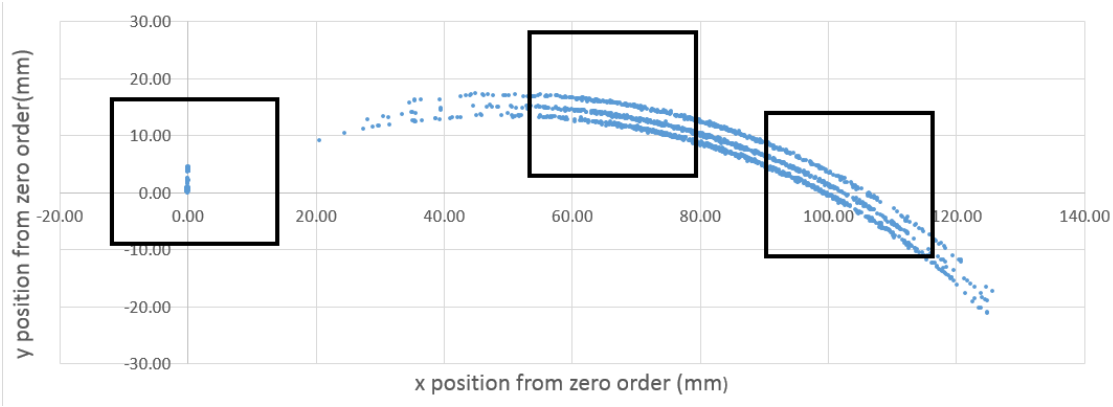

Figure 3-7: The initial OGRE focal plane design. The three blue arcs show the simulated positions of photons after passing through the optics and gratings whilst the black squares show the imaging areas of the EM-CCD devices (Lewis, et al. 2016).

Whilst this would have been useful to maximise the area of the arc observed, it would not have been possible to differentiate which of the three possible light paths the photon had taken. The inherent nature of the previous components means the photons will not fall on a single easily defined line. The photon location has a degree of uncertainty which presents itself as a 'bow-tie' shaped area of where a photon at a given energy can be observed known as its point spread function. This scatter means the three lines would overlap and so the exact location the photon would ideally be incident would be lost in a cloud of uncertainty. As it is the position on the device which is important in determining the energy of the photon it was therefore required to increase the separation of the arcs. An alternative design was put together to achieve this.

3.5 EM-CCD Camera

The OGRE EM-CCD camera has the important job of ensuring the light incident upon it after diffraction has occurred is successfully read out into an image. The camera comprises of four EM-CCDs, three for observing the X-rays and a fourth that is being used to monitor the optical light from Capella to monitor the pointing accuracy of the rocket. The detectors are operated using a dedicated and self-contained electronics system.

3.5.1 OGRE camera overview

The primary aims of the OGRE camera are to allow the user to easily define operating parameters (voltages, timings, etc), control the capture of images, and receive them in a format which is suitable for use at the time of operation. The camera hardware can therefore be split into three sections:

1) The operating computer: The user can change variables and commence operations from here as well as receive images captured by the camera. This computer is a ground-based component and will not be on-board the rocket at launch.
2) The OGRE motherboard: This component is housed in its own case with grounding provided internally to ensure optimal operating conditions. The functions of this board will be discussed in the following sections and can be seen in Figure 3-8.
3) The OGRE headboard: This board is connected to the EM-CCDs via through-vacuum feedthroughs and flexi circuits. This board also converts the signal from analogue to digital as well as filtering biases.

3.5.2 Power supply and conditioning

The final OGRE payload will be operated using a 28 V battery which when fully charged will briefly deliver 34V before degradation starts. As the detectors need to be powered with a constant voltage, power conditioning has been built in to ensure that the camera operates steadily. For the prototype testing an external power supply is kept at a constant 28 V to ensure the camera operates at the voltage specified in the initial design specifications. A temperature controller has been built in to allow the appropriate power to be passed to the heater coils in the final flight build. The heater supply is driven from a second 28 V battery, ensuring redundancy between the two systems.

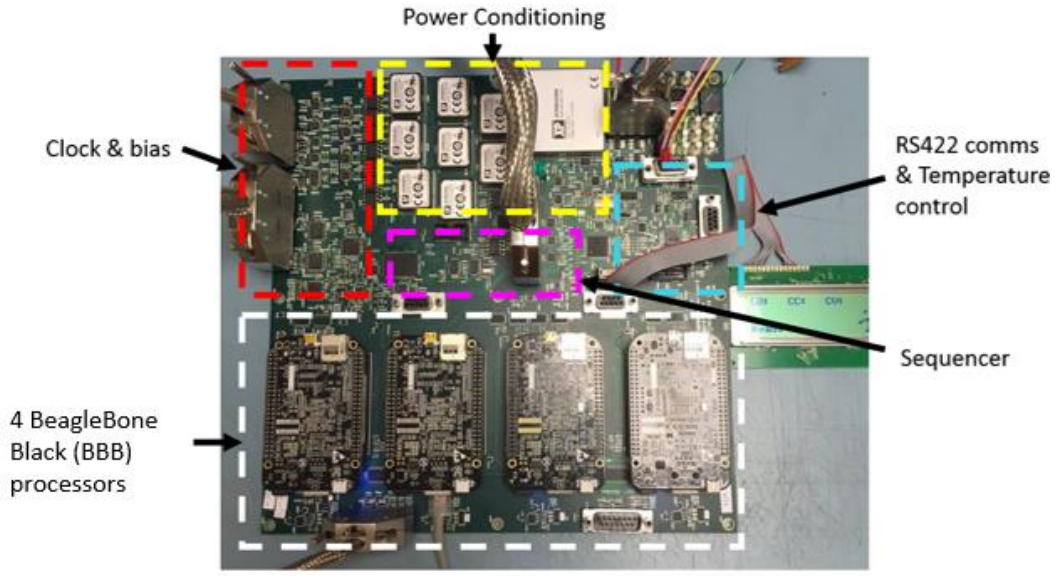

Figure 3-8: The OGRE motherboard with labelled sections to highlight the main features built into it. A diagnostic screen can be seen to the right used upon initial setup of the board on the production line.

3.5.3 Bias generation and supply

The operation of an EM-CCD requires highly configurable voltages which change at a rapid rate. The bias applies a constant voltage to the device where needed.

3.5.4 Clocks and sequencing

To operate the devices a sequencer is used to control the timing of the clock voltages supplied to the detector. This allows the manipulation of the charge generated within the device and is used to optimise the capture of the image as well as the transfer of the charges to a readout node. The timing of the clocks is optimised to balance the readout noise with the readout rate, ensure that charge is transferred through the device efficiently, control the duration of the integration time, and synchronise the readout with the sampling of the ADCs.

The sequencer is key in how the detectors are operated with a variety of operational modes being defined by this code. For example, if the user wished to combine pixel charges to generate a smaller image, i.e. binning the pixels, the sequencer would be programmed to ensure the charge packets are moved and enable this to occur before readout.

3.5.5 ADCs and amplifiers

The incident photons generate electrons within the silicon of the device which are held within a pixel by the electrodes. The electrons held within a given pixels space will be referred to as a charge packet. This charge packet is read out of the device as a voltage and is passed to the Analog-to-Digital Converter (ADC) which transfers this voltage into a digital value. The number sent back to the user does not have any units, it is just a Digital number (DN).

As there is noise inherent in the operation of the detectors the background observed in the device will have some variation. The average of this background, assuming no electrons are found in the background, is the zero-signal level. If a signal is present and its energy known a conversion can then be found to switch the DN back to an energy value.

3.5.6 BeagleBone Blacks and data management

Each of the four detectors connects to a BeagleBone Black (BBB, (Kridner 2017)). These small Linux-based computational systems can process the data sent to them to extract useful data. Each BBB can host an SD card allowing the full data to be stored safely so it is unaffected by any on-board processing. The processed data is then passed to the communications unit via the BBBs RS422 link.

3.5.7 Data communications

An RS422 communications port will connect to the rocket's telemetry device provided by NASA. As the data stream is limited in the speed it can send data back (approximately 1 MB s^{-1} (McCoy, Schultz, et al., A primer for telemetry interfacing in accordance with NASA standards using low cost FPGAs 2015)), processed data will be telemetered as it will require less bandwidth in the stream than sending back all the full images. With each image from a single detector being as large as 3.5 MB, and four images being generated at an ideal frequency of 1 Hz it becomes apparent that all the data cannot be sent down and so event-processing will be utilised to send only the positions of incident X-ray photons along with the zero order positions.

3.6 The prototype OGRE data flow

A series of communications between the three main OGRE components allows for proper use (Figure 3-9). The labels in this diagram refer to the following processes:

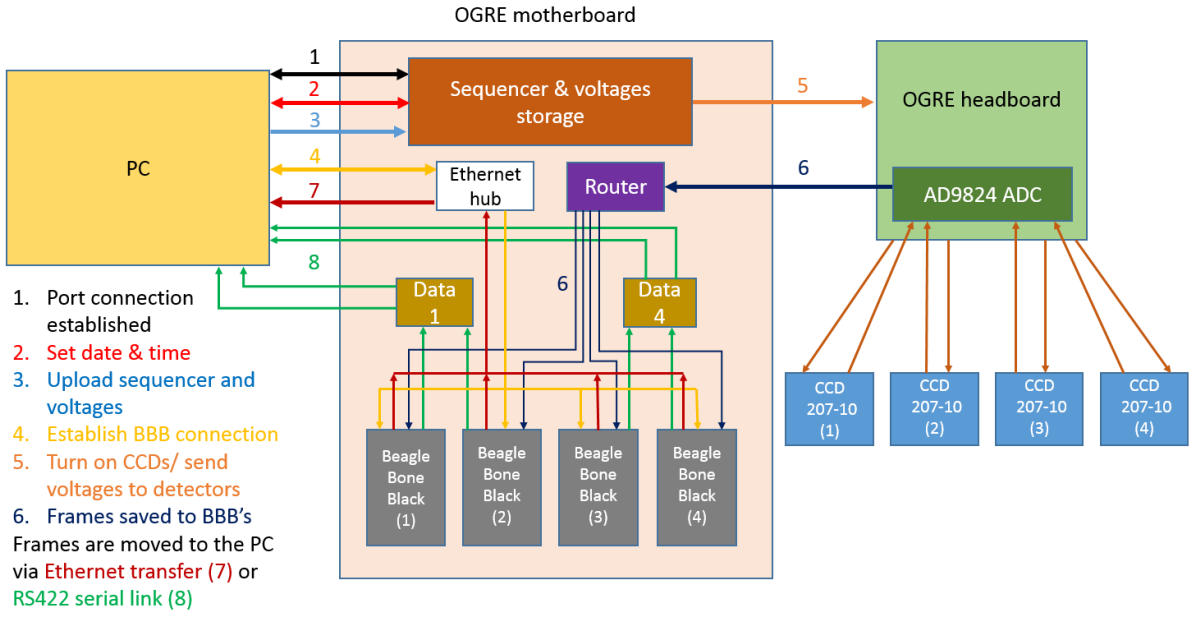

Figure 3-9: The operational pathway of the OGRE system showing the directions and order of information transferral.

1) A serial port connection must first be established between the computer and each of the BeagleBone Black units. The use of a BBB for each detector allows for a

direct connection to each allowing simple transfers of information to precise handling of each detector.

2) The motherboard resets to factory default dates and times whenever it loses power. To allow for the saving of files in a manner which equates to the actual time of use the date and time is uploaded to the camera system when it first turned on. This is then stored on the motherboard for the duration of its operation.
3) The sequencer which operates the camera can be hard saved onto the motherboard, however it is usually desirable to easily change between sequencers or operating voltages. The system allows for these changes to be quickly made before camera operations occur. A simple cell and command structure can change the operating voltages and the timings of the voltage signals.
4) For inspecting the BBB operating system and file system structure during ground testing, the BBBs are connected to the host computer using an Ethernet interface, with MATLAB's built-in BBB library. The camera control script can then automate beginning data capture by calling executables on the BBBs, followed by data retrieval from each of the BBB's file structure. The flight camera will store the data onboard and transmit event data packets over dedicated RS422 serial data connections.
5) A single command can be used to start, or stop, sending the voltages to the CCDs to allow for operations. Depending on the test required a script can then be run to allow for data collection and handling whilst ensuring all resultant images are saved into relevant locations.
6) Whilst running, the devices operate in the manner described later in chapter 4 to convert the photons to an electrical signal and to read out an image. The OGRE camera saves these images onto the BBB's hard storage section. If images are already present when the image acquisition starts, any images are removed to

ensure enough hard drive space is available for the incoming data. Image frames are named frame_# with the # being the image number (starting from 0) since this data acquisition began. In some tests where an operating parameter is changed, the number resets as data collection is stopped whilst changing the parameter value.

Once the data acquisition has finished the resultant images can be transferred back to the user computer in one of two methods.

7) Once the acquisition has finished the data is transferred via Ethernet into a relevant storage location on the computer.
8) The data is processed by each BBB into an output string which is then sent via a RS422 serial link. This is the connection which shall be used for the communication with the telemetry stack during flight.

3.7 Telemetry of data

It would be incredibly useful to get feedback from the rocket during its flight to ensure it is operating optimally. The data passed down can then be processed by a Graphical User Interface, or GUI to give a 'live' update on the camera's performance. The data will be passed from the rocket to the ground via a NASA telemetry stack.

3.7.1 Available telemetry stacks

NASA's Wallops Flight Facility, the providers of the rocket bus for OGRE, have three different telemetry modules available for use (NASA Goddard Space Flight Center 2015).

Table 3-2: The available telemetry stacks which could be used for OGRE (NASA Goddard Space Flight Center 2015)

Telemetry Stack	Bit Rate	Word Length	Frame Size	Parity	Output code	Frame/ subframe
WFF93	78 kb to 10 Mb	8 – 16	Up to 8k words	None	BIΦL, M, S NRZL, M, S RNRZL Conv NRZM Conv NRZL	Limited to 8k
MV Encoder	Up to 20 Mb/s	8 – 16	Up to 130k words	None	BIΦL, M, S NRZL, M, S RNRZL Conv NRZM Conv NRZL	Limited to 32k
Mesquito	Up to 2 Mb/s	16	Up to 64k words	None	NRZ-L Radomized	Limited to 64k

It is highly likely that OGRE will be using the WFF93 system. This is a highly configurable stack allowing for multiple modules to be added to fit certain purposes. The module chosen affects the number of channels possible as well as the length of the strings that can be sent down. The large diversity in the modules available as well as the ease with which the telemetry stack can be set up means that the stack can accommodate the requirements of the command and control and data return RS422 serial interfaces.

3.7.2 The data rates of the camera

Once the frame on each device has been analysed the event processing will need to output the event data into a string to be sent down via telemetry and later 'translated' by the GUI. For that reason, each event output must take the same form. It may also be possible to send back a diagnostic string which updates the GUI on information not related to the X-ray events such as the device temperature or the amount time that has passed since capture was started. The two strings could use different starting characters to allow the GUI to identify which string is being passed to it.

The baud rate of the camera is a factor that must also be considered. This measure of the number of bits that can be sent out per second limits the number of X-ray event packets that can be sent out for each frame. This is currently set up to be 57.6 kb/s on each COMS output. The WFF93 telemetry stack can handle between 78 kb/s to 10 Mb/s so could potentially handle maximum capacity readouts from each of the four COMS channels OGRE can use.

The 'words' within each string sent to the telemetry stack can be 8 or 16 bits long with frames containing up to 8000 words. Some of the information to be sent back may therefore have to be 'bulked up' to ensure the data is properly sent. Each string must also end with a Frame Sync signal in the same place each time to ensure the telemetry stack is reading out at a constant working rate.

3.8 On-board data storage

To ensure the data is maintained for later analysis the frames obtained from each device will first be saved to on-board storage. The BeagleBone Blacks allow for micro-SD card storage as well as having a total of 4 GB of internal on-board storage. Each image file is 3.423 MB meaning only 1168 images can be saved on-board so external storage will be needed to cover the 45-minute operational time. Once this image has been saved, the event processing will occur ensuring the complete data is hard saved on-board.

3.9 Summary

The OGRE mission with its new optical manufacturing and composition, the off-plane diffraction gratings and the first use of an EM-CCD camera system for non-earth observations aims to provide a high spectral resolution soft X-ray spectrum of Capella to greatly encourage the use of these key technologies in potential future missions. Focusing on Capella should allow for comparisons with other notable missions that have also

observed this system allowing a clearer determination of the benefits of upscaling a system like OGRE to a long-term satellite project.

With sounding rocket missions, the system will only have a narrow window of time to demonstrate its capabilities, so it is essential that each of the key components function in a manner allowing for the desired observation to be made to a high degree of accuracy and reliability. Therefore, such extensive testing is carried out on each piece, with the precise characterisations allowing a better idea of how the system will work when it is all brought together.

The silicon optics and diffraction gratings have undergone rigorous testing by the other collaborators in the OGRE projects with a large amount of trust placed in their capabilities. It is therefore paramount that the EM-CCD camera systems can allow for the collection of the expected observations.

4 CCD and EM-CCD theory

4.1 Silicon-based image sensors

The conversion from analogue to digital imaging has largely been due to the invention of silicon image sensors. Previously vacuum tubes were used to capture and display images. The silicon-based Charge-Coupled Device, or CCD, was invented in 1969 by Boyle and Smith who had worked previously on magnetic-bubble memory (J. J. Janesick 2000). The bubbles were small, magnetised areas which could be moved along tracks when an external magnetic field was exerted on them and they were pushed into a conventional magnetic pickup. They realised that these basic principles could potentially be used with a 'charge-bubble' using semiconductors and the manipulation of the potentials applied to the device.

These ideas were successfully tested and then improved upon to allow for photon-generated charge signals to form within the device and be read out (Boyle and Smith 1970). The CCD proved a success which would go on to be used in many scientific projects including satellites whilst paving the way for other imaging devices such as Complementary Metal-Oxide Semiconductors (CMOS) which can be found in many imaging devices today, such as mobile phone cameras and webcams.

The incredible impact of Boyle & Smith's CCD work led to them being awarded the 2009 Nobel Prize for physics along with other national awards and prizes for their pioneering work.

4.2 Semiconductor theory

4.2.1 The crystalline structure of silicon

CCDs take advantage of the properties of silicon and the ability to dope its crystalline structure to meet the required needs. Each silicon atom has an electron configuration with

four electrons in its outer shell allowing it to form a covalent bond with four neighbouring silicon atoms forming a diamond cubic crystalline structure (Figure 4-1). Doping silicon using either phosphorous or boron atoms changes the material's properties to behave as an n-type or p-type semiconductor, respectively. An n-type semiconductor contains additional free electrons due to phosphorous containing 5 electrons in its outer-shell, 4 of which bond to neighbouring silicon atoms. The remaining electron is free to be a charge carrier in the conduction band. A p-type semiconductor contains additional holes due to the boron only containing 3 electrons in its outer-shell. This means only three of the crystalline bonds are complete with the hole being a charge carrier in the valence band.

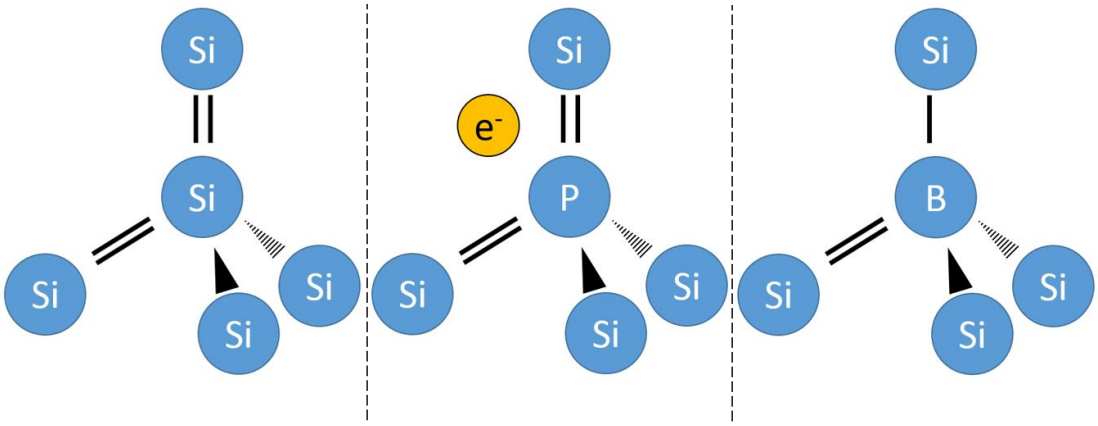

Figure 4-1: The tetrahedral molecular geometry of a pure silicon crystal (left) an n-type semiconductor/ phosphorous doped silicon crystal (middle) and a p-type semiconductor/ boron doped silicon crystal (right).

4.2.2 The p-n junction

Bringing the two semiconductor types together allows the additional electrons to combine with the holes. As the p-type semiconductor contains negatively charged atoms which no longer have holes, and so has an inherent negative charge. Conversely positive charge builds in the n-type. These regions prevent further movement of electrons and a new state of equilibrium is reached with a depletion region present (Figure 4-2). When light is incident upon the silicon electrons are generated via the photoelectric effect. The electrons are excited by the photon and move from the valence band to the conduction band leaving a

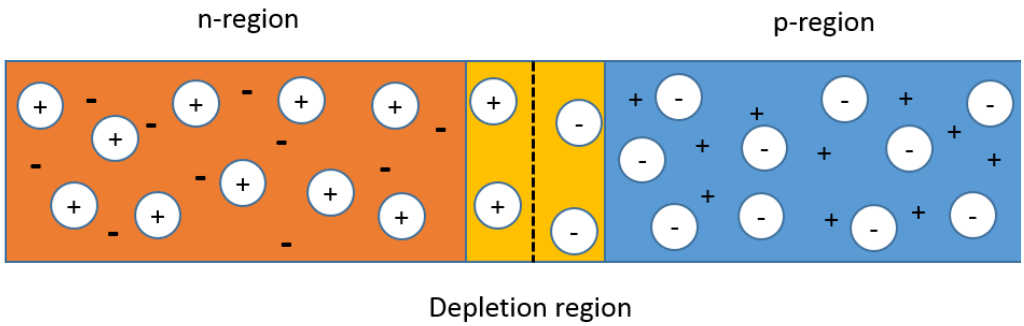

Figure 4-2: The p-n junction showing the two regions in equilibrium with a depletion region which allows the separation of any electron-hole pairs formed there.

hole behind, meaning the photon has generated at least one electron-hole pair. If a photon is incident within the depletion region any electron-hole pairs generated are quickly separated with electrons moving into the positive n-type region and the holes moving into the negative p-type region.

One result of doping the silicon is a change in the material's Fermi level, the energy at which no electrons can escape when at absolute zero. Silicon doped with boron (p-type) has a lower Fermi level than silicon doped with phosphorous (n-type) so if the two are brought together and are in equilibrium, the Fermi levels must align. This causes a change in the potential profile when looking across the semiconductor. The difference between the conduction band and valence band potentials is known as the barrier potential which restricts the movement of electrons and holes within the silicon.

4.3 Charge generation and handling

Once a photon is incident upon the silicon and an electron-hole pair is formed it is desirable for these not to recombine before the photon events are observed. This can be done in a couple of ways but Metal Oxide Semiconductor (MOS) capacitors, are key in both methods.

4.3.1 MOS capacitors

To prevent recombination a Metal Oxide Semiconductor capacitor is used. A gate electrode is held separate from the silicon by a thin layer of oxide to keep it electrically isolated. When no potential is applied to the electrode the semiconductor is left in equilibrium.

4.3.2 Surface channel devices

Applying a negative bias with the electrode near a p-type semiconductor attracts the excess holes towards the oxide/surface layer whilst leaving the rest of the semiconductor in equilibrium.

Applying a positive voltage to this p-type semiconductor will have the opposite effect and repel the holes from the surface creating a depletion region. More positive voltages cause a larger depletion region and, assuming a reasonable positive bias is used, electrons generated thermally or by photons will move towards the surface of the silicon where the potential is lowest, i.e. close to the positively biased gate electrode. This behaviour is why MOS capacitors like this are known as surface channel devices (Figure 4-3). The more incident photons in the region, the more electrons and therefore the higher charge carried towards the gate.

4.3.3 Buried channels

A disadvantage of using a surface channel device is that electrons are held at the oxide-semiconductor interface which contains many electron trap sites. These defects may prevent the uniform flow of an electron cloud by allowing for electron interactions with the semiconductor material. This causes a Charge Transfer Inefficiency (CTI) as some of the electrons may be left behind in the trap sites, resulting in a loss of information before reading the signal out.

To circumvent this issue a buried channel can be formed by using an n-type MOS capacitor along with a p-n junction. By aligning the two n-type regions a depletion region is formed

away from the oxide-semiconductor interface, i.e. 'buried' beneath the surface. As there are considerably fewer trapping sites within the material the CTI is considerably lower than if a surface channel device is used. Applying a greater voltage will increase the depletion region. The potential well in the buried channel can only hold a certain amount of charge without electrons spilling into the surrounding area. This is known as the full-well capacity (FWC).

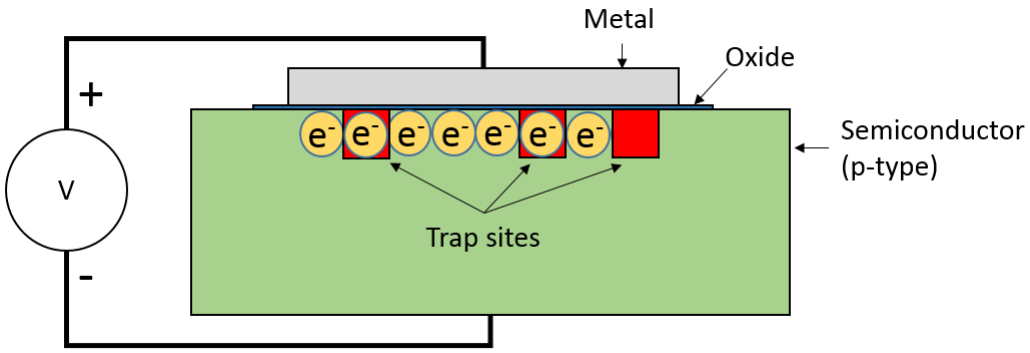

Figure 4-3: Schematic of a surface channel Metal Oxide Semiconductor capacitor with a positive voltage applied to the gate electrode. Also shown are trap sites which are common at the oxide-semiconductor interface.

4.4 CCD Structure

4.4.1 Image section structure

If a two-dimensional image is desired MOS capacitors must be arranged in such a manner that the electrons move into specific picture elements, or pixels. The rows of an image are formed by polysilicon electrodes on the surface of the semiconductor which extend across the width of the image section. The number of electrodes present per pixel determines the phase number of the device; a factor considered with image readout. Each pixel within the image section of the device hosts the same number of electrodes and each electrode is connected to the same circuitry as the corresponding electrodes in every other row, i.e. all the phase 1 electrodes are connected in parallel, as are the phase 2 electrodes etc.

To create the columns channel stops are formed by using boron implants in the surface of the silicon. The boron implant forms p-type silicon with a native negative charge which repels any electrons to provide a clear boundary between the columns. The combination of electrode and channel stop structures define the pixels and allows for any photo-generated electrons to be stored close to their generation point and held separately from any other pixels, assuming FWC is not reached (Figure 4-4).

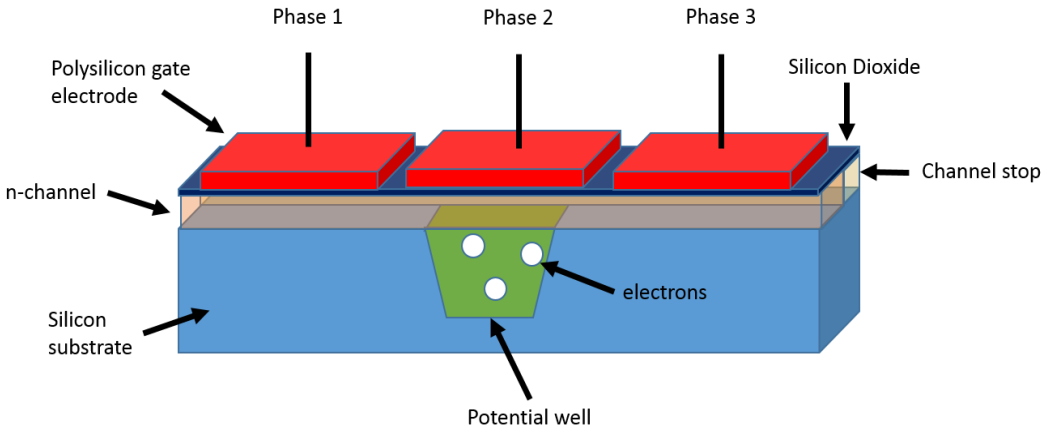

Figure 4-4 The pixel structure of a three-phase buried channel CCD. In this case a positive voltage is being applied to the phase two gate electrode, creating a potential well in which the photogenerated electrons are held.

4.4.2 Front-illuminated vs Back-illuminated devices

CCDs tend to come in two different types: front-illuminated and back-illuminated. With a front-illuminated device, light passes through the electrode structure and into the silicon substrate. The electron-hole pairs form in the silicon at depths dependent on the photon energy. These detectors have the advantage of being able to be thicker and thus more rigid, however by passing the light through the electrode structure some photons will be absorbed before reaching the photo-sensitive silicon.

The back-illuminated device architecture counters the loss of low energy photons by exposing the rear side of the silicon directly to the light. The substrate needs to be thinned to allow the photons to interact close to the electrode structure. The unimpeded light path

causes a higher sensitivity and better quantum efficiency, the probability that an incident photon is detected.

As X-ray photons have short attenuation lengths, they will interact very close to the rear surface. Typical back-illuminated devices may still be considered 'too thick' due to their small absorption lengths which means photon interaction occurs outside the depletion region of the silicon. In this field-free region any formed electrons can diffuse isotropically and be incident upon several different pixels due to the charge cloud having a larger area. This is known as charge splitting (**Error! Reference source not found.**). The rate at which the charge packet disperses has a full-width half maximum (FWHM) of roughly twice that of the distance the packet moves through the field-free region (Janesick, et al. 1987). Charge splitting can be reduced by increasing the electric field across the device which increases the depth of the depletion region and thus decreases the distance in which lateral diffusion can occur. Larger pixels also reduce the effect of charge splitting but give a poorer spatial resolution.

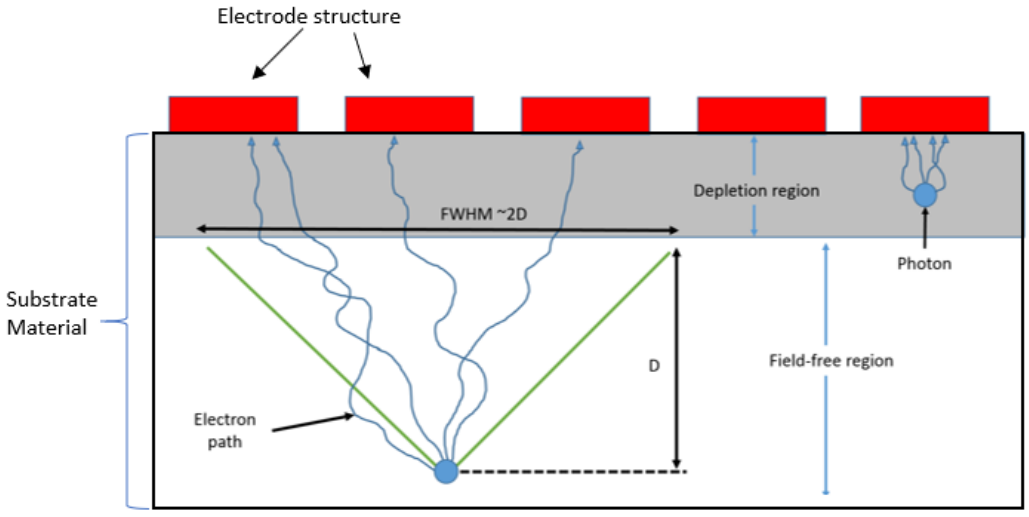

Figure 4-5: The motion of electrons towards pixels for two photons of equal energy forming in different regions of the detector. The photon incident with the field-free region interacting at a depth D into the field free-region generates electrons which can diffuse across multiple pixels whereas the photon incident in the depletion region is strongly attracted towards the pixel so does not diffuse as much.

4.4.3 CCD readout

As each pixel does not have its own readout the charge must be transferred across the array. Each pixel generally features at least three different polysilicon gate electrodes which extend across the entire row to allow a three-phase readout. This allows the potential on a gate electrode in each pixel on a row to be changed at the same time. By holding the gates at various voltages it is possible to collect charge as well as move it (Figure 4-6).

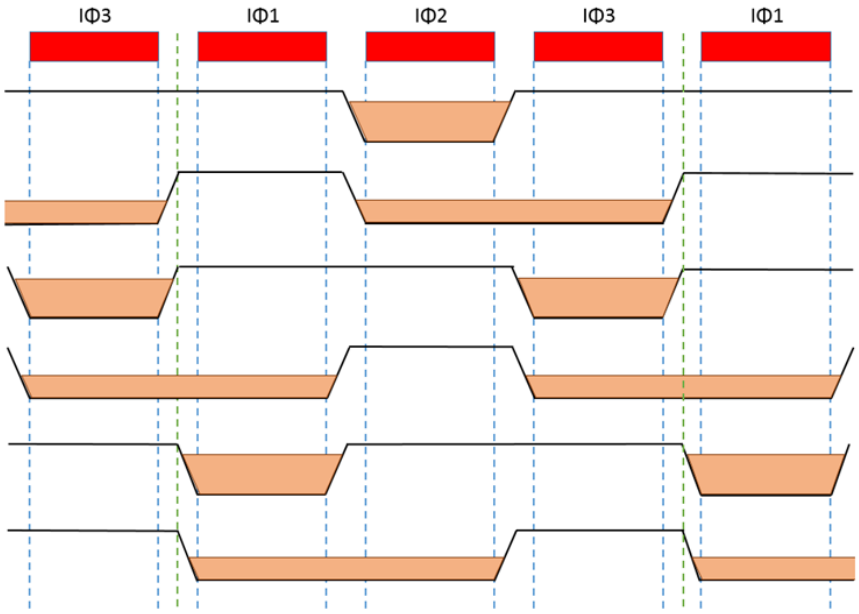

Figure 4-6: The transfer of charge, represented here in orange, across the gate electrodes allowing the charge packet to be moved down a pixel. The pixel boundary (green dashed line) can be seen showing the charge moving from one pixel to another.

These three electrodes in the image section are referred to as IΦ1, IΦ2 and IΦ3. Whilst the photons are incident upon the silicon IΦ2 is held with a high voltage thus attracting the resultant electrons towards it. Once the photon collection for the image is finished, IΦ3 is increased to the same voltage as IΦ2, allowing the electrons to be shared across the two electrodes. IΦ2 is then reduced and due to the positive voltage on IΦ3 the electrons are all moved to this electrode. The IΦ1 electrodes are then given a positive voltage allowing the electrons to be shared over the pixel boundaries briefly before IΦ3 is reduced leaving the

charge packet in the next pixels' IΦ1. A similar process occurs to shift the charge into IΦ2 meaning the charge packet has moved down one pixel.

The row of pixels that have been shifted at the end of the array will have been moved down and into a serial register after this cycle occurs (Figure 4-7). Each pixel in this register must be read out individually before the next row of pixels can be moved down. A similar process is utilised with three electrodes, orientated perpendicular to the previous system. These electrodes are referred to as RΦ1, RΦ2 and RΦ3. By procedurally changing the voltages across the electrodes the charge packets can be moved across. An output node is located at the end of the serial register which allows the charge packet to be converted into an output voltage. Every cycle of the RΦ electrodes reads out one pixel and so this is repeated for the number of columns present in the array to read out the row in its entirety. Once this is done and the serial register is empty, the process repeats until every row in the array has been read out.

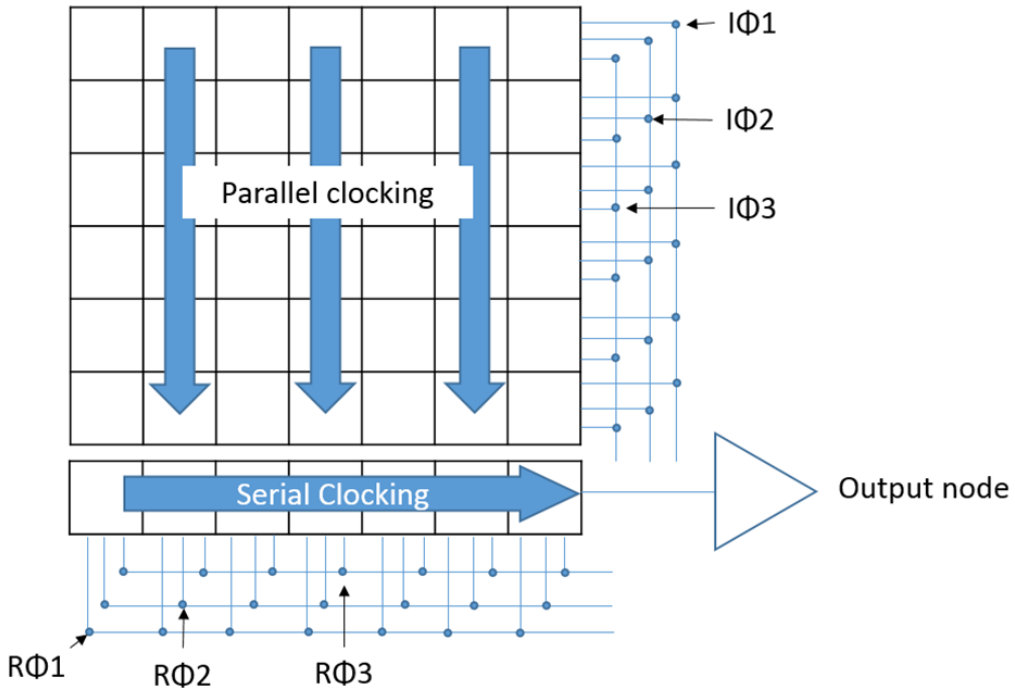

Figure 4-7: Schematic of a typical CCD with the read-out directions and electrode circuitry shown.

The output node, generally a heavily doped n-type region with a parasitic capacitance C_n, stores the charge packet before it is converted to a voltage by a load resistor, R. Using a reset transistor and output transistor built into the silicon wafer it is possible to reset the output node, retrieve the signal charge packet and then output the signal as a voltage. A gate voltage is used to allow the charge to come from the serial register into the output node. While the charge packet is held back, the node is reset by applying an 'on' voltage, known as the reset clock (ΦR) to the reset transistor. This allows the reset drain potential (V_{RD}) to charge the output node to the same voltage. Changing ΦR to zero leaves the output node at $V_{RD.}$ When the output gate is 'opened' and the signal charge passes into the output node, the voltage change is detected by the output transistor and an output voltage generated.

4.5 Noise Sources

Some noise is inherent from the systems employed to convert the charge packet to a voltage. Ideally a large-signal to noise ratio is present when reading out an image from a CCD to give high confidence that the values observed are close to that due to incident photons rather than noise in the system. Noise can originate from several areas within the device though.

4.5.1 Shot noise

Each photon event in a substrate will not necessarily produce the same number of electrons. Looking at the mean number of electrons generated per photon event, n_e, shows a Gaussian distribution with a standard deviation of $\sqrt{n_e}$. This deviation is known as shot noise. The mean number of electron-hole pairs that will be generated by a photon interaction event can be predicted by considering the quantum yield of the substrate material.

The Fano factor, f, is a reduction in the shot noise from a CCD based on the medium being used to detect the photons. For silicon, any X-ray photon event produces many electrons

with others forming due to impact ionisation. Each electron generated via the impacts must form from a silicon atom within the substrate so each time this occurs the number of electrons the lattice can provide is reduced. This causes the potential charge packet size to be constrained. The distribution width in the number of electrons generated from a single X-ray in the silicon can be calculated using the Fano factor, the energy of the incident photon, E, and the quantum yield of silicon, ω, using equation 4-1.

$$\sigma_{shot} = \sqrt{f n_e} = \sqrt{f \frac{E}{\omega}} \qquad 4\text{-}1$$

4.5.2 Dark Signal

Thermal excitations due to mechanisms within the silicon substrate can occasionally lead to the formation of e-h pairs without a photon interaction occurring and thus is known as dark noise. The electrons from this can be detected as part of a signal packet despite them originating from the detector itself. This is known as dark signal and as it can occur in any pixel region in the device it is generally expressed in units of electrons per pixel per second.

The number of electrons generated by dark signal per cm^2 is defined using equation *4-2*

$$\sigma_{dark} = \frac{Nq}{At} \qquad 4\text{-}2$$

where N is the electrons generated per pixel per second, q is the electronic charge, t is integration time and A is the area of the pixel. This value allows for simple direct comparisons between different devices regardless of pixel structure/size.

The dark current, the dark signal per second, can be suppressed by clocking the device in inverted mode. Increasing the substrate voltage allows holes to accumulate at the front surface. Any dark signal that would be generated here is promptly recombined with the holes thus not contributing to the signal charge packet. Dark current is also greatly suppressed by

running at low temperatures (e.g. -80°C can give results of less than 1 electron per hour per pixel (Li and Nathan 2005)) so these different methods of suppression, or a combination of the two, can be utilised for a variety of different experiments.

4.5.3 Clock-induced charge

As the gate electrodes are clocked and move the charge across the detector, some electrons can be generated due to impact ionisation. These extra electrons add Clock-Induced Charge (CIC) to the charge packet. CIC increases when the device is operated in inverted mode, which involves operating the electrodes with a sufficiently negative voltage to allow holes to be attracted to the surface. The holes in the silicon are accelerated towards the electrodes and cause impact ionisation to occur releasing more electrons. Running a device at low temperatures in non-inverted mode will largely suppress CIC but if inverted mode is needed CIC can be reduced in two ways; using image area clocks to set the gate electrodes to a low voltage thus reducing the electric field generated and thus the acceleration of holes, and to have slower clock transitions so the electric field is not changed so rapidly.

4.5.4 Reset noise

Ideally the reset node is set to V_{RD} for every pixel, however there is a slight fluctuation in the actual voltage the node reaches for each reset as well as changes in the node temperature over time. This is reduced using Correlated-Double Sampling (CDS) which requires measuring the output after the reset to determine the actual reset level and sampling the output again once the pixel charge has been moved into the node. As both readings will contain the actual V_{RD} on the node for that pixel, the difference can be found and thus the signal voltage extracted. Two types of CDS that can be utilised are Clamp and Sample, and Dual Slope Integration. Clamp and Sample takes the voltages at points as described earlier to find the difference. Dual Slope Integration takes an average across the points for a set time. When looking at the reset level, the charge is integrated negatively onto an op-amp integrator to

the set time. Once the signal is passed onto the node, a positive integration is applied for the same time period. As both signals will feature the average V_{RD} values over this time the resultant charge is equivalent to the signal, thus the effects of the noise are reduced. Using a longer sampling time for the integration allows for a more effective noise removal.

4.5.5 Readout noise

The output circuit is also susceptible to noise due to the random thermal motions of electrons. As electrons move through the output circuit, they can collide with the lattice and generate thermal noise. This was quantified by Johnson and Nyquist (equation 4-3) where the r.m.s. readout noise voltage ,$\sigma_{readout}$, is related to the Boltzmann constant, k, the absolute temperature in Kelvin, T, the noise power bandwidth, B, and the resistance of the circuit in ohms, R.

$$\sigma_{readout} = \sqrt{4kTBR} \qquad 4\text{-}3$$

Using dual slope integration Correlated-Double Sampling (CDS) can reduce the effects of this, especially if longer integration times are used. This does impose a problem though as if a longer integration is used the read out will take longer. Clamp and sample CDS is quick as it only uses one point before and after the signal is passed to the output node, but due to the singular point there is greater noise. It is therefore obvious that there is a delicate balance between speed and noise in traditional CCDs.

This is not the only balance that must be delicately handled when it comes to the output circuit. The capacitance of the output node affects the responsivity of the device which could potentially restrict the signal that can be observed. A lower responsivity will increase the range of energies that can be detected without saturating the output node. A higher responsivity allows smaller changes in the signal to be seen so overall the device becomes

more sensitive. This means a large range of energies with high sensitivity is not possible, so output nodes need to be chosen based on balancing out the range and sensitivity.

The CCD circuitry can be triggered to readout signals without manipulating the positions of the charge within the image area of the device. This gives a signal output equating to the additional signal generated from the device's operation alone. Generally, a large section of the output is dedicated to serial under-scan taken before each row in the image is read out. There is a small serial over-scan after the row has been read and ensures the serial register is emptied after each row in the image section is read out. Both regions contain the closest to a zero signal in the image, so any values found here are due to dark current in the device. Parallel over-scan and under-scan adds non-existent rows to the image section which can also be sued to determine the devices operational performance (**Error! Reference source not found.**). All these regions can be used to determine the noise present in the device.

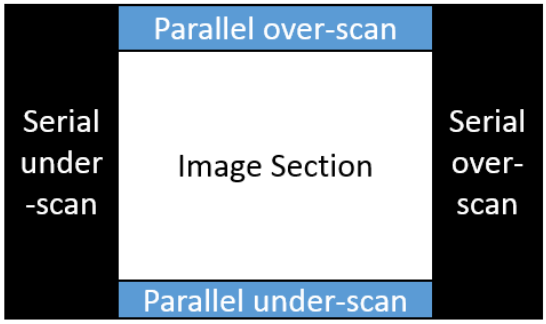

Figure 4-8: The sections of a CCD output image with the additional regions generated by reading out signals that are not from the image section of the device.

4.5.6 Total noise

If the proper precautions are put in place the noise contribution due to CIC and resetting are negligible. To find the total noise in the system the separate noise elements must be added in quadrature (equation 4-4).

$$\sigma_{total} = \sqrt{\sigma_{readout}^2 + \sigma_{dark}^2 + \sigma_{shot}^2} = \sqrt{\sigma_{readout}^2 + \sigma_{dark}^2 + \mathrm{f}\frac{E}{\omega}} \qquad 4\text{-}4$$

As the peak for pixel values has a Gaussian shape it is useful to know how much this value can vary, i.e. how wide the peak is. The spectral resolution of a detector can be determined by its Full Width half Maximum (FWHM) value. This value, as the name suggests, shows how wide, or narrow, the Gaussian is when at half the maximum and so devices with smaller FWHMs have a much better resolution. The equation for the FWHM can be derived from the Gaussian function (equation 4-5).

$$f(x) = \frac{1}{\sigma\sqrt{2\pi}} e^{\frac{-(x-\mu)^2}{2\sigma^2}} \qquad 4\text{-}5$$

Here, σ is the standard deviation, and μ is the mean. As the first term is a constant scaling factor and the function at FWHM is equal to 0.5, equation 4-5 reduces to equation 4-6.

$$e^{\frac{-(x_0-\mu)^2}{2\sigma^2}} = \frac{1}{2} \qquad 4\text{-}6$$

where x_0 are the half maximum points. Finding x_0 and remembering that these two points are on different sides of the mean value leads to the FWHM equation:

$$FWHM = 2\sqrt{2ln2}\,\sigma_{total}\omega \approx 2.3548\sigma_{total}\omega \qquad 4\text{-}7$$

The multiplication by ω changes the units of the calculation to the more conventional eV. As the equation features a constant before the noise value comparisons between the values of various devices can be easily compared to effectively compare the noise present.

4.6 The Electron Multiplying CCD (EM-CCD)

In section 2.5.1 GEM detectors were discussed as being used by the OGRESS mission to increase the number of electrons generated by an incident photon. One disadvantage of GEM detectors is that they have considerably larger pixels than standard CCDs, so the resolution is significantly worse. Standard CCD structures are unable to use a gaseous medium to obtain electron multiplying but generally offer smaller pixel sizes, and thus better resolutions. EM-CCDs aim to have both advantages in one device.

EM-CCDs are incredibly similar to standard CCDs. There is still an image section which uses several polysilicon electrodes per pixel to shift the rows into a serial register. Some EM-CCDs can be read out like a standard CCD. These detectors feature two outputs; a High-responsivity (HR) output which offers a non-specialised output for standard CCD operation, and a Large-signal (LS) output for a multiplied signal.

4.6.1 The multiplication register

The large-signal output has several additional features which allow for the signal to be multiplied. Additional corner elements are needed to carry the charge to the multiplication when LS mode is in use (Figure 4-9) however these act like a standard register element to move the signal across each element. The biggest difference when using the LS output is the addition of a multiplication register between the serial register and the output node. This new register, which is usually comprised of several hundred elements, utilises impact ionisation to increase the number of electrons in a charge packet.

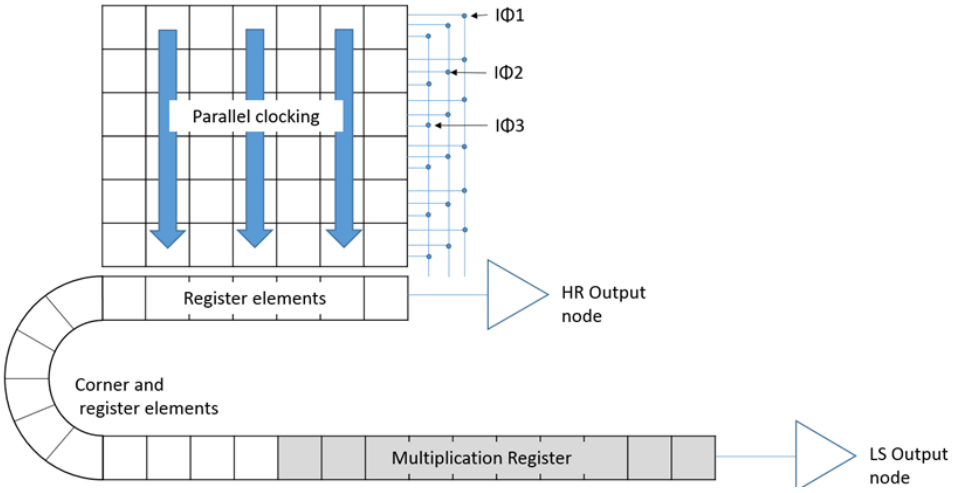

Figure 4-9: Schematic for a standard EM-CCD with two modes of operation.

The register moves packets across in a similar way to the serial register, however as RΦ2 uses higher voltages than standard CCD electrodes (approximately 50V) it is referred to as RΦ2HV. An additional element, known as RΦDC is placed before RΦ2HV and acts as a controlled barrier height for the charge packet. Rather than being switched between open and closed voltages, RΦDC is held at a low, constant voltage (approximately 2V). When RΦ1 is given a voltage larger than RΦDC the charge is to one side of the barrier. When RΦ2HV has reached the desired potential, RΦ1 is set to zero allowing the electrons to be accelerated across RΦDC and into the large potential well of RΦ2HV. This maximises the chances of impact ionisation occurring and a new electron-hole forming. The newly formed electron joins the charge packet, increasing it. The usual packet movement procedure is carried out to move the charge into RΦ3 and the next elements RΦ1 for the cycle to repeat for each element in the multiplication register (Figure 4-10).

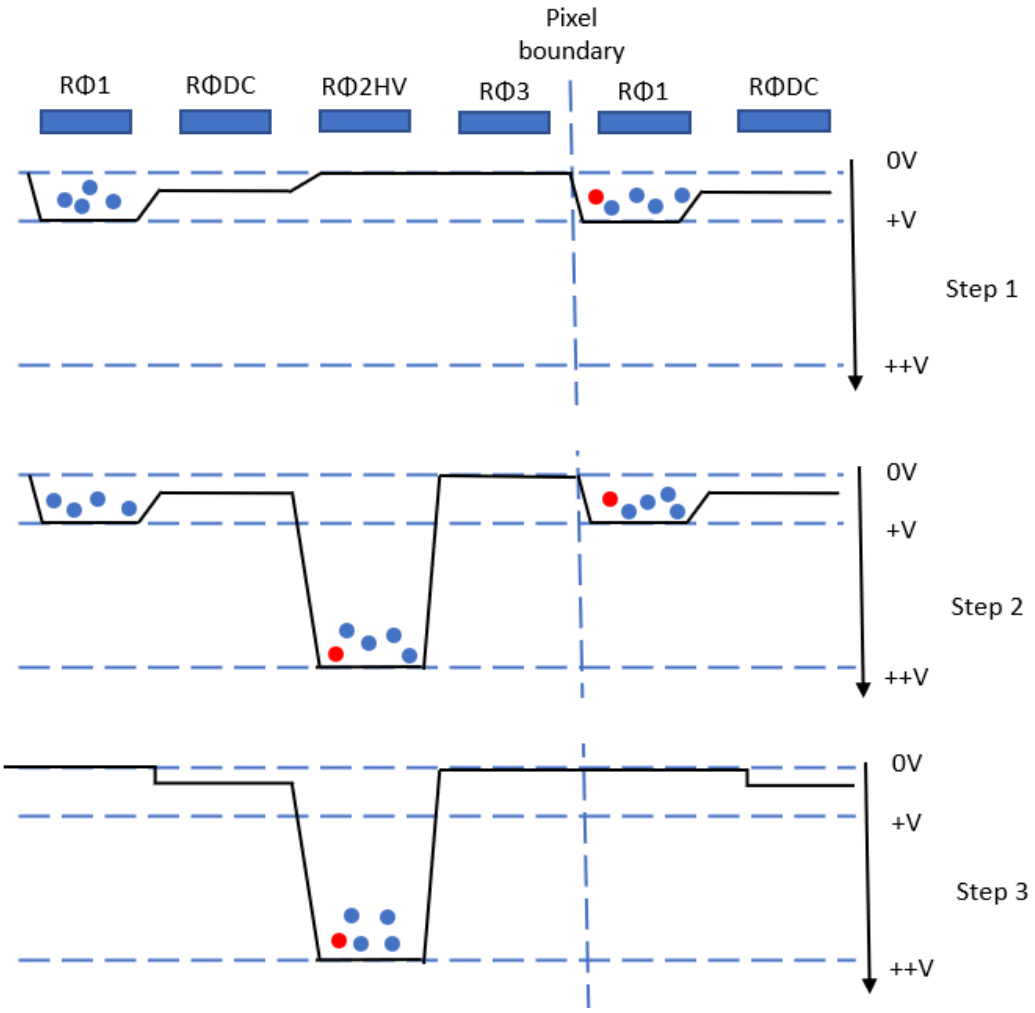

Figure 4-10: Sequence demonstrating the use of impact ionization to increase the number of electrons (blue dots) in the charge packet. The packet is held in RΦ1 while RΦ2HV is increased (step 2). RΦDC is kept at a low voltage allowing the electrons to flow into the deep RΦ2HV well. As electrons pass into this phase (step 3) there is a small chance they will excite another electron-hole pair, resulting in an additional electron than previously seen (symbolized by the red dot). This new electron may also produce new pairs in later cells within the multiplication register.

The chances of a new electron being generated in a single element is rather low (1-2%) which is why there are many multiplication elements. The average gain, G, that you would encounter across a device with N multiplication elements, each with a probability, p, of creating a new electron-hole pair is given by equation 4-8 (Jerram, et al. 2001)

$$G = (1 + p)^N \qquad 4\text{-}8$$

The probability is determined by the voltage levels of the clock as well as the device temperature. Assuming a worst-case scenario where p is equal to 1% and the device only has 100 elements, the gain is found to be 2.7 which could still prove beneficial in some situations. Generally, more elements are present and operating conditions are controlled to allow for a higher gain. If these changes allow a probability of 1.5% for each element and there are now 500 elements in the multiplication register a gain of around 1700 will be observed. This proves very advantageous when detecting small charge packets from low-energy photon interactions like soft X-rays.

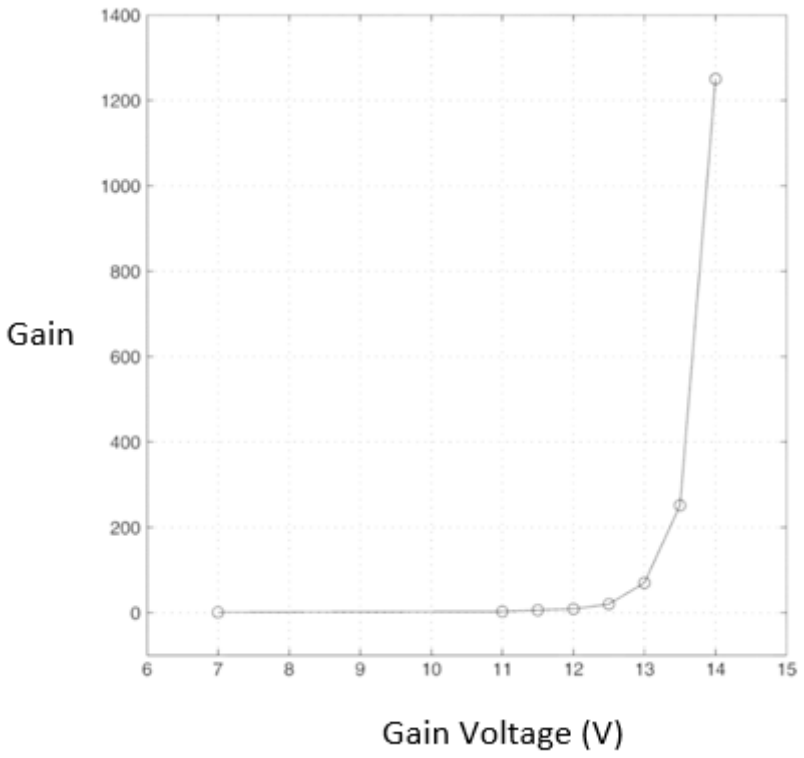

Figure 4-11: Plot of an EM-CCD's gain vs the high voltage used in the multiplication register when held at -40°C (Soesbe, et al. 2007)

4.6.2 Temperature dependence

The temperature of the device affects the probability greatly with lower temperatures allowing for higher gain values at a fixed RΦ2HV. This is due to reduced energy in the phonons meaning electrons are less likely to be scattered and more likely to use their energy to ionise more electrons. As the gain is so sensitive to the temperature of the device, it is important for stable gain during operation that the temperature is also stabilised.

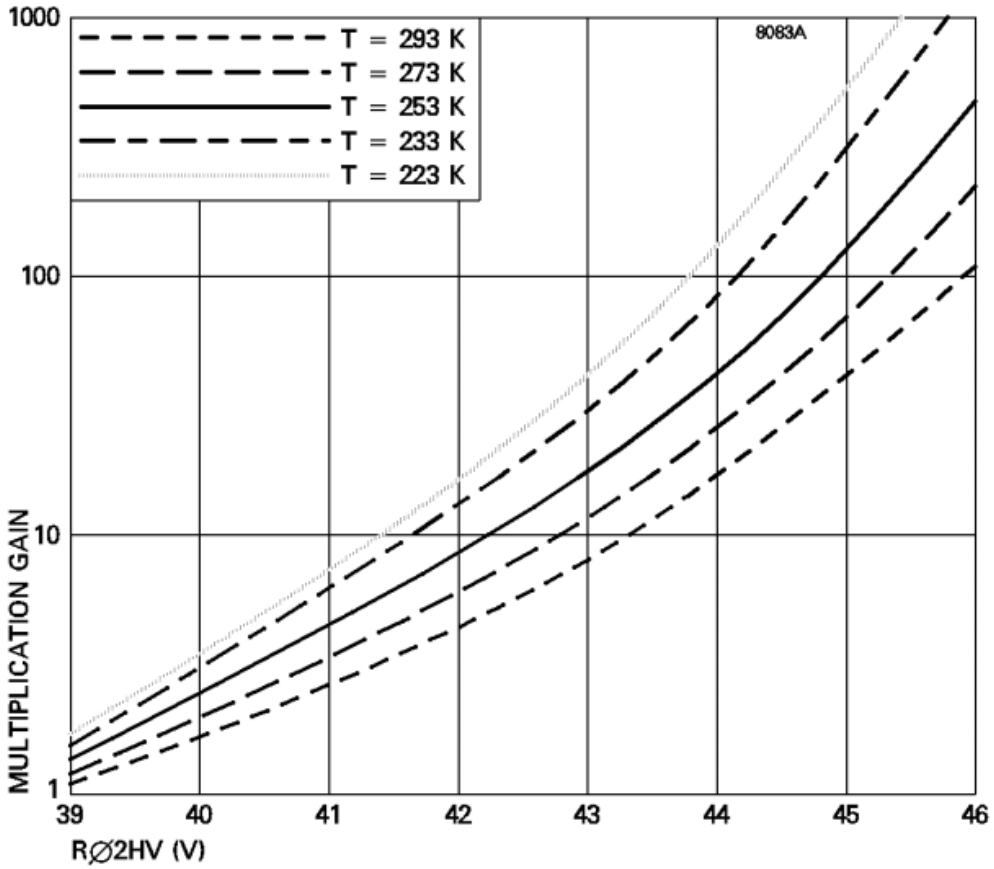

Figure 4-12: Typical variation in multiplication gain with varying high voltages in the multiplication register when a CCD97 is held at differing temperatures. (e2v technologies 2011)

4.6.3 Suppression of noise

The location of the multiplication register before the output node also proves advantageous. It has been established already in this report that the readout circuit adds some noise to the

voltage returned in the form of reset and readout noise. Looking at equation 4-3 shows the readout noise is independent of the signal. This is typically <100 e^- r.m.s. without CDS (e2v Technologies Ltd 2004, e2v Technologies Ltd 2015) and lower when CDS is in use (approximately 37 e^- r.m.s. for the CCD60 and CCD201-20). As the gain on the charge packet is so large in comparison to the added-on readout noise, the effective noise is suppressed, even for low energy charge packets.

4.6.4 Noise in an EM-CCD

Whilst the readout noise is heavily suppressed the other sources of noise inherent in CCDs are still present in the EM-CCD. Some degradation to the spectral resolution is observed due to the amplification of the signal packet in the gain register. The amplification is a stochastic process with a shot noise contributing to the final number of electrons generated equal to $\sqrt{n_e}$ for high gain levels. When combining this amplification noise with the Fano-limited shot noise in the number of electrons generated per X-ray event a combined noise of $\sqrt{fn_e + n_e}$ is measured at high gain levels. This can be re-written as $\sqrt{n_e}\sqrt{1+f}$ with the modified Fano factor being (1+f) (Tutt, Holland, et al. 2012).

For X-ray photons being detected on a device with high gain, the FWHM is found to be

$$FWHM = 2.3548\omega\sqrt{\left(\frac{\sigma_{readout}}{G}\right)^2 + G\sigma_{dark}^2 + \sigma_{shot}^2 + \sigma_{multiplication}^2} \quad 4\text{-}9$$

When a high gain is assumed both σ_{shot}^2 and $\sigma_{multiplication}^2$ are equal to $\frac{E}{\omega}$. This can also be written referring to the modified Fano factor.

$$FWHM = 2.3548\omega\sqrt{\left(\frac{\sigma_{readout}}{G}\right)^2 + G\sigma_{dark}^2 + 2\frac{E}{\omega}}$$

$$= 2.3548\omega\sqrt{\left(\frac{\sigma_{readout}}{G}\right)^2 + G\sigma_{dark}^2 + (1+\mathrm{f})n_e} \quad 4\text{-}10$$

If the device is cooled σ_{dark}^2 becomes negligible. If a high gain is also used, then the readout term also becomes negligible. This allows the signal to noise ratio to be found using:

$$\frac{S}{N} = \frac{n_e}{\sigma_{total}} = \frac{\sqrt{n_e}}{\sqrt{1+f}} \qquad 4\text{-}11$$

If the gain is not large enough (<10x) it has been observed that the noise due to the gain amplification does not follow a Gaussian approximation. If a gain of 1 is used, i.e. a standard CCD behaviour, the multiplication gain is zero however Gaussian approximations would not work for this. The Excess Noise Factor (ENF) is a measure of the ratio between input and output signal variances of the gain register in the optical case when a low gain is used. This value starts at 1 for a gain of 1 and tends towards a value of 2 for gains larger than 10 (Robbins and Hadwen 2003). The ENF allows the total noise at low gain to be predicted using equation 4-12.

$$FWHM = 2.3548\omega \sqrt{\left(\frac{\sigma_{readout}}{G}\right)^2 + ENF\sigma_{dark}^2 + ENF\sigma_{shot}^2} \qquad 4\text{-}12$$

4.6.5 Changes over the EM-CCD lifetime

Over the lifetime of an EM-CCDs operation the amount of gain acquired from a set voltage decreases. The same gain can still be obtained using shifting to a higher voltage (Figure 4-13) but if longer missions and observation times are required of the device the ageing of the gain needs to be understood.

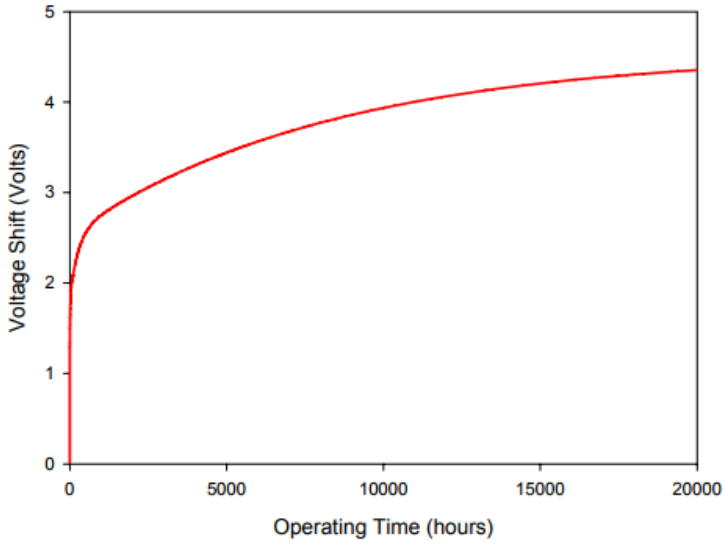

Figure 4-13: Observed ageing of a CCD65 running at an 11 MHz pixel rate with a gain of 1000 and uniform signal of 300 ke^- (e2v technologies 2006).

The largest drop in gain occurs during the first hours of operation so it is common practice for the manufacturer to 'break-in' the devices in to ensure the gains do not drastically change when the consumer first uses the devices. The degradation of the gain is then observed to be quite slow (Evagora, et al. 2012). It is believed that the ageing occurs due to electrons being accelerated rapidly towards the silicon oxide layer and possess enough kinetic energy to embed themselves permanently within it. This reduces the resultant electric potential when a bias is applied to the electrode and so the avalanche gain is decreased (Ingley, Smith and Holland 2009).

4.7 Summary

CCDs have a good history in the areas of observational astronomy and so further advancing this technology in a manner to allow for low level observations such as soft X-rays is of vital importance for future missions. The precision that is required with the observations coupled with the sensitivity of these devices means there is a lot of characterising and optimising that must be carried out with any detectors chosen for use in each project.

The work in this thesis looks at how EM-CCDs can observe X-rays with the presence of unwanted signals in the same image as well as how this noise can be found and reduced. As discussed, EM-CCDs are capable of supressing readout noise however the temperature dependence and variability of gain in the system needs to be highly characterised if a constant performance is desired in conditions which may change. This knowledge could then allow for a greater degree of control in the device's operation should this occur which is beneficial for devices whose spectral performance is so finely linked to its operating conditions.

Whilst CCDs are available in many configurations (different image areas, pixel sizes, etc), EM-CCDs are not as prevalent or as requested. It is possible that projects such as OGRE are therefore capable of showing the benefits of these devices in low signal observations and thus improving the demand for these devices, increasing the variation in the market to suit the needs of different areas.

5 Simulating the OGRE mission & the updated design

Whilst the success criteria documents created for the OGRE teams gave a good outline of the minimum science we were hoping to achieve, an exact simulation of the OGRE payload had not actually been created to check the spectral line counts. With the OU and XCAM team working on the detection of the photons as well as the event detection algorithms it seemed it would be useful to determine how the results could approximately look to ensure the system could observe an accurate and worthwhile spectrum.

It was therefore decided that a simulation should be created modelling each of the key components using relevant physics and the constraints assigned from designs to the setup. As this piece of work was more to develop an understanding of the entire system and to provide peace of mind about the capabilities of the project the original model was developed to be ideal, i.e. assumptions made to allow for the maximum theoretical output, with additions to be made later to consider the errors that would likely be present in the actual construction. Any assumptions made for each component will be stated.

The paper Lewis, et al., 2017 includes the first description of the work contained in this chapter however this thesis will detail the mathematics and method behind the results as well as delving deeper into the effects of the simulation on the mission.

5.1 Simulating Capella

5.1.1 Method

To determine the possible spectrum, we could expect to observe with the OGRE camera an input spectrum was required to allow for the efficiency of each OGRE component at different energy ranges to be used. Capella has been observed by previous missions, the most notable data catalogue coming from observations by Chandra from 1999 to 2006.

The Chandra Capella data set was kindly provided by David Lumb (Lumb 2017) along with the constraints of the instrument used to acquire the data.

The data provided an X-ray count at different wavelengths over an 84597 s observation. To use this data for the OGRE simulation it was required to convert this data into a flux from Capella, the incoming light per second per area, rather than the observed count. Luckily, the effective area data for Chandra was also provided for each wavelength bin in the data. This value considers the gathering area of the telescope and reduces its value by the ratio of the amount of light at that energy which would successfully make it through the system (i.e. a telescope of spatial area 2 m^2 with an overall efficiency of 0.75 would have an effective area of 1.5 m^2). This allowed for the conversion of the X-ray count in the system to the total number of X-rays per unit area predicted to have been incident with Chandra. The wavelength could then be converted to an energy by using the Planck and wave equations (equation 5-1).

$$E = \frac{hc}{\lambda} \qquad 5\text{-}1$$

5.1.2 Findings

Taking the 84597 s observation time into account allows for the flux to be found and thus an input spectrum for the OGRE simulation generated (Figure 5-1). For the case of an ideal simulation it was assumed the flux of Capella is the same for both Chandra and OGRE despite there being differences in the observation environment (e.g. height at which the observation occurs, true distance from the source to the instrument etc.).

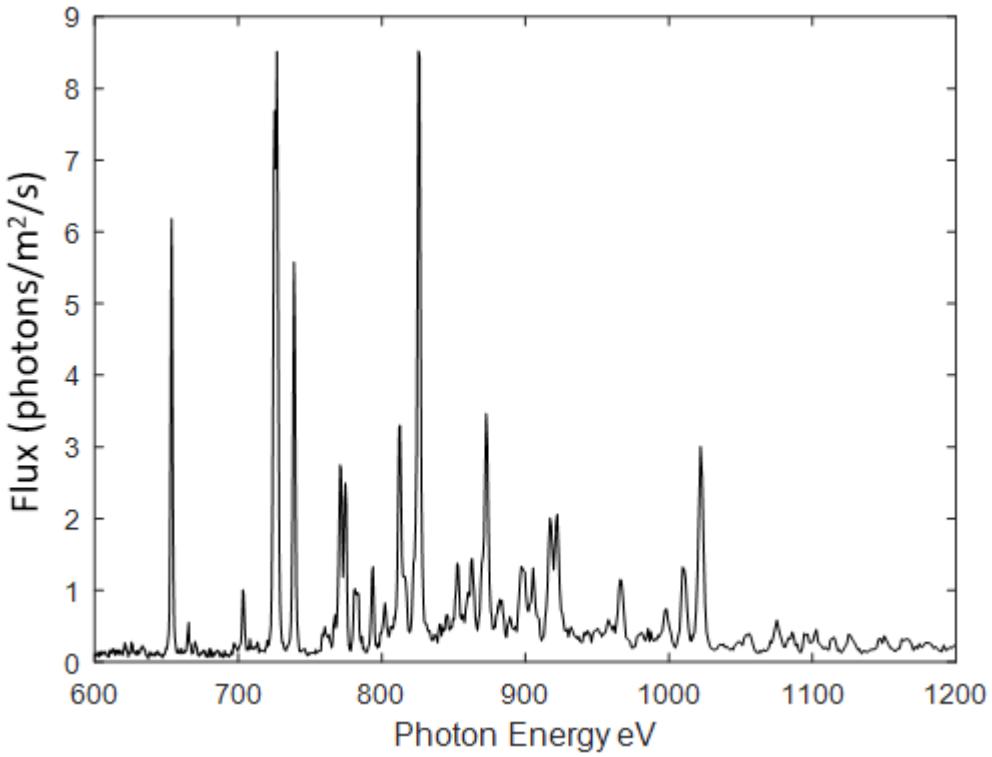

Figure 5-1: The Capella spectrum across the OGRE energy range as observed by Chandra. Seen previously as Figure 3-1

5.2 The OGRE optics module

The OGRE optics is a Wolter-1 system comprised of a parabolic mirror and a hyperbolic mirror. These mirrors are nested to increase the overall collecting area as a shallow angle I needed to successfully reflect X-rays. Each of these mirrors is constructed from silicon which gives a low mass and high reflectivity for X-rays. One of the assumptions for the ideal system is that the mirrors are perfectly aligned so that any light incident on the parabolic mirror is successfully directed to a point on the hyperbolic mirror which reflects it towards the gratings. Therefore, the observational area of the module is that of the exposed cross section of the nested parabolic mirrors.

The OGRE design consists of three optics modules each with 8 nested mirror layers covering a 60° azimuth. A physical test module had been constructed by NASA's Goddard

Flight facility to check for the structural integrity of the system and had been built according to the design of the OGRE system. From the central point of the optic (i.e. the centre of the circle) the position of the mirror edges was known to an accuracy of hundredths of a mm. The total area coverage was calculated considering only the exposed faces of the mirrors (mirror edges are not included in the calculations and it is assumed any photons incident there are scattered in a non-disruptive way). The innermost radius of the parabolic mirrors has a radius of 165.03 mm and an outermost radius of 180.94 mm. Using simple maths and the values of the mirror edges provided gives a total optical area of 0.0129 m^2.

The reflectivity of the mirror is dependent on the angle of incidence, the energy of the incident photon and the material composition of the mirror. Whilst many mirrors used in observation would have a coating applied to improve the structural rigidity and fine tune the mirror to perform better at the desired energy values it was assumed the mirrors would be uncoated as plain silicon has a better reflective index with the OGRE constraints than many of the traditional mirror coatings. Using the design's graze angle of 1° and entering the values into a reflectivity calculator (B.L. Henke 1993) produces reflectivity data for the OGRE mirrors in desired X-ray energy range at the relevant graze angle as seen in Figure 5-2. The variation over the energy range is only small and the reflectivity value is

generally high, so the composition of the mirror is a good match for the design of the system.

With the assumption being that the optical area is that of the parabolic mirror system and that the X-rays are reflected off two mirrors (angle is kept constant despite it varying in reality) the effective are of the optics module is therefore

$$A_{Effective} = A_{Actual} \times R(E)^2_{Silicon} \qquad 5\text{-}2$$

where $R(E)_{silicon}$ is the reflectivity of silicon for a photon of energy E. For comparison with another system, the effective area of the OGRE optics with 1000 eV photons is 0.01019 m^2 whilst Chandra has an effective area at the same energy of 0.04 m^2. This is largely due to Chandra being a considerably larger telescope though.

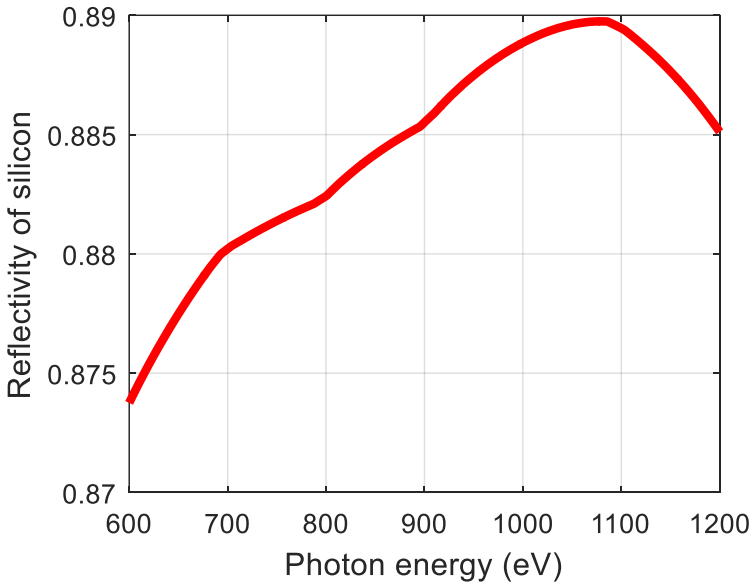

Figure 5-2: The reflectivity of silicon over the OGRE soft X-ray energy range when a graze angle of 1°is used.

5.3 The off-plane gratings efficiency

The main goal of the OGRE project is to observe the Capella spectrum with the secondary goals being to increase the Technology Readiness Level (TRL) of the three main

components. Whilst diffraction gratings have been used in previous missions to good effect it is hoped that the new arrangement used in OGRE has a significant advantage over these previous systems which will be adopted into future missions once a higher TRL is achieved. Generally, a large amount of science in previous setups is lost at the gratings stage due to the scattering nature of the component and its design.

The off-plane arrangement in the OGRE mission should allow for greater resolving power at higher orders as well as a reduction is shadowing due to each grating being fully illuminated. The blazed profile preferentially dispersing to one side of the zero order should also greatly increase the count when a given detection area I used. With many variables being available to be fine-tuned the gratings have a high customisability when it comes to ensuring they fit well into a mission's design.

The off-plane gratings to be used in the OGRE system are made from fused silica with a gold coating. The gratings will be used in a Littrow configuration, a geometric arrangement which allows the diffraction and incidence angles to be identical. Each grating features a groove density of 6250 grooves/mm and light will be incident at an angle of 1.5°. A preferential dispersion towards certain orders should allow for a greater number of X-rays to be observed and so the gratings are mounted with a yaw of 0.85°.

The Penn State University team ran some tests with gratings using these parameters with the data being used to generate an efficiency curve for the gratings over the OGRE X-ray energy range (Figure 5-3).

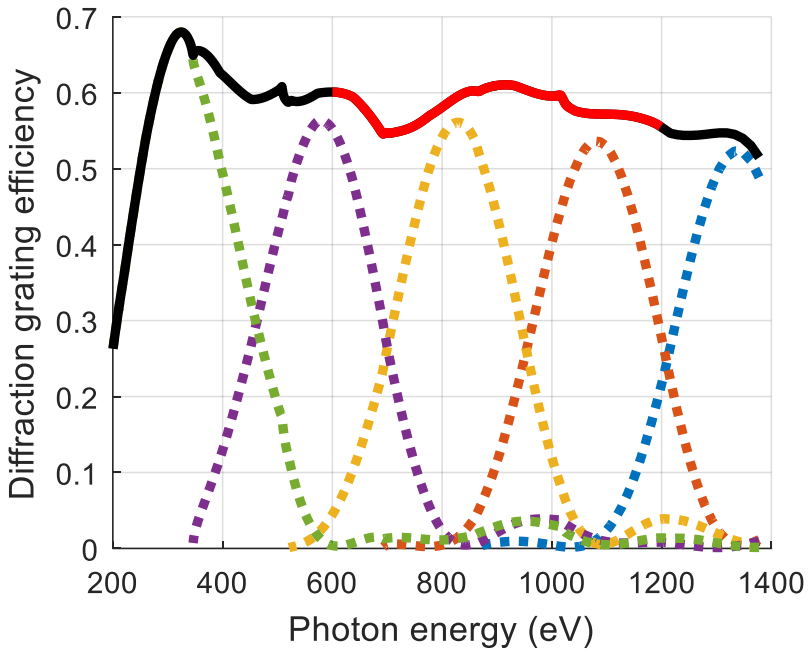

Figure 5-3: The total grating efficiency over a broad energy range (black line) which covers the OGRE energy range (red line). This is the sum of the individual order efficiencies (greens dashed is first order, purple is second order, yellow is third order, orange is fourth order and blue is fifth order).

The data shows the diffraction efficiency of the off-plane gratings is around 0.575 which may seem low however previous grating systems were observed to have efficiencies around 0.4 at the highest so this technology is a noticeable improvement on previous systems that have been used.

The simulation assumes the angles of approach for all X-rays is the same, i.e. a parallel beam, and that this data set is an accurate portrayal of how X-rays would be diffracted in the final payload. The assumption regarding the optics also mean it is assumed any X-rays successfully reflected by the optics are incident on the gratings which are the diffracted towards a detector.

5.4 Optical Blocking filters

The design of the OGRE payload means some optical light is likely to be incident upon the detectors. As this light would interact with the devices in a manner which would interfere with our X-ray observations an optical blocking filter is likely to be needed. Upon the creation of the simulation an optical filter had not been decided upon for the OGRE mission. To simulate with representative values for a space grade optical filter, the properties of the filter used for the CLASS instrument were taken as a borderline (Smith 2016). This filter should allow for good X-ray transmission as well as blocking practically all optical and ultraviolet light. The suggested filter is comprised of 0.4 µm of polyimide and 0.2 µm of aluminium.

The expected transmission values were determined using an available data catalogue to cover the OGRE energy range (Figure 5-4). Whilst the generated figure suggests the polyimide is a detriment to the filter and significantly reduces its low energy X-ray transmission it should be noted that it is of great benefit at blocking the ultraviolet components and helps provide structural integrity to the system. The overall transmission at this lower end is still a region which could be improved upon; however, an optical blocking filter is relatively simple to add to the OGRE design and so a more concrete decision on the filter to be used will occur later.

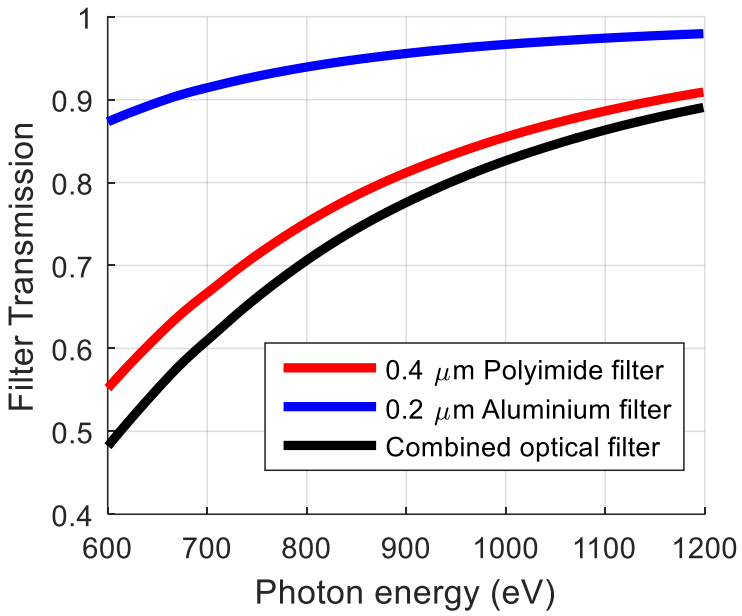

Figure 5-4: Transmission factors for a polyimide filter, aluminium filter and the suggested optical blocking filter comprised of both layers.

5.5 Assumptions of the simulation

The detectors are only capable of observing photons which are incident upon them. To determine if the X-rays successfully reflect off the mirrors, are incident upon the gratings and diffract in a direction which will cause it to be incident upon one of the three EM-CCDS a ray-tracing code would be needed. As this simulation was to improve the overall understanding of the system as well as to get a good idea of the instruments maximum capabilities it was deemed that ray-tracing would be a detriment due to the amount of time which would be needed to learn how to do add it to a simulation. The largest assumption made in the simulation is therefore that all X-rays which successfully pass through the optical module, gratings and optical blocking filter are incident on the detectors imaging area regardless of the size of the detectors used. This means the effective area used in this model is the maximum value theoretically possible if a perfect

system was created, therefore a real setup will have a diminished value due to even the smallest of inaccuracies.

5.6 The Quantum Efficiency of EM-CCDs

Even with the assumptions regarding the travelled path taken by the photons this does not mean the X-ray is observed as the quantum efficiency (QE) of the device needs to be considered. This is a measure of the probability that an incident photon is detected. QE data for the CCD207-40 over the OGRE energy range is not readily available however colleagues within the CEI had carried out an experimental run on the CCD97 which covered the OGRE energy range (Moody n.d.). As this detector has a thickness and back surface passivation incredibly similar to that of the CCD207-40 it was deemed that this data would be a good fit for simulating the OGRE detector performance (Figure 5-5). As the data is still sparse over the energy range a fitted line for which QE values could be obtained for any given energy gives some QE values greater than 1. As this is a scientific impossibility (equating to a chance 1 event could cause multiple correct detections) a condition was added to ensure the QE never exceeds a value of 1.

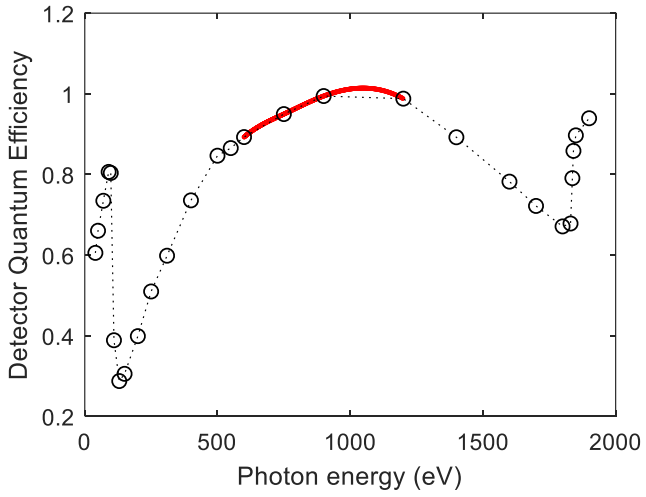

Figure 5-5: The QE data of the CCD97 (black dotted line with data markers) with a fitted spline for the OGRE energy range (red line)

5.7 Total effective area (EA)

The Capella spectrum obtained from the Chandra data provides the total number of photons expected at each energy level per square metre per second. It is therefore important to see what the overall area is per energy bin for the OGRE system. This could then be used along with the observation time to predict the total counts within each energy that the OGRE system would observe. Multiplying the OGRE optics effective area shown in section 5.2 with the grating efficiency, optical blocking filter transmission value and QE value gives the total effective area of the ideal OGRE system (Figure 5-6). Comparing this to the effective area of Chandra shows that the instruments within the OGRE camera demonstrate a vast improvement over previous technologies, especially when the fact the optical effective area of OGRE is a little over one quarter of Chandra's.

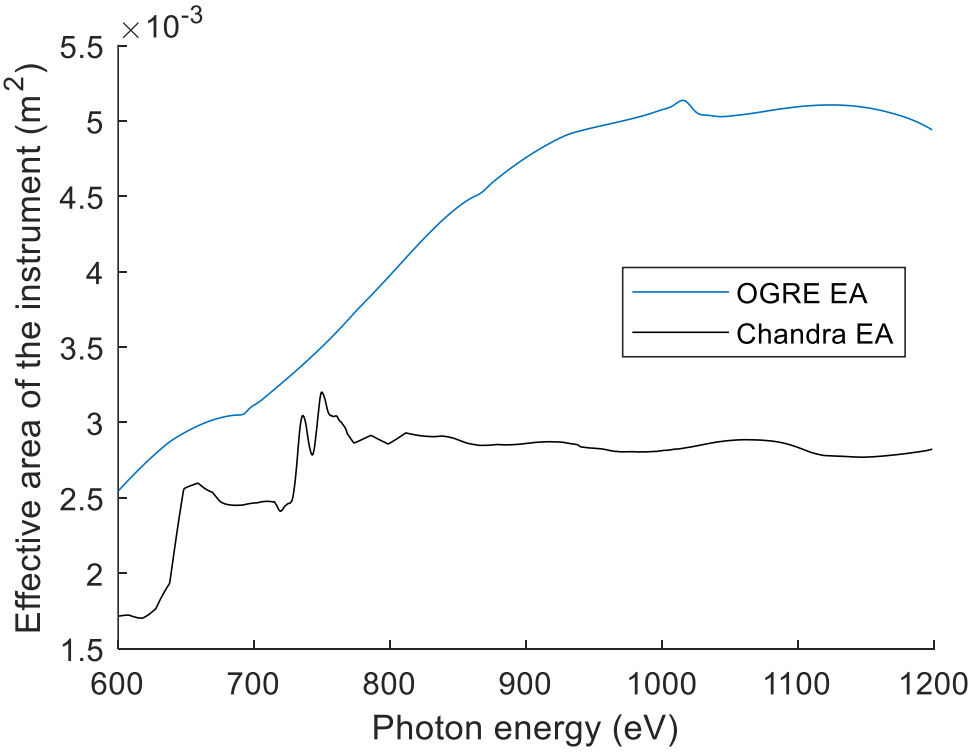

Figure 5-6: The total effective area of the OGRE system over the OGRE energy range compared to that of Chandra.

This plot is therefore a testament to the potential of the off-plane gratings and EM-CCDs for soft X-ray observations as these two components alone can significantly improve the detection of X-rays if used in a proper configuration.

5.8 Resultant spectrum

Combining the effective area of the OGRE payload with the flux predicted from Chandra's Capella spectrum allowed for the creation of the OGRE spectrum (Figure 5-7). Rather than finding a total photon count for each energy bin the detected photons per second were calculated to allow for an estimate about the required observation time for certain peaks.

For this section, a photon peak refers to the value in one energy bin and a spectral line refers to the sum of the counts of an energy bin and its neighbours.

The OGRE system will get somewhere between 3 and 6 minutes of observation time. To be considered a success the OGRE camera must be able to observe at least one spectral line consisting of at least 25 photons. Looking at the simulated spectrum the most likely line this would occur is the Fe-XVII line at 825 eV (estimated 0.096 photons s^{-1}). To meet the minimum success conditions at this line a minimum observation time of 4 minutes and 20 seconds would be needed. Whilst the 6-minute observation time would allow for the peak to be observed to a degree acceptable for the success criteria, if the shorter observation times occurred the mission would fail.

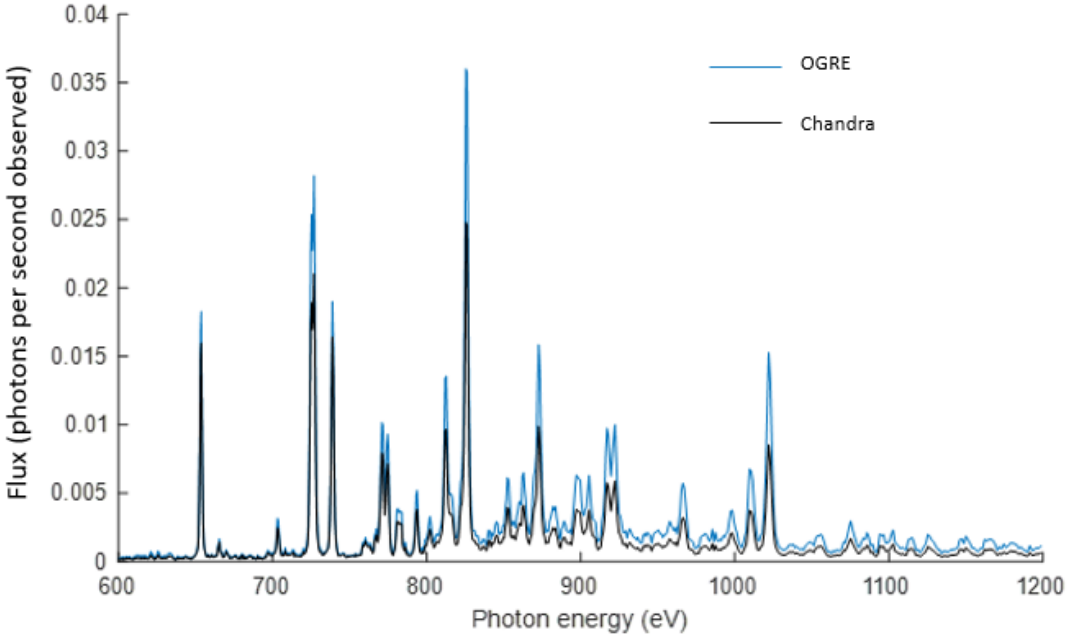

Figure 5-7: Simulated photon count rate of OGRE (blue line) over the OGRE energy range compared to the photon count rate of Chandra (black line).

5.9 Proposed design changes

Considering that this is also an ideal model, i.e. the photon count per second will only decrease as the simulation is improved upon, the fact a failure seemed likely was of great concern. Looking over the contributions from each of the main components showed that there was little to be improved upon concerning the QE of the detectors and the reflectivity of the mirrors. This meant the areas which could be improved upon were the gratings, the optical blocking filter, and the optical module. Whilst the blocking filter does prove to be a big detriment to the photon count at the lower energy end of the X-ray spectrum the benefits it provides by blocking the visible and ultraviolet photons means it is a necessary object. Other commonly used X-ray filters were looked at for insertion into the simulation however for the OGRE energy range the polyimide/ aluminium filter seemed the most suitable for the mission's aims. The grating efficiency also reduces the count greatly

however compared to previous gratings used in missions the off-plane gratings showed a large performance improvement.

It was therefore decided to focus on how changing the optical module could improve the photon count. Increasing the collecting area would naturally increase the total number of photons entering the system. Editing the variables in the simulation and extrapolating the mirror spacing to add additional mirror layers to each module showed that if 12 mirrors were present in each module instead of 8, the optical area would be 0.0202 m^2 and the effective area would increase (Figure 5-8) causing the spectrums Fe-XVII line to consist of 0.149 photons (Figure 5-9). This would require 168 s of observation to reach the 25 photons needed in a single spectral line to classify the mission as a success. This is the fewest number of mirrors required to ensure a success if the observation time OGRE got was only 3 minutes.

At the time of the simulations creation the prototype optical module containing 8 mirrors had not yet been checked for its structural rigidity to see if it could withstand a rocket launch so suggesting the use of twelve mirrors while ideal was not a known possibility.

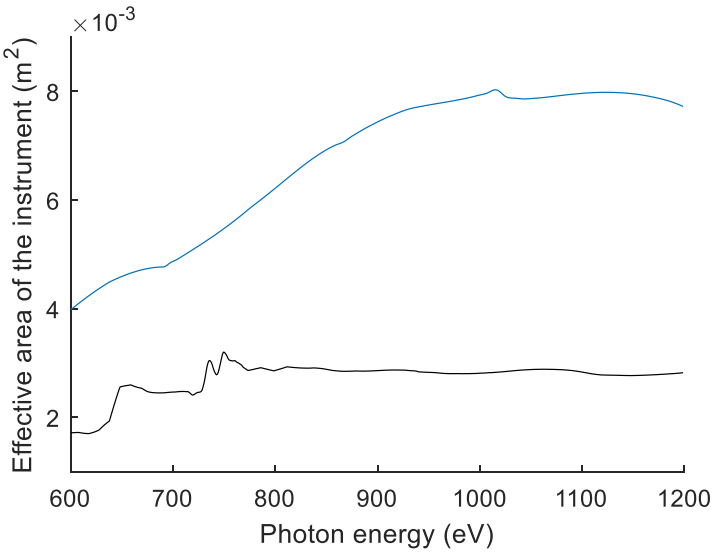

Figure 5-8: The effective area of the OGRE system with a 12-mirror optical module (blue) compared to the Chandra effective area (black) over the OGRE energy range.

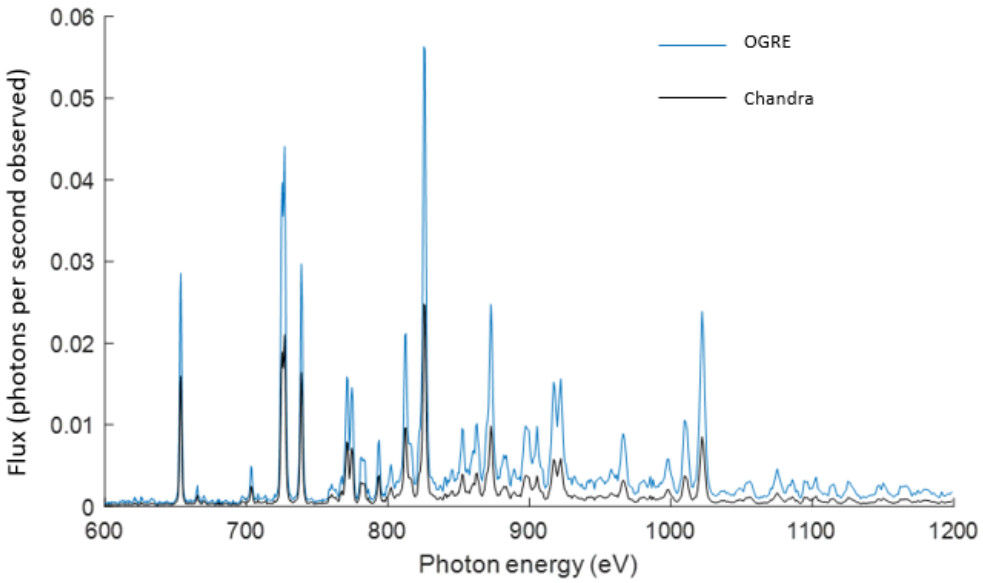

Figure 5-9: The 12 mirror OGRE simulated photon count rate (blue) compared to the Chandra spectrum (black).

It should also be noted that the OGRE energy bins will be narrower than those seen in these figures. As the spectrum data cannot be generated for the resolutions OGRE will be hoping to observe at ($\lambda/\Delta\lambda = 2000$) the final spectrum will hopefully show more split peaks and narrower lines.

5.10 Impact on the OGRE mission

The findings of the 8-mirror simulation came as a surprise to the OGRE team. The optical module and gratings teams (Goddard and Penn State University respectively) held a discussion to see what could be changed to ensure that the final OGRE flight successfully observed the spectrum we were hoping for. An appeal for additional funding was successful allowing for the Goddard and Penn State University teams to put together a new design which would hopefully impact the camera operation and mission timescale as possible.

5.10.1 The meta-shell optical telescope

It was apparent that the total collecting area would need to be increased to allow for a higher count rate in the OGRE system. It was noted that 12 mirror layers could allow for an adequate count rate and testing on the 8-mirror module had been successful. The team at Goddard had been working on a new optical design known as meta-shells which had also passed structural rigidity testing. This design utilises layered mirrors stacked with an overlap (like the layout of bricks in buildings) with each mirror being mounted at four points help minimise distortions to the mirror (Figure 5-10).

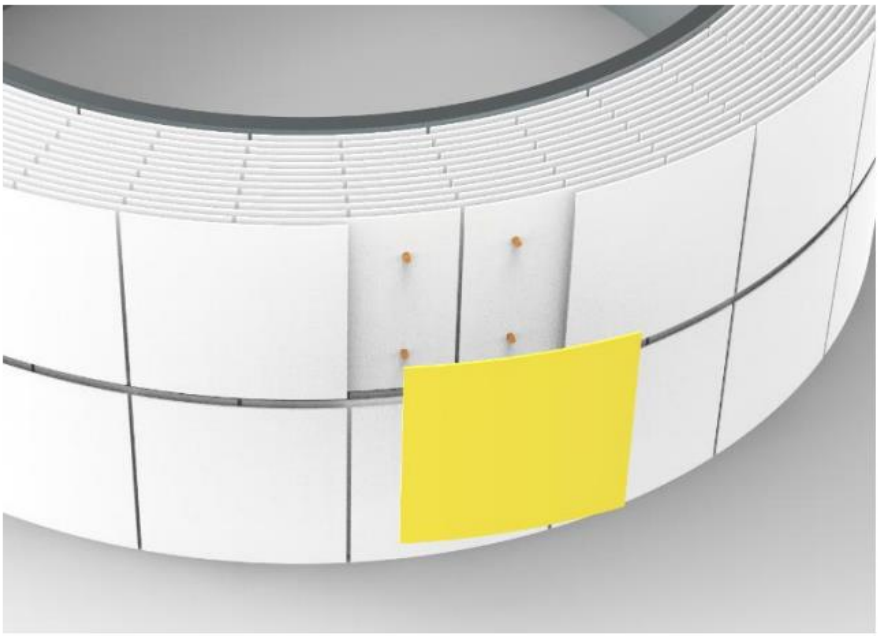

Figure 5-10: Construction and mounting of the meta-shell optical system (McClelland 2016).

This new technique has a lower tooling cost and offers a more precisely defined optical axis. OGRE will be the first use of this new arrangement with silicon mirrors (McClelland, Bonafede, Saha, Solly, & Zhang, 2016). Instead of having three modules each covering 60° the new OGRE optic is one meta-shell consisting of 12 mirror layers and covering a full 360° azimuth. This new design therefore has an area approximately 0.04 m^2 rivalling that of Chandra within a considerably smaller radius.

5.10.2 The new grating arrangement

With the increased optical coverage an increase in the number of grating modules was also needed. Covering a full 360° optic with gratings and still being able to produce viable arcs of diffraction onto three rather small detectors was quite a challenge, however a new design was developed to ensure a large coverage area and clear arcs.

Figure 5-11: CAD of the optical module assembly with the grating modules mounted onto a 'spider' structure (J. H. Tutt 2018)

The new gratings design (Figure 5-11) utilises 12 grating modules in 6 different arrangements (groups of 2).

5.10.3 Changes needed regarding the camera

Due to the updates of the optical and grating system corrections will need to be made regarding the positions of the EM-CCDs used in the camera as well as possible changes to the readout methods previously discussed as viable options. The newer design features 6 different arcs of diffraction due to the increased number of grating modules, however the camera system still consists of three detectors. As this number could not be increased further a new system was devised allowing an overlap of two arcs over one device (Tutt, McEntaffer, et al. 2018). By having an opposing grating profile with an alternative mounting angle, two gratings modules can disperse onto the same detector (Figure 5-12).

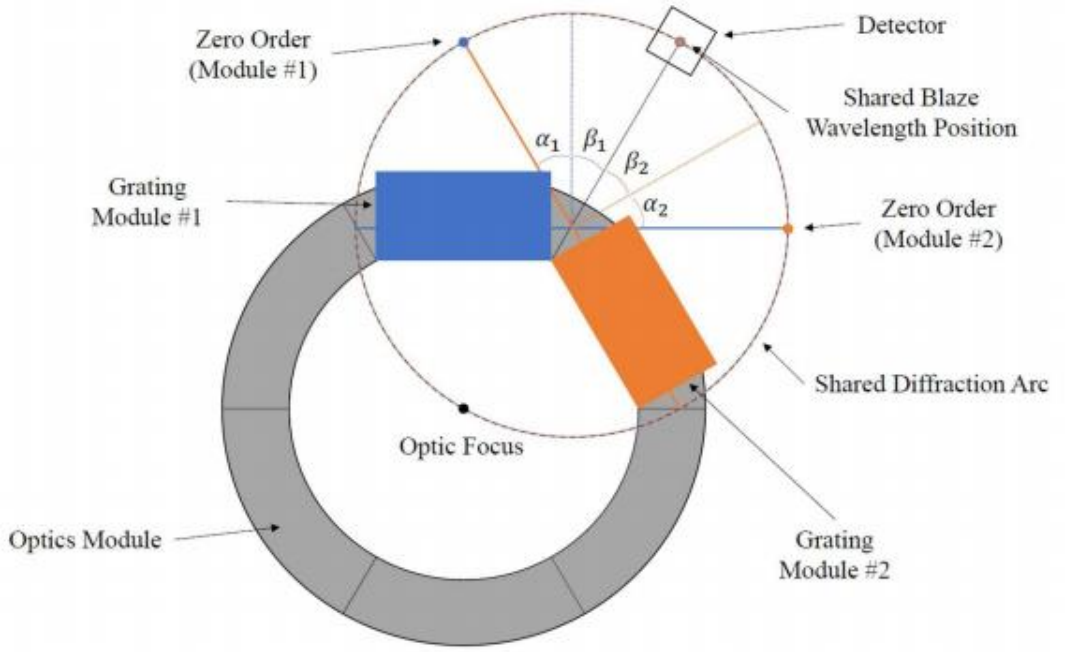

Figure 5-12: Schematic demonstrating how two gratings modules can have a shared overlap onto one detector (Tutt, McEntaffer, et al. 2018)

Repeating this three times for the entire optics and gratings system therefore gives a camera layout with the exact specification being dependent on the final grazing angles and positions (Figure 5-13).

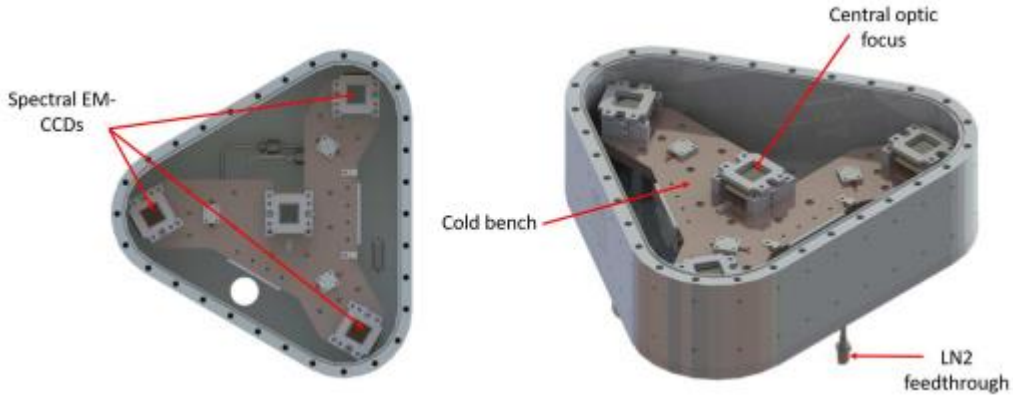

Figure 5-13: The updated camera system design with a cold bench allowing for the cooling of all four detectors. The exact positions could vary however this is the general form the system will take from this point onwards.

With this design a fully populated set of diffraction arcs would give a cross-shape on the three spectral EM-CCDs. This overlap may allow for windowing to be used to reduce the detector area read out, however this will depend on the variation of the X-ray positions on the device as tolerances need to be built in. It is also important that the exact arc the observed X-ray is from is known due to the mission utilising event positions to infer the X-ray energy rather than the value of the observed signal (unsuitable for use due to the electron multiplication).

The new system must therefore perform a check to ensure that the X-ray origin can be accurately determined. If an exact mirrored system of gratings is used, the overlap region will be difficult to check due to a region in the centre of the device where X-rays of similar energy will fall within proximity, especially when the potential variation in X-ray position is considered. By offsetting the gratings slightly, the overlap position can be adjusted so this overlap region consists of lower energy X-rays from one arc, and higher energy X-rays from the other. This would allow a check on the observed signal to infer which of the gratings the X-rays came from in his overlap region whilst allowing very clear character characterisations elsewhere on the device due to a greater separation (Figure 5-14).

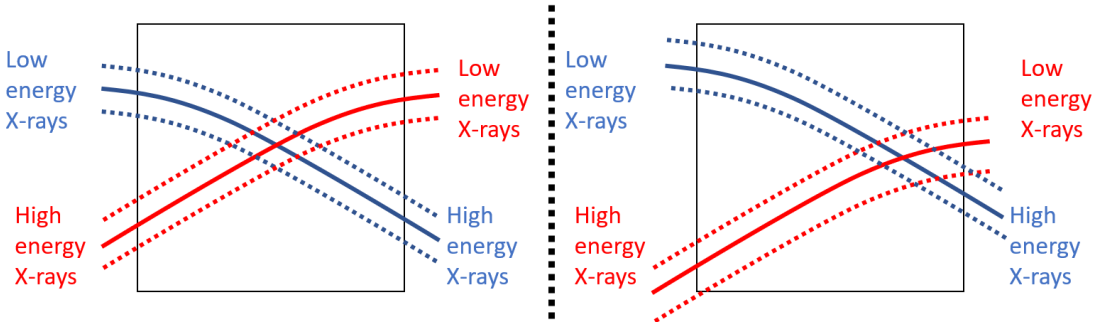

Figure 5-14: Overlaps of two arcs of diffraction on a single device. The left shows a mirrored grating setup with the device on this line of symmetry creating a clustered overlap region in the centre of similar energies. The system on the right is possible with an offset of one grating allowing an energy difference in the overlap region allowing for some differentiation between X-rays sources.

Whilst the exact nature of the camera system can only be determined upon a confirmed design and specification of the optical and grating systems, it is still essential to check how the EM-CCDs perform when detecting X-rays in a vacuum as well as testing a prototype camera system to check its suitability for use in the final payload.

5.11 Summary

The overall OGRE system was modelled based on the theoretical/ ideal capabilities of each of the projects key components with an input data stream created by utilising real data from a previous observation combined with the instruments known effectiveness to generate a pre-observation X-ray spectrum of the Capella system. The aim of the model was to initially improve the understanding of the project however it has had connotations which affected the mission greatly.

Whilst the input spectrum of Capella generated from the Chandra data does not match the spectral resolution OGRE is intending to meet, it was the overall flux of photons in the OGRE target waveband which was of significance. Each of the components was shown to be highly effective when working with the soft X-rays of the desired energies however the overall flux into the system was seen to be the greatest limiting factor.

As this is a limited time observation due to the nature of sounding rocket missions the simple option of increasing the observation time, a benefit Chandra had due to tis satellite nature, the decision to increase the optical collecting area was taken with an understanding of how much this would affect the overall requirements elsewhere in the payload. The increased number of diffraction gratings particularly added a large amount of increased complexity to the making of the OGRE telescope which in turn affected the focal plane and thus the camera system to a significant degree. With the flight detectors being a fixed dimension and of a known capability, the changes to the operation of the camera system are relatively minor, however the layout of the devices and the requirements of the

image analysis is something which will be adjusted once the exact alignments and capabilities of the optical and gratings modules are known.

The updated design capabilities will therefore greatly improve upon that seen with the initial design, which in turn was also noted to benefit from considerably better performance than the Chandra satellite. Upscaling this design to further increase the optical collecting area whilst maintaining gratings and detector areas appropriately for a large-scale mission would allow for significantly better performance than any currently seen X-ray satellite.

6 Experimental setup and the OGRE prototype camera

6.1 The prototype camera

The OGRE camera was designed and built by XCAM Ltd to specifications given by the Penn State University team. The project required a camera system which could achieve a 1 Hz readout whilst offering on-board event processing, temperature control capabilities, and the transferral of resultant data to a simple output to be used by a telemetry system. This system would also need to allow for the use of 4 EM-CCDs so power management and simultaneous device operation would need to be well maintained.

A design was created which could accomplish these requirements however it resulted on some technology new to the company. It was therefore decided that a prototype version of the camera system should be constructed and tested to ensure the flight model works as intended.

6.1.1 The laboratory EM-CCDs

The detectors chosen for OGRE are the CCD207-40 produced by Teledyne e2v-technologies Ltd (Figure 6-1 & Figure 6-2). These EM-CCDs feature an image section comprised of 1600 × 1600 pixels each of which is 16 µm squared. There are two available readout paths built into each detector, one leading to the Large-Signal (LS) output, and another leading to the High-Responsivity output (HR). The multiplication register is located before the LS output node. These devices are back-illuminated to allow for a greater sensitivity with the low-energy photon detection.

It is of paramount importance that the actual flight detectors remain as clean and undamaged. Testing with these devices would therefore impact their capabilities and so an alternative device was needed.

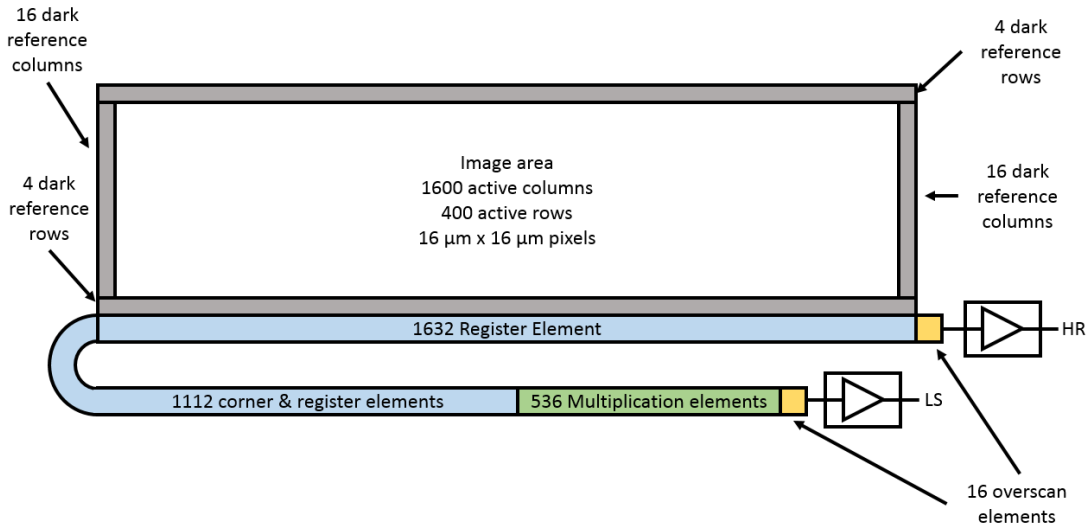

Figure 6-1: Schematic of the CCD207-10 adapted from the Teledyne e2v CCD207-00 & CCD207-10 Back-Illuminated data sheet. Whilst the HR node is present all operations of this device throughout the thesis are done via the LS output.

The prototype OGRE camera is instead fitted with four CCD207-10s, also produced by Teledyne e2v-technologies. These devices are a suitable alternative as they use the same electrical structure but feature an image section comprised of 1600 x 400 16 µm square pixels: effectively one quarter of the final flight devices. The devices used in the lab are engineering grade 5 devices kindly donated by Teledyne e2v for use with the prototype OGRE camera system. Whilst these are functional, they are not quite to the desired specifications as the final devices will be in terms of sensitivity or noise levels.

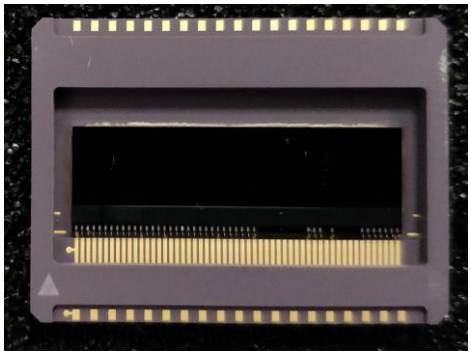

Figure 6-2: The CCD207-10 in its packaging

6.1.2 Comparing the laboratory detectors and flight detectors

Without having any of the CCD207-40 detectors to test with the prototype camera it is important to ensure the device specifications match up so that the installation and operation of the flight models will go smoothly. This comparison can be seen in Table 6-1. As can be seen the difference between these devices is that there are fewer rows in the CCD207-10 but all other device properties are the same.

Table 6-1: Comparison of the CCD207-10 and CCD207-40. Data taken from the relevant Teledyne e2v data sheets

Parameter	**CCD207-40**	**CCD207-10**
Active Image area	26.11 mm x 25.73 mm	26.11 mm x 6.53 mm
Image section active pixels	1632 (H) x 1608 (V)	1632 (H) x 408 (V)
Image pixel size	16 x 16 μm	16 x 16 μm
Additional over-scan rows	4	4
Additional dark reference columns	16 + 16	16 + 16
Total elements per line	1648	1648
Multiplication elements	536	536
LS path corner and register elements	1112	1112

6.2 The experimental chamber

The OGRE prototype testing chamber was put together to allow for the testing of the 4 OGRE EM-CCDs as well as the capabilities of the OGRE hardware and built-in software (Figure 6-3). The main components of the experimental setup are:

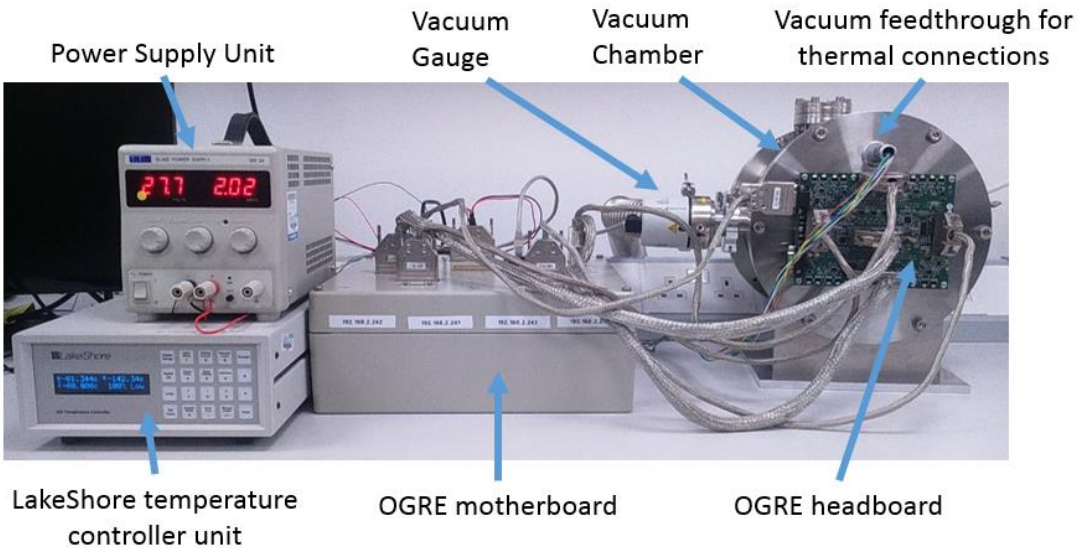

Figure 6-3: The OGRE prototype lab setup. Whilst the OGRE box has a built-in temperature controller the LakeShore temperature controller was used whilst ensuring the built-in model operated in the correct manner.

- The main OGRE box: This case houses the OGRE motherboard with its built-in power conditioning, temperature controller, RS422 communications link and BeagleBone Black processing units.
- Power Supply Unit (PSU): The on-board battery for the OGRE payload was quoted as operating at a minimum of 28V with higher voltages being available earlier in the flight and degradation occurring as the payload battery is used. The PSU for the OGRE bench has been set to the lowest operating voltage that could be experienced during the flight to ensure operations are still optimal. The built-in power conditioning will enable safe operation at higher voltages.
- The OGRE headboard: Connected to the OGRE box via insulated cabling of the same variety to be used on the flight model, the OGRE headboard connects directly to the flange of the vacuum chamber which has a built-in isolated port.
- The vacuum chamber: Made of stainless steel the vacuum chamber can hold its contents at a pressure of ~1e-6 mbar. Not visible in Figure 6-3 section of the

chamber going through the bench which houses the CryoTiger cooling unit. Using clamps and rubber O-rings other modules can be attached, for example, the vacuum tube, vacuum gauge, and push-pull modules. One of the chambers flanges is completely solid whilst the other end features a 24-way Fischer connector and the ports and screw holes to allow for the mounting of the OGRE headboard.

- The LakeShore temperature controller: Whilst the OGRE box houses its own temperature control unit it was of great importance to check it could reliably detect the correct temperature of the test system. PT100s were used for both the OGRE temperature controller and the lakeshore with two 20 Ω heater coils generating the warming element of the temperature controlling.

6.3 The mounting of the detectors

As the detectors were to be tested at a vacuum and while cooled to low temperatures it was important to ensure the mount used was secure and offered ample surface contact area to help cool the devices. Due to the nature of the design, with the headboard being connected to the flange outside of the chamber, flex circuits were needed to allow for the cooling element to run behind the operating devices.

The chosen mount was therefore constructed of copper. The unit referred to throughout as the cold bench features two ‘fingers’ with the mounting surface utilising as much of the CCD207-10 packaging area as possible to help draw the heat away. As the cooling unit is made of metal a sufficient gap was left to ensure the detector connections could not short against the copper. The rear of these fingers was slightly tapered to allow for a smoother wraparound of the flex connectors. The two heater coils were housed inside the copper cold bench using a smaller screwed on piece of copper to fully secure and surround the heater coil.

To keep the detectors held in place, aluminium clamping units were used which feature square cut-outs the same dimensions as the CCD207-40 detector packaging to allow for a secure fit and for ample area for the observation path. As the prototype camera uses CCD207-10s which are smaller than the CCD207-40 there was some degree of latitudinal movement. For this reason, the clamp was tightened whilst ensuring the devices were not making contact with the copper finger. Kapton tape was also applied in areas to reduce the chances of a short occurring without impacting the cooling capabilities. Kapton is suitable for use at low pressures as it does not outgas whilst also preventing electrical conductivity.

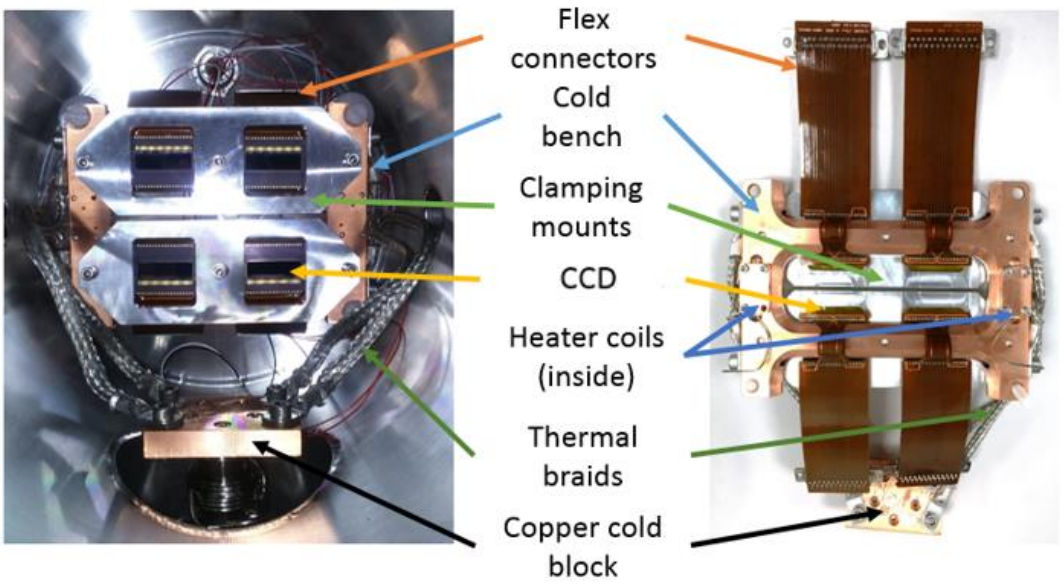

Figure 6-4: The EM-CCD mount from the front as mounted inside the testing chamber, and from the back. The heater coils are clamped in place by a smaller piece of copper on the rear side only.

6.4 Vacuum equipment

To achieve a low pressure within the chamber a Pfeifer turbopump was used. For this setup, the pump consists of two components: the HiCube 80 Eco turbo pumping station, and the HiPace 80 Turbopump. The station is responsible for monitoring the characteristics of the pump unit and can connect to a vacuum gauge to determine the pressure inside the chamber whilst also displaying useful information, such as the spin speed of the turbine

within the pumping unit. With the pump operating at its maximum rotation speed of 1500 Hz which gives a gas throughput (H_2) of 2.7 mbar l/s (Pfeiffer vacuum 2006).

6.5 Cooling equipment

To cool the detectors down, the copper cold block was mounted to a PT-30 CryoTiger head (Figure 6-5). This cold block was then connected by thermal braided cables to the cold bench to allow for the cooling of the whole system.

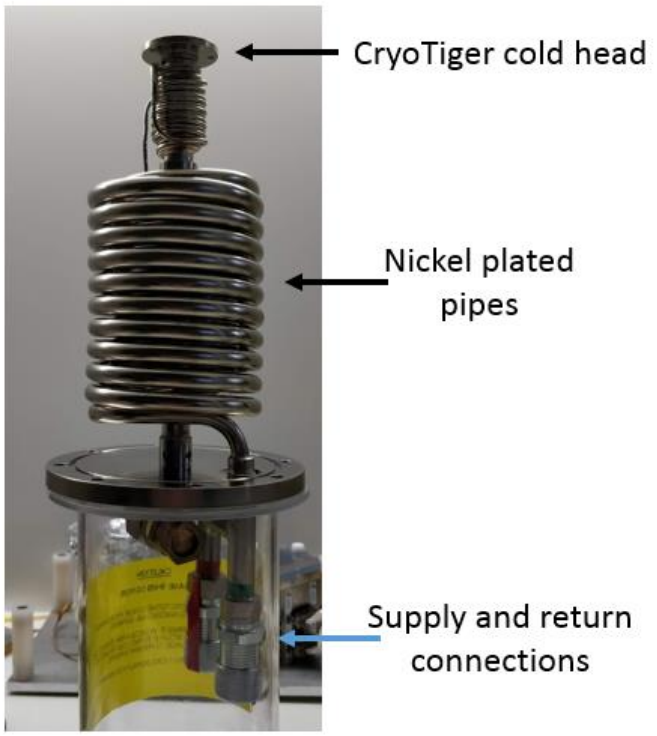

Figure 6-5: The PT-30 CryoTiger cooling unit head. Within the glass jar can be seen the supply and return connections for the coolant flow.

6.5.1 Cooling capabilities

To test the cooling effectiveness of the CryoTiger unit the test chamber was put under vacuum to prevent ice forming inside the chamber, and the detectors were left unpowered. The temperature controller was set to only monitor the temperatures and not to heat the setup.

The CryoTiger units cooling capability, a measure of its ability to remove heat, varies with the temperature it is operating at (Figure 6-6). As can be seen from the cooling capacity

curve once the temperature falls below ~130 K (-143 °C) the capacity to curve drastically falls off. As the OGRE camera system features multiple thermal regions it was therefore important to monitor how the temperature varies across these components and to determine the equilibrium state of the system.

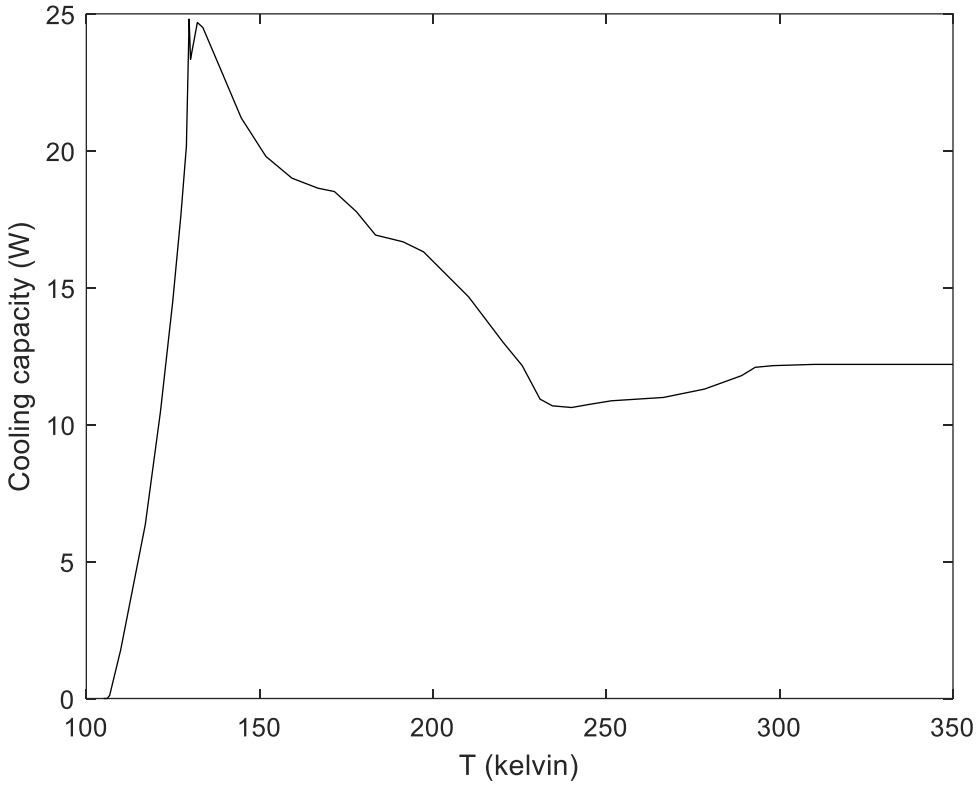

Figure 6-6: The cooling capacity of the PT-30 CryoTiger unit at different temperatures.

To monitor the temperatures within the testing chamber PT100s were used within the chamber and attached in different locations. These platinum-based resistance temperature detectors change resistance at different temperatures allowing a measurement of this to be converted to a temperature. One was attached to the copper cold bench whilst the other was attached to the copper cold block. The cooling of the setup from room temperature can be seen in Figure 6-7 with the cold mass achieving lower temperatures due to its direct mounting on the CryoTiger unit than the cold bench which is cooled via the thermal braids causing some loss of efficiency due to radiative and conduction processes.

As can be seen in Figure 6-7 the cold block can reach temperatures of around -150°C (123 K) whilst the cold bench levels off at -105 °C (168 K) so there is a temperature difference, without heating, of around 45 K.

Looking at the cooling capability of the CryoTiger at 123 K (Figure 6-6) the cooling capacity can be seen to be approximately 10 W which means the total energy gained by the system due to radiative processes and the conduction of heat from the cold bench to the cold block also equals this 10 W.

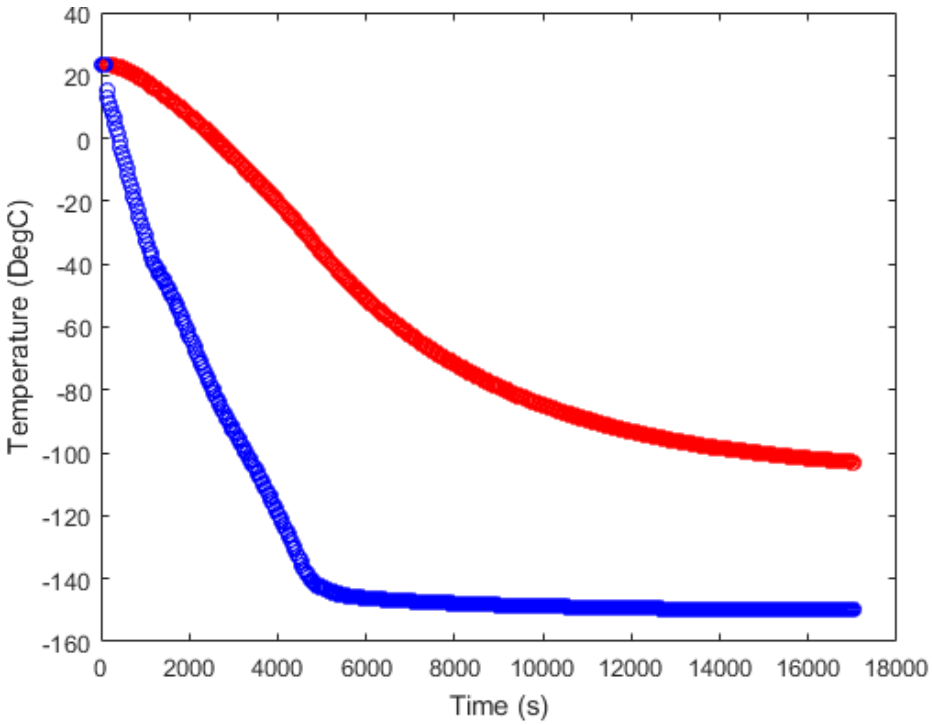

Figure 6-7: The cooling capabilities of the OGRE prototype system unit without heating elements. The red line shows the temperature of the copper cold fingers and the blue line shows the temperature of the copper cold block.

The OGRE camera will operate at a steady temperature somewhere between -80°C and -100°C so this experimental setup allows for device testing within the desired temperature range. It is of importance to determine the exact nature of the observed equilibrium temperature difference and so a thermal model was developed to simulate the cooling system.

6.5.2 Thermal model

As a large temperature difference was observed between the two main copper units of the prototype mounting system a thermal model was generated. The appropriate parameters were used to define each individual component involved.

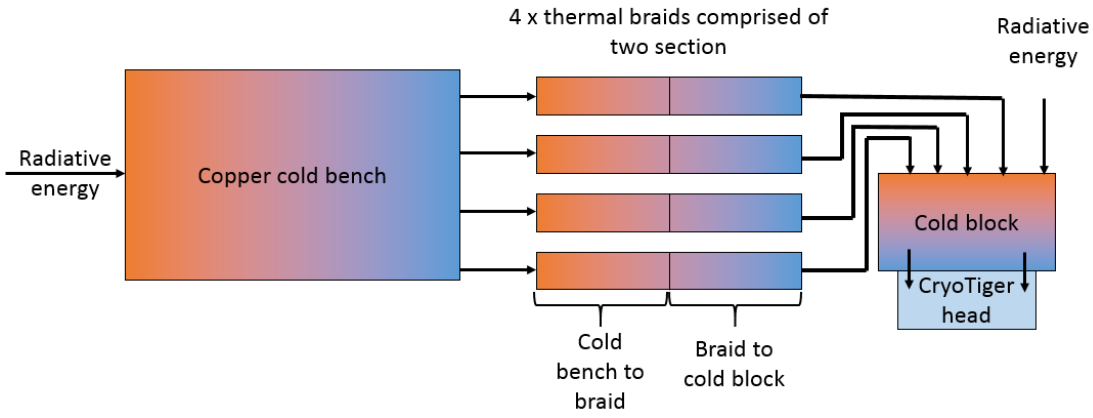

Figure 6-8: Schematic of the thermal model used with an orange to blue shift used to indicate the direction of heat flow in each component.

The system was treated as a three-part system; the cold bench, the thermal braids and the cold block attached to the CryoTiger head (Figure 6-8). The radiative heat from the chamber was calculated for the two copper units using the Stefan-Boltzmann law (6-1), with ε being the emissivity, σ being the Stefan-Boltzmann constant, A being the surface area of the unit focused on and $T_{chamber}$ assumed to be room temperature, or 296 K.

$$\Delta E_{radiative} = \varepsilon\sigma A(T_{chamber}^4 - T_{unit}^4) \qquad 6\text{-}1$$

It was assumed that the thermal braids were only given energy from, and to, the two copper units with the energy transfer being calculated using 6-2 with k being the thermal conductivity, A being the cross-sectional area, ΔT being the temperature difference between the components in the direction of the overall movement of energy (towards the CryoTiger), t being the time step used in the calculation and l being the length of the

thermal braid. A total of 4 thermal braids were used so this value was multiplied accordingly assuming each act identically.

$$\Delta E_{transfer} = \frac{kA\Delta Tt}{l} \qquad 6\text{-}2$$

To convert the energy differences into a resultant temperature change 6-3 was used with q being the overall energy change, m being the mass of the component and C being its specific heat capacity.

$$\Delta T = \frac{q}{mC} \qquad 6\text{-}3$$

The cooling capacity of the system (Figure 6-6) was used to determine the energy reduction due to the CryoTiger unit. The following thermal properties were used in the calculations.

Table 6-2: Material properties and constants used in the thermal model

Material property	**Value**
Cold bench mass	603.3 g
Cold bench surface area	0.0153592 m^2
Cold block mass	146.4 g
Cold block surface area	0.00724 m^2
Thermal braid length	0.15 m
Thermal braid thermal conductivity	385 W/g °C
Thermal braid cross sectional area	25 mm^2
Thermal braid mass	37.5 g
Copper specific heat capacity	0.385 J/g °C
Stefan Boltzmann constant	5.670367 $x10^{-8}$ W m^{-2} K^{-4}
Emissivity of the chamber	0.74

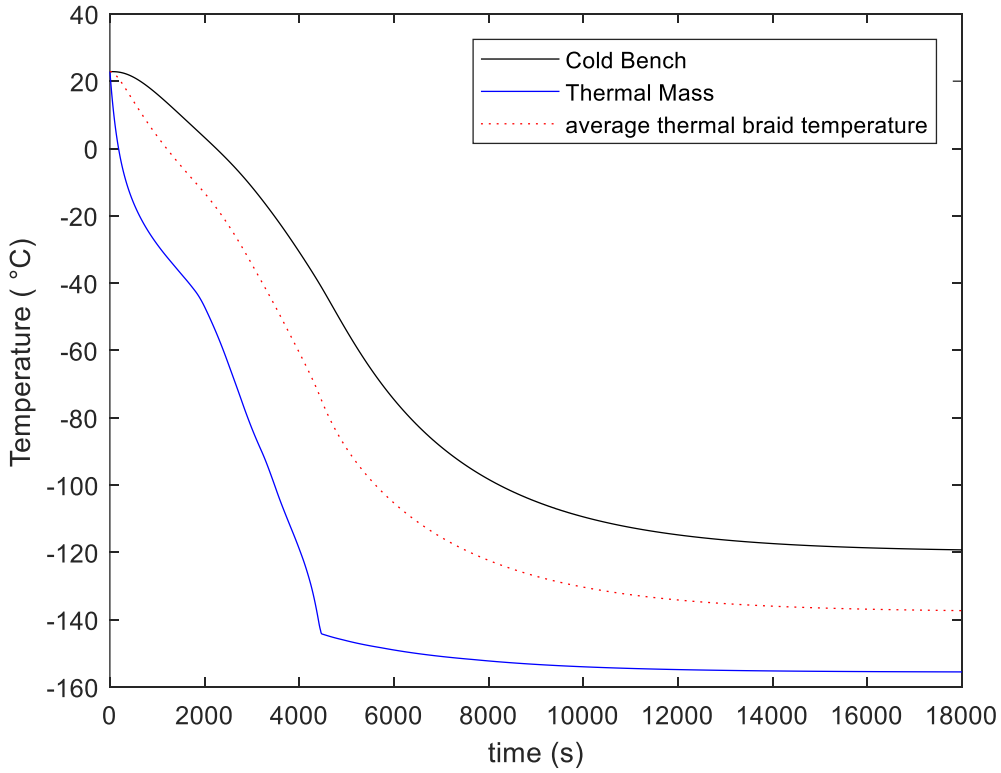

Figure 6-9: Thermal model of the OGRE cooling system

The resultant thermal model can be seen in Figure 6-9 with comparisons made with Figure 6-7. The discrepancy in equilibrium temperatures can be attributed to the following differences in energy transfer:

- Due to radiative processes from the chamber the cold bench gains approximately 6.0123 W of energy and the cold block gains 3.0666 W
- The CryoTiger unit is cooling with a capacity of 9.0789 W at the equilibrium point
- Precise calculations in the overall energy difference show a total difference of -1.57 x 10^{-6} W

6.5.3 Temperature control

To maintain the operating temperature of the detectors during the flight, a heating element will be needed to ensure the devices operating parameters do not change too

much. Whilst the final flight model will incorporate a different mount system and utilise liquid nitrogen cooling, the basic principles of the temperature controlling are the same in the prototype system. As can be seen from Figure 6-7 the detectors can be held at temperatures lower than -100°C however their operation will impart some heating into the system. If the desired operating temperature is -80°C it is therefore desirable to add some thermal energy into the system to ensure the device is not colder than desired. The temperature controller works by varying the power through the heater coils and thus generating different amounts of heat in the overall system. The more power provided the faster the heating and the higher the equilibrium temperature. (Figure 6-10)

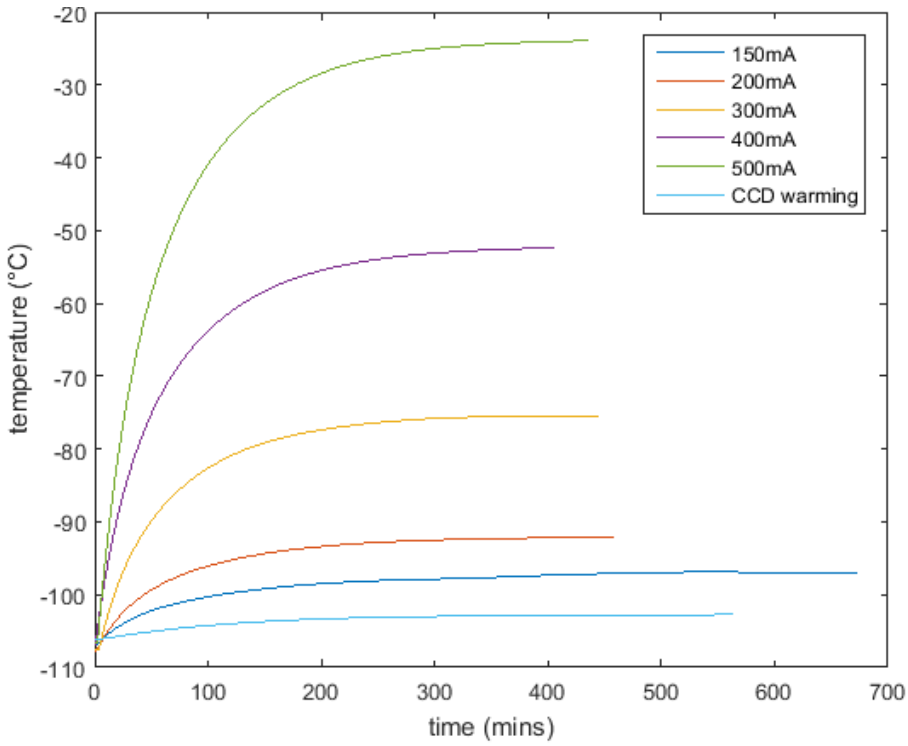

Figure 6-10: Warming capabilities with varying heating currents or with just the detectors running. The current data was taken whilst the detectors were off.

The temperature monitoring the resistance of the temperature sensors and adjusting the output power to the heater coils (Figure 6-11) to ensure the overall temperature change is

as close to zero as possible once the desired temperature has been reached.

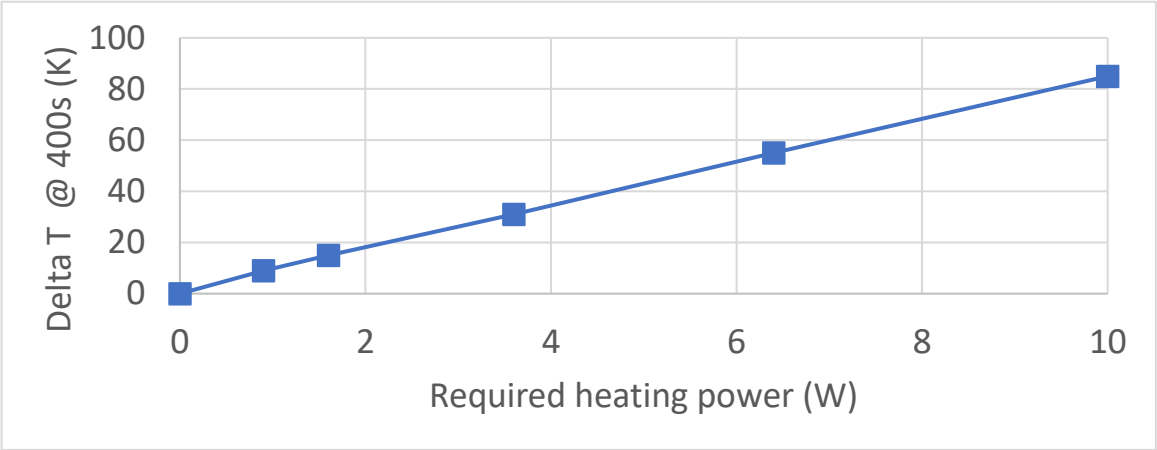

Figure 6-11: Power output required for the heating of the copper mass for different rates of heating over a set period, in this instance a 400 second window.

If the system is being warmed up or cooled down to a temperature set point the system takes some time to adapt and ensure that the system is operating at the desired temperature. If monitoring the temperature this can be seen as a small wave before levelling off at the set point (Figure 6-12). With the OGRE prototype camera setup the extreme cold temperatures can take a while to reach so sufficient time must be given to allow for the set point temperature to be reached (Figure 6-13). At some temperatures, a slight offset can be seen between the set point and the actual temperature, however it is the stability of the temperature which is of more importance due to its impact on the gain variation observed within the EM-CCD.

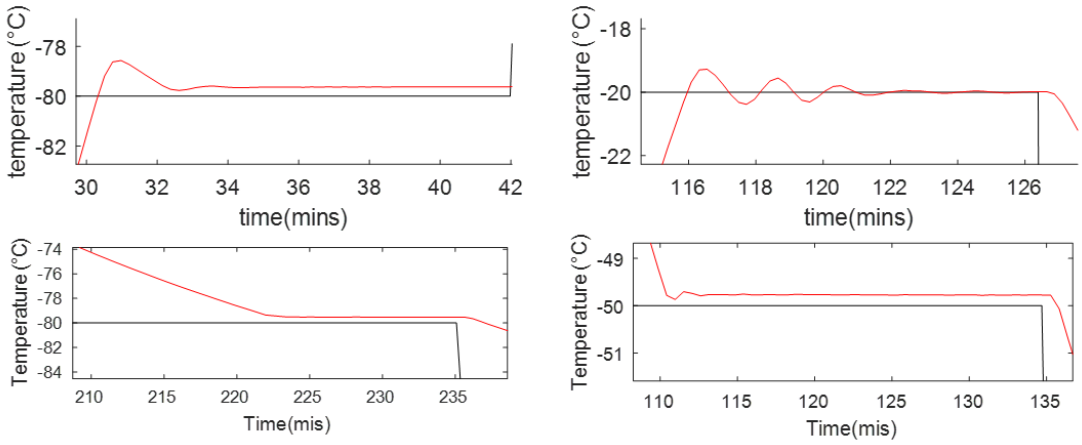

Figure 6-12: Examples of settling behaviours at different temperatures when warming up to a target temperature (top two images) or when cooling to a target temperature (bottom two images).

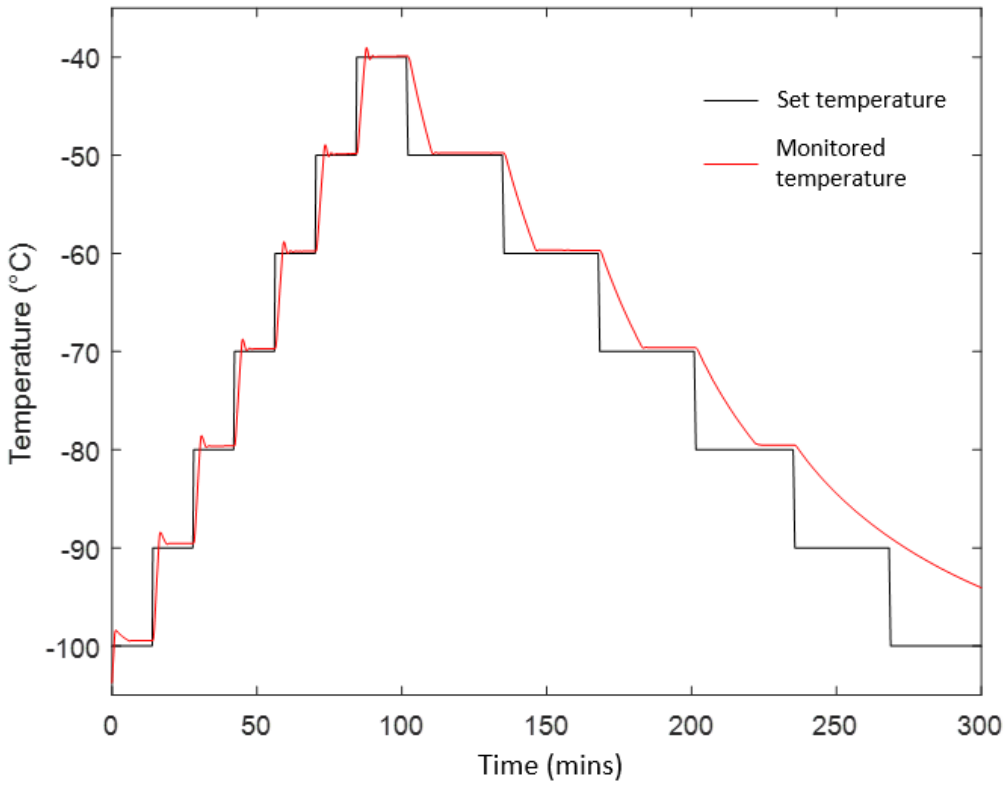

Figure 6-13: Temperature controller responsivity when changing the desired temperature set point. As can be seen when cooling to lower temperatures the system must be given enough time to reach the correct temperature.

The stability of the temperature due to the controller is also dependant on the temperature desired due to the outputting nature of current to the heater coils and the

cooling capacity of the system (Figure 6-14). Fortunately, whilst the system is cold this variation is greatly reduced and should be able to keep the overall temperature reliably within the operating requirement. The low variation also proves beneficial with the usage of the EM-CCDs as this low temperature variation will have a negligible impact on the gain used within the detectors.

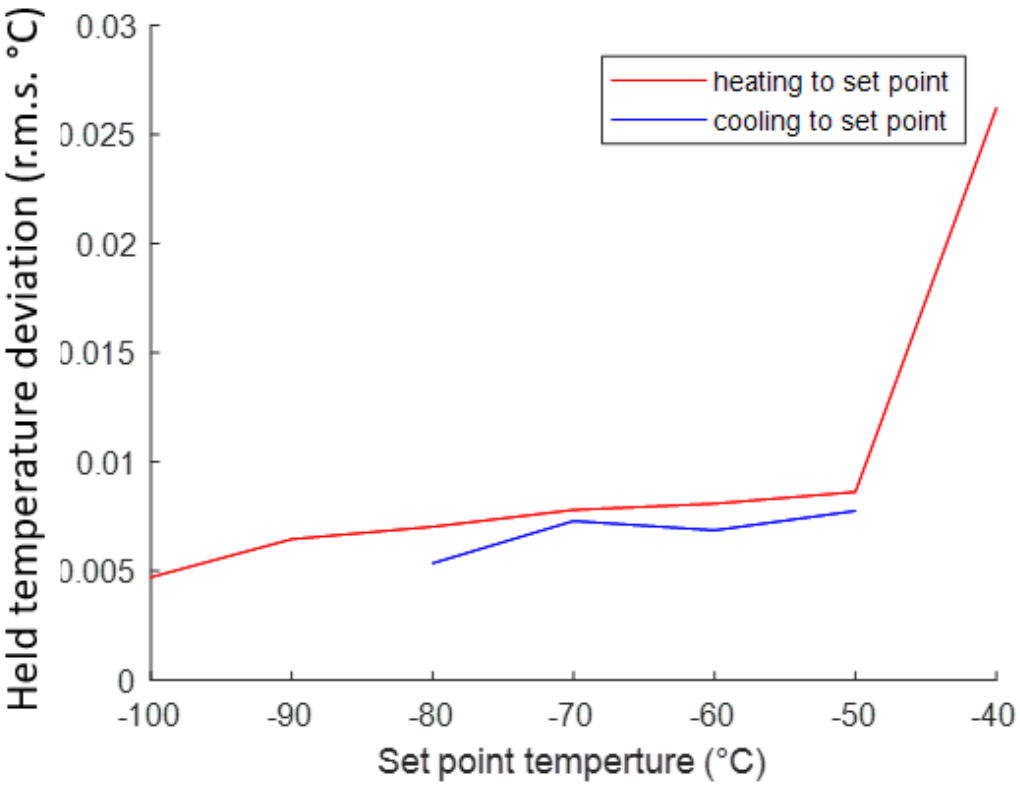

Figure 6-14: Temperature variation observed in the OGRE system upon reaching the set point temperature over a range of temperature values. Generally, the warmer the system the higher the variation.

6.6 The X-ray source: iron-55

To ensure the camera operates optimally for the detection of X-rays it is important to check its operations and calibrate it accordingly with a well-known X-ray source. For the OGRE prototype tests an iron-55 source was used which decays to Manganese-55 in one of the four following ways:

- Around 60% of the decays result in the emission of Auger electrons with an energy of 5.19 keV
- Electrons transitioning into the innermost k-shell from the second shell layer result in K-alpha X-rays with energy 5.9 keV with a 24.4% occurrence probability
- Electrons transitioning into the innermost k-shell from the third shell layer result in K-beta X-rays with an energy of 6.49 keV and an occurrence probability of 2.85%
- Low energy Auger electrons and photons from other minor transition processes account for the remaining 12%

The activity of the lab iron-55 sources is around 180 Bq when measured near the source however the mounting of the source at the far end of the chamber greatly reduces the count observed by the detectors due to dispersion. The photon count observed by the detectors is roughly 1 photon per second allowing manageable count rates over a large range of timescales.

Whilst the iron-55 X-ray energies fall outside of the desired OGRE energy range the capabilities of observing low energy X-rays can still be observed due to the gain profiles generated. The iron X-rays are around 10 times more energetic than the lowest desired Capella X-rays however the desired gains to be observed should reach into the high hundreds thus comfortably ensuring these events are increased to a detectable point.

6.6.1 Setup for testing with iron-55

The iron-55 source was screwed into a G-10 fibreglass laminate plate coated with Kapton tape to prevent the outgassing of materials. This was then attached to the flange opposite to where the detectors are mounted (Figure 6-15). The path between the iron source and the detectors was unobstructed to allow for the full energy of the photons to be incident upon the devices.

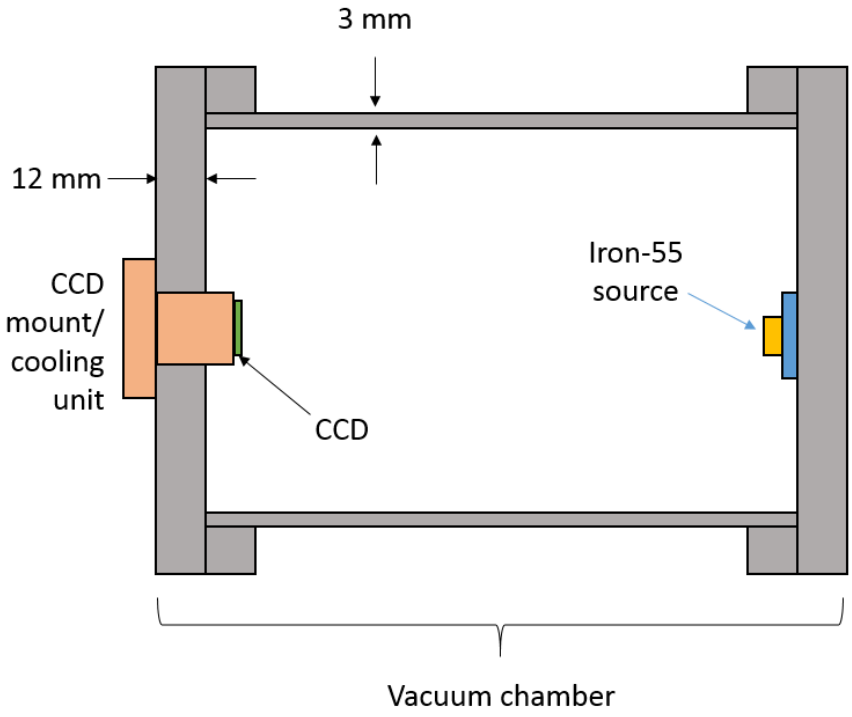

Figure 6-15: General schematic for testing a device with an iron-55 source in a vacuum chamber.

6.7 Alternative setup for the handling of strontium-90

6.7.1 The Strontium source

A Strontium-90 source was selected for specific experiments to provide electron signals in the detectors which will simulate cosmic events (Table 6-3). The Strontium-90 source has a long half-life of around 28.6 years however a secondary decay step, Yttrium-90 to Zirconium-90, occurs which has a much shorter half-life of around 2.7 days.

Table 6-3: Strontium-90 data

Strontium-90 Half-life	28.6 years
Strontium-90 Activity	5,050 x10^9 Bq/g
Yttrium-90 Half-life	64.4 hours
Yttrium-90 Activity	1.99 x 10^{16} Bq/g
Activity of the selected ^{90}Sr source	1.85 x 10^5 Bq
Strontium-90 to Yttrium-90 Beta decay emissions max energy	546 keV
Strontium-90 to Yttrium-90 Beta decay emission effective energy	196 keV
Yttrium-90 to Zirconium-90 Beta decay emissions max energy	2283 keV
Yttrium-90 to Zirconium-90 Beta decay emission effective energy	935 keV

Despite regular quotations saying the Strontium-90 source is not a gamma emitter, the decay process from Yttrium to Zirconium produces some gammas which may damage devices and cause health issues for anyone nearby. At 10cm the exposure rate to gammas is approximately 0.006 mSv/yr, considerably lower than the UK average annual radiation dose of 2.7mSv.

The strontium-90 β^- decay produces an electron and electron antineutrino with a decay energy up to 2283keV. The resultant high energy electrons can cause bright spots or streaks in the device image due to the electrons high energy allowing it pass through the device whilst depositing energy into the silicon.

6.7.2 Handling of the Sr-90

Beta radiation can be a health risk due to its ability to penetrate through skin and so the handling of the strontium source needed to be done in a secure and safe manner.
There were some concerns that the Strontium source may not be safe for use in a vacuum and would potentially outgas dangerous materials into the vacuum pump. An alternative arrangement was needed to allow for the detectors to be operated whilst still cold and at a

vacuum whilst ensuring the strontium remained in standard room conditions whilst keeping localised radiation down. (Figure 6-16) The best way to get around this was to use a flange with a Luxel 201.2 nm aluminium/ 9.78 nm polyimide/ 102 nm aluminium foil pressure window (Figure 6-17). This window features a honeycomb support structure to keep the foil strong and hold a vacuum. The strontium could then be held inside a separate chamber made of steel via a rotary dial. This allows for the strontium to be directed towards the detectors when needed with the photons able to pass through the foil window.

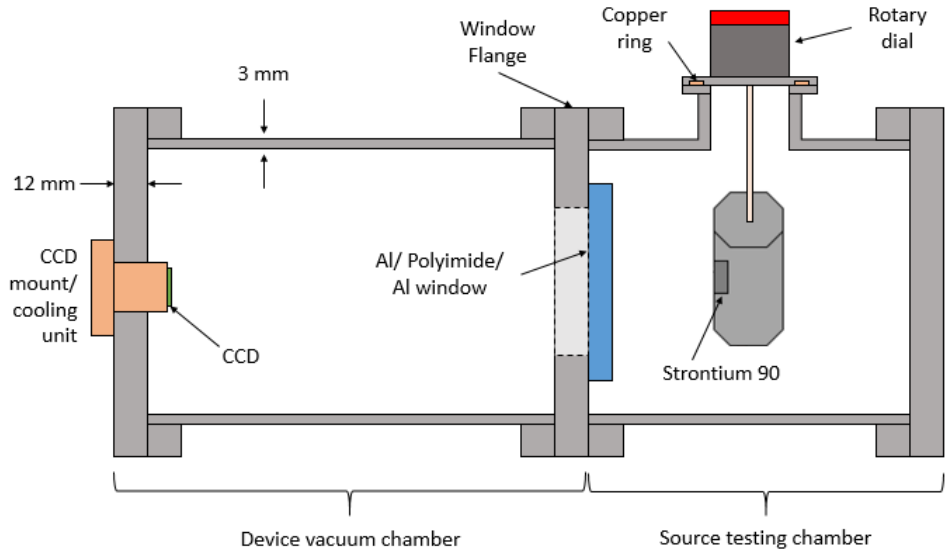

Figure 6-16: Schematic showing the test chamber arrangement when using Strontium-90. Only the region marked device vacuum chamber was under vacuum conditions.

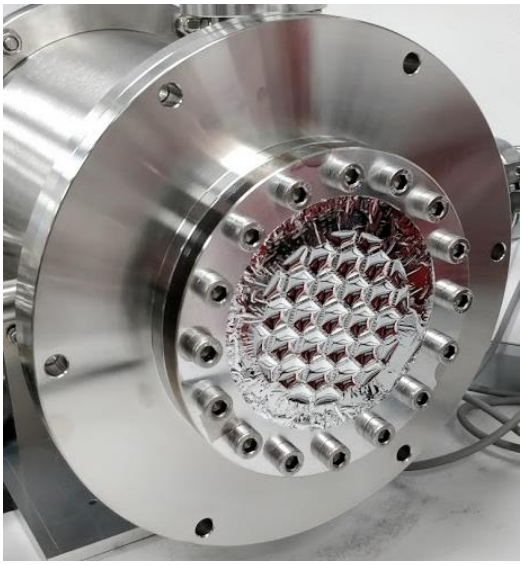

Figure 6-17: The aluminium/ polyimide/ aluminium foil window flange. The honeycomb structure within the window allows for structural rigidity, allowing the foil to hold a vacuum.

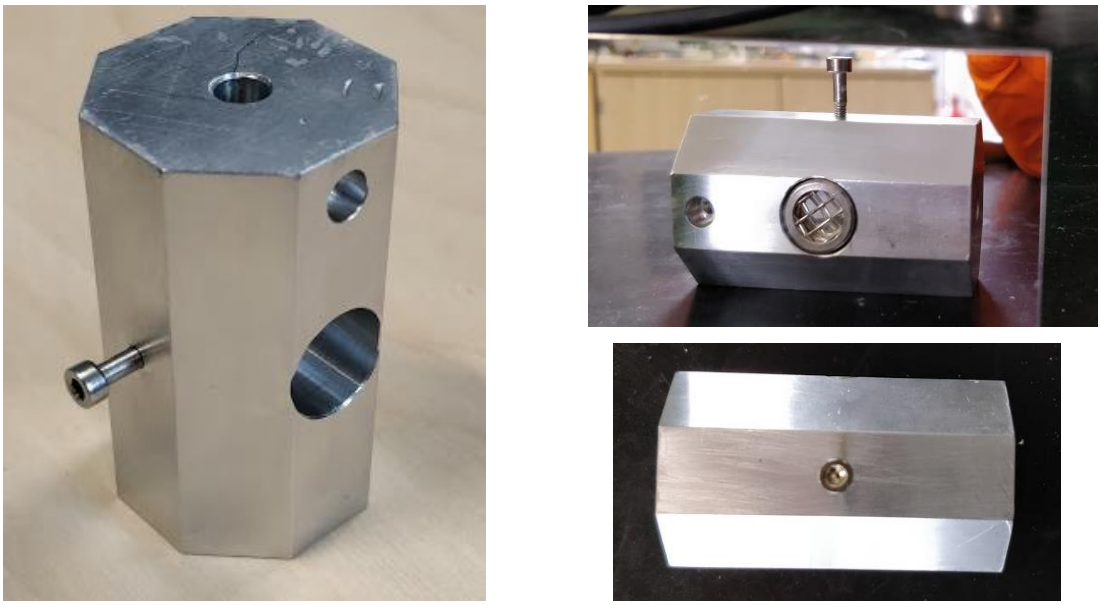

Figure 6-18: Housing for the Strontium 90 source. The bored-out region is the width of the source so will be held securely in place. The smaller hole in the back accommodates the pin and the insertion of a small tool into the rear of the housing will allow the source to be pushed out at the end of its use. The hole on the side is threaded and allows an M3 screw to be inserted which holds the pin of the source in place.

The source was mounted within a steel/aluminium alloy block (Figure 6-18) which was designed to securely fit the source, restrict the area in which radiation occurs, and allow for its safe removal. The source features a pin which is used to secure its place via a locking M3 screw.

The high energy emissions of the Strontium-90 can cause damage to any test devices if they are exposed for long periods of time. The rotary dial allowed the strontium to be pointed away from the detectors when tests were not being carried out. The chambers were of sufficient thickness to prevent any photons from reaching outside the chamber ensuring a safe operating environment.

6.7.3 Experimental procedure

The tests regarding the strontium-90 source require the presence of an iron-55 source as well. The ideal scenario for the dataset was to therefore revolve around 4 scenarios;

1) Testing of the detector background with no radiation sources present.
2) Testing with the iron-55 only to get an X-ray input only.
3) Testing with the Strontium-90 only to determine the effectiveness of its use to simulate cosmic style events.
4) Testing with the iron-55 and strontium-90 present to allow for tests on the event detection algorithms and its ability to isolate X-ray signals from other charge sources.

The iron-55 was therefore mounted on an additional push/pull system to allow for it to be moved in and out of position, essentially turning it off and on. This was used inside the vacuum chamber to give a better ratio of X-rays to cosmic style events due to the X-ray source being closer to the detectors.

6.8 Summary

The precise testing of the CCD207-10 had to be carried out using precisely controlled conditions to allow for ideal operating conditions like those the detectors will be in on launch day. The greatest difference between the laboratory arrangement and that of the flight camera system is the method of cooling as a powered cooling unit will not be used on

the flight system but instead will be cooled via LN2 supplied via an umbilical. The precise heating of the thermal mass used in the flight is to be carried out by XCAM Ltd.

The system can use four detectors upon proper operation however due to the nature of the engineering grade detectors provided for use in this project several of these were operating in a far from ideal manner (damaged sections, high dark signal) and so the rest of this thesis focuses on data acquired from the best of the detectors provided which was observed to have more background signal than a top-grade device.

This detector is still capable of observing the photons generated by the iron-55 and strontium-90 sources. As radiation damage can occur to EM-CCDs over the course of their lifetime care was taken to ensure the detectors within the vacuum chamber were only exposed to X-rays for as long as the observations were needed.

7 Characterisation of the OGRE camera

The successful detection of X-rays is crucial in the OGRE project and so the proper operation of the detectors will be needed to a high degree of reliability in terms of the device's performance and sensitivity. To ensure the detector capabilities are fully utilised on the mission it is best to characterise the devices to better understand how they behave and can be more precisely tailored to the mission's needs.

It should be noted that the tests throughout this chapter focus on the CCD207-10 instead of the flight detectors, CCD207-40s. As discussed in previous sections these devices share the same properties in all ways except for the CCD201-10 featuring 400 image rows whilst the CCD207-40 features 1600 image rows. The devices used in these tests are engineering grade 5 detectors whilst the flight camera will feature top end, new detectors so whilst some adjustment will be needed in when using the flight camera, the general behaviour and values will be near enough to allow for a quick and easy setup.

7.1 Requirements for the OGRE mission

The success of the OGRE project is dependent on each of the key components operating in a specific manner to successfully observe the X-rays from Capella. The optical module and gratings must successfully focus the photons into the correct areas to a high degree of accuracy to create the arc of diffraction. It is then the objective of the camera to ensure these X-rays are successfully observed and their positions seen to a high degree of accuracy and clarity. To safeguard the likelihood of the camera operating productively towards the aims of the mission a set of component requirements were constructed to ensure OGRE camera operates in a manner to declare the mission a success.

7.1.1 Signal observation

The camera should be able to observe X-rays clearly with a negligible chance that a source of noise could be construed as a desirable photon. The use of an EM-CCD camera will ensure that the charge packets generated within the image area of the device will be amplified significantly above other noise sources. The signal-to-noise ratio (referred to as S/N henceforth) is therefore larger than a standard CCD. To ensure the events observed by the camera are reliably the Capella X-rays it was set that S/N should be a minimum of 100.

7.1.2 Gain requirements

No set gain value was assigned to the mission with the objective being to ensure clear detections whilst using the multiplication utility of EM-CCDs to reduce the impact of readout noise and make observations clearer. An issue with multiplying signals generated within the image area is that any charge generated within the image area by undesirable sources which has a higher energy than the target X-rays will also be multiplied. The full well capacity of the device needs to be considered to ensure that once this undesirable charge has been multiplied the impact on the image is not too severe. This means that whilst ensuring the gain is significant to observe the 600 eV to 1200 eV energy range OGRE will focus on, it should not be used excessively to ensure a greater likelihood of a usable image. The controllability of the gain should also be well-known to allow for a change mid-flight to the operating parameters should issues arise (i.e. excessive signal, large variations in temperature).

7.1.3 Spatial resolution

With OGRE being a spectroscopic mission the position of the photons on the devices is the key to deriving the spectrum of Capella. For this reason, the spatial resolution of the detectors needs to be sufficiently high to not be the limiting factor of the telescope's capabilities. The design of the payload is such that the X-rays will be sub-apertured or

focused in a non-universal manner, i.e. there are multiple possible component paths X-rays may take through the system. Whilst a full 360° optic would produce a distribution pattern of a circle with a higher density centre, each OGRE diffraction arc only uses 60° of the circular aperture. This generates a bowtie style distribution pattern. Whilst oriented in the direction of dispersion the OGRE point spread function from the optics and gratings will cover a 49 μm (width) by 2 mm area, the equivalent to 3.06 pixels by 125 pixels. This will be orientated by 30° (Figure 7-1).

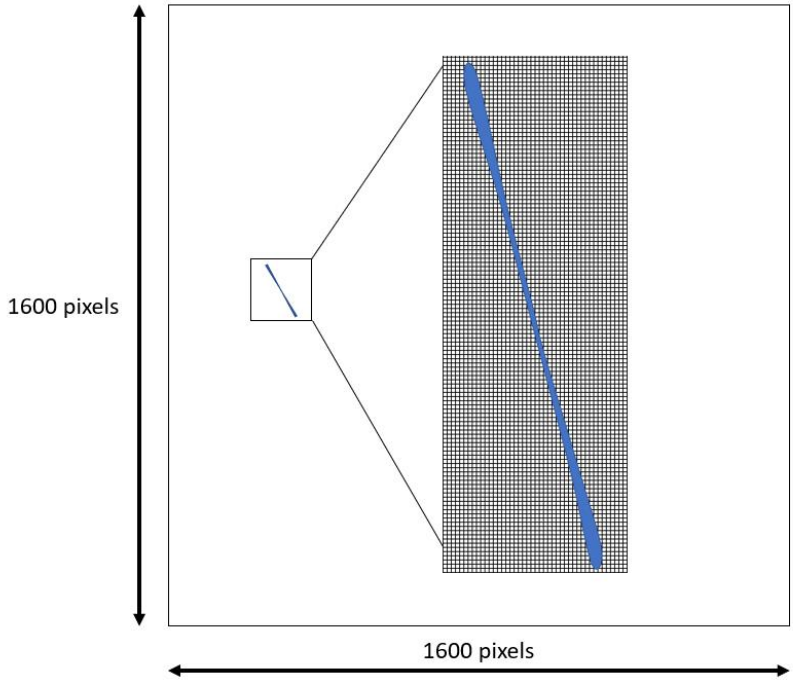

Figure 7-1: Point spread function region of the OGRE instrument for a photon at a single energy level. This figure shows the variation in position at one energy value relative to the size of the EM-CCD with a zoom to show this at the pixel scale.

Throughout the duration of this project the different designs of the OGRE payload have meant a variety of spatial conditions have been set at different points throughout the project timeline. The design has allowed for discussions regarding the operation of the detectors in varying manners to better utilise the spatial readouts of the detectors via different processes. Two different methods were looked at as part of this thesis,

windowing, and parallel binning, which will be discussed in their own sections later in this chapter.

7.1.4 Timings

The nature of a sounding rocket mission means that observation time is precious. With the updated design the simulation estimates 3128 X-rays will be incident on the detectors over a 6-minute observation. This gives an average overall flux of 8.7 X-rays per second, so roughly 3 X-rays per second per detector. The operation of the camera requires some time to reset the device ready for photon integration as well as to read out the image with most of the time desirably being spent on integration. To try and maximise the time spent collecting science data a 10 to 1 ratio of integration time to non-integration time was established to reduce the number of out of time events occurring, i.e. lost useful information.

To fully utilise the advantages an EM-CCD would bring it was also decided that the camera should operate with a 1 Hz image acquisition to generate 60 images per minute. This will minimise the likelihood of X-ray event pile-ups and the contribution of instrument background sources due to non-Capella events, such as cosmic particles passing through the system. The payload will ideally work on a constant cycle so maintaining a 1 Hz operation will allow for constant power consumption throughout the flight allowing adequate power supplies to be used during the launch. The star tracker which will be used to maintain the rockets pointing towards Capella is likely to operate at a frequency of 2 Hz so differences in the pointing accuracy over the time the image is acquired will be known and can be considered during later analysis.

7.2 X-ray events

7.2.1 Standard image format

Due to the process in which an image is generated the resultant data set constructed from an image grab is comprised of a two-dimensional array of Digital Numbers (DN) as opposed to the resultant charge found in the device. Some noise is present within the image which has the potential of masking the signals from the incoming photons.

There are also a variety of event types that can be observed within an image (Figure 7-2). For an X-ray, the ideal signal would be a single bright pixel, however commonly the pattern observed is a bright peak in a small area with some charge distributed to the neighbouring pixels. The resultant peak makes it easily observable amongst the rest of the image. Other events may be split over neighbouring pixels which result in a region that is still noticeably larger than the non-photon generated signals but not as immediately obvious as the former scenario.

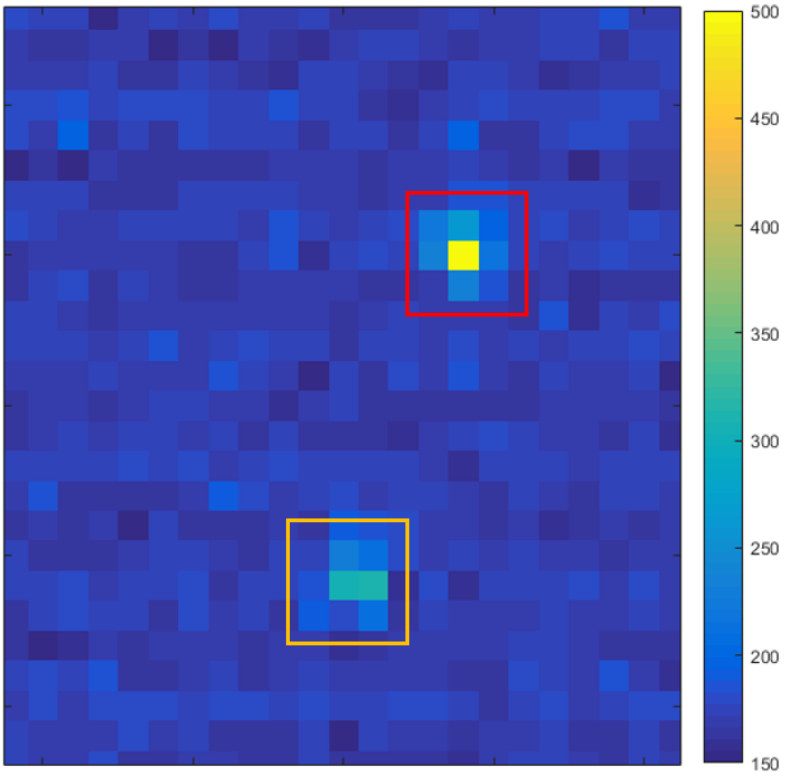

Figure 7-2: Typical X-rays on an unprocessed image with a low gain captured with the OGRE prototype camera system. The red square shows a classic X-ray with the central 'bright' pixel being surrounded by smaller charge packets. The yellow square demonstrates a split event. The image is generated using the DN of each pixel.

The resultant image must be processed to make the important data stand out without reducing the scientific credibility of the image. Whilst obtaining the image from the detector an offset region is created by reading out additional non-existent pixels after the image section, the over-scan region. This over-scan can be used to find the added signal due to the electrical offset of the device's operation and thus subtracting the mean of this offset value brings the image values closer to that of the signal generated by the target photons.

It can also be assumed that most of the image will not be due to photon interaction and so is the device background. For the CCD207-10 which has 640,000 image pixels even with

100 photons randomly scattered across its imaging surface, each affecting a 5x5 pixel region, the background signal would still constitute 99.6% of the total image area. The flight detectors, the CCD207-40, will feature areas where X-rays should not have any possibility of reaching due to the spectroscope nature of the payload. As well as observing less X-rays per image and having a greater number of pixels the effects any X-rays on the overall mean image value will be negligible. Taking the mean pixel value of the entire image and subtracting it from the output image will therefore remove most of any noise inherent in the image region of the detector. There will still be some variation in the background due to variations in the readout noise and any background offsets however many of the background pixels values will now be small in value either side of a 0 DN.

7.2.2 X-ray calibration

With the signal properly isolated from the offsets due to the device operation it is possible to compile event data into a histogram depicting the observed spectra within the testing chamber (Figure 7-3). The histogram will still show several features. The background will still be apparent due to the large number of pixels which fall into this category. A second peak represents the X-rays observed from the Iron-55 source. This peak has a known energy of 5.90 keV and so fitting the observed device output with the expected iron-55 observations allows for a conversion factor to switch from DN to the number of electrons generated within the pixel. The gap between the two peaks in the histogram are split events which are unusable for calibration purposes.

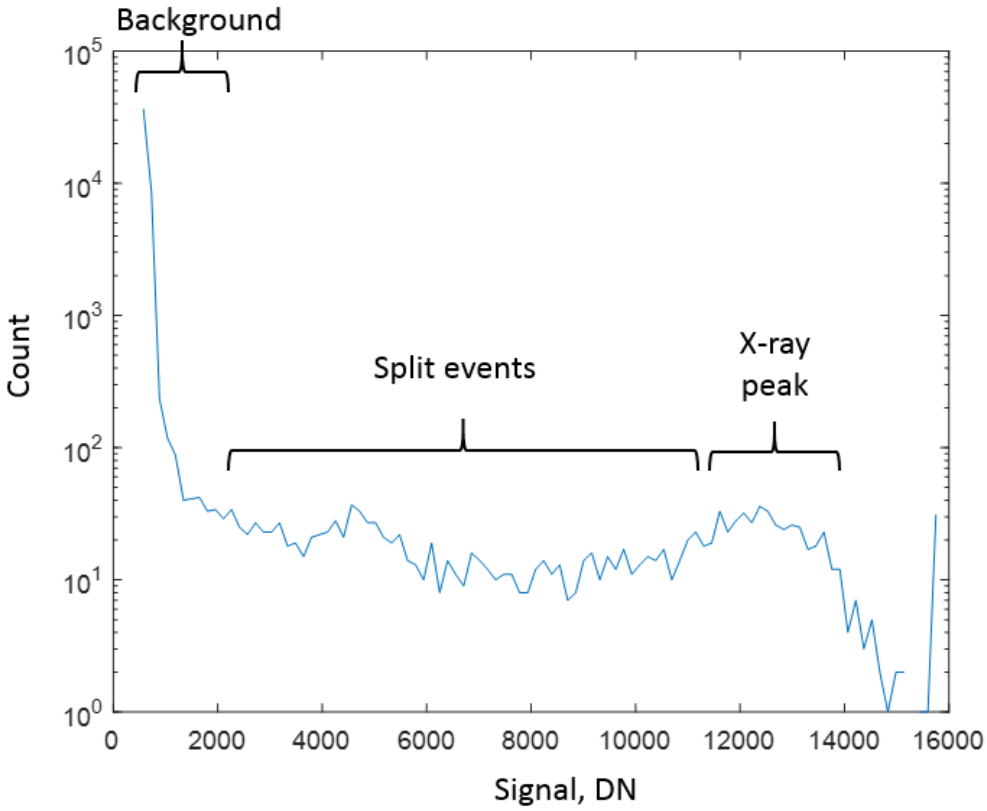

Figure 7-3: Spectrum over several compiled images at high gain

One factor which must be considered when using EM-CCDs is the gain on the device. As the signal is multiplied during the transfer to the readout node the number of electrons generated within the image area per event are the same regardless of the gain. The number of electrons is only increased just before readout and so a conversion factor is needed based on the gain being used (Figure 7-4). As the X-ray peak does have some width and the gain of the system is not a constant factor for each pixel due to the probabilistic nature of the system, the calibration value does have some error when higher gains are used.

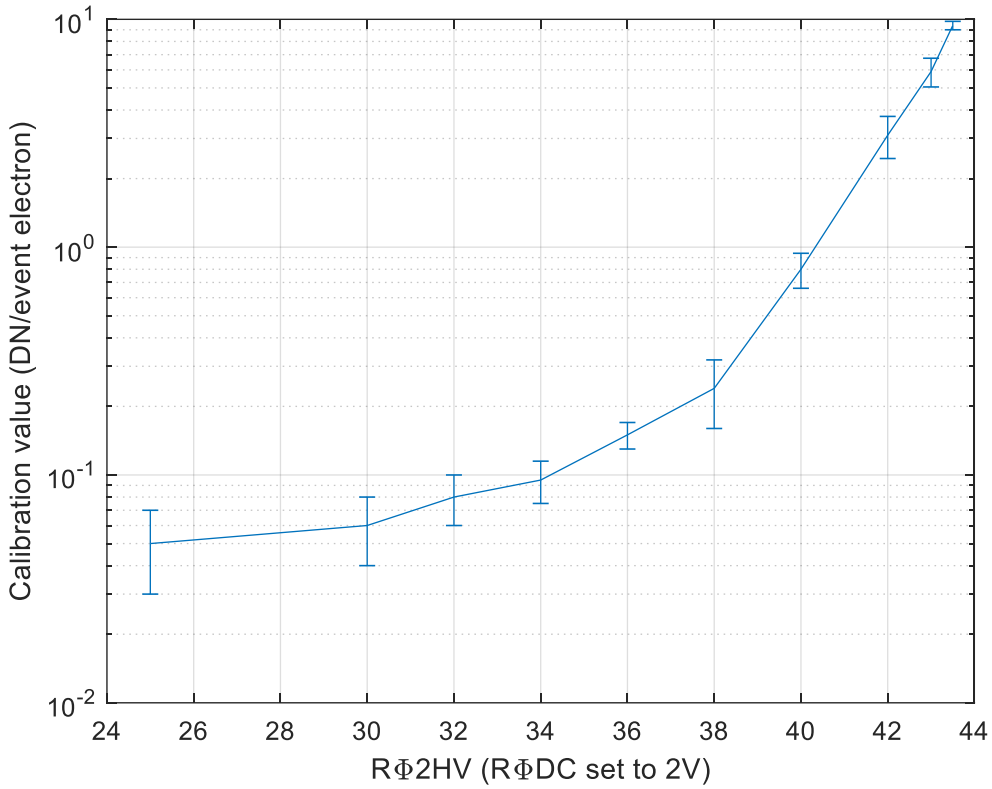

Figure 7-4: Calibration values for the CCD207-10 operating at various HV voltages when the detectors are held at - 80 °C.

7.3 Sensitivity of desirable operating factors

7.3.1 The variation of gain with HV

As detailed in section 4.6.1 the electron multiplication of an EM-CCD is determined by the voltages applied across the multiplication elements of the device during image readout. It is the acceleration of the electrons over the large potential difference which causes impact ionisation to increase the charge within the charge packet. Utilising a larger potential difference will increase the chances of impact ionisation occurring due to the greater acceleration the electrons undergo. To see how this voltage, referred to as RΦ2HV, affects the overall gain of the device, the X-ray signal at various voltages was compared to the signal observed when there is no multiplication factor, i.e. standard CCD readout (Figure

7-5). The gain is found by the x-ray peaks DN-to-energy conversion factor at a set voltage divided by the same conversion factor when no gain is applied.

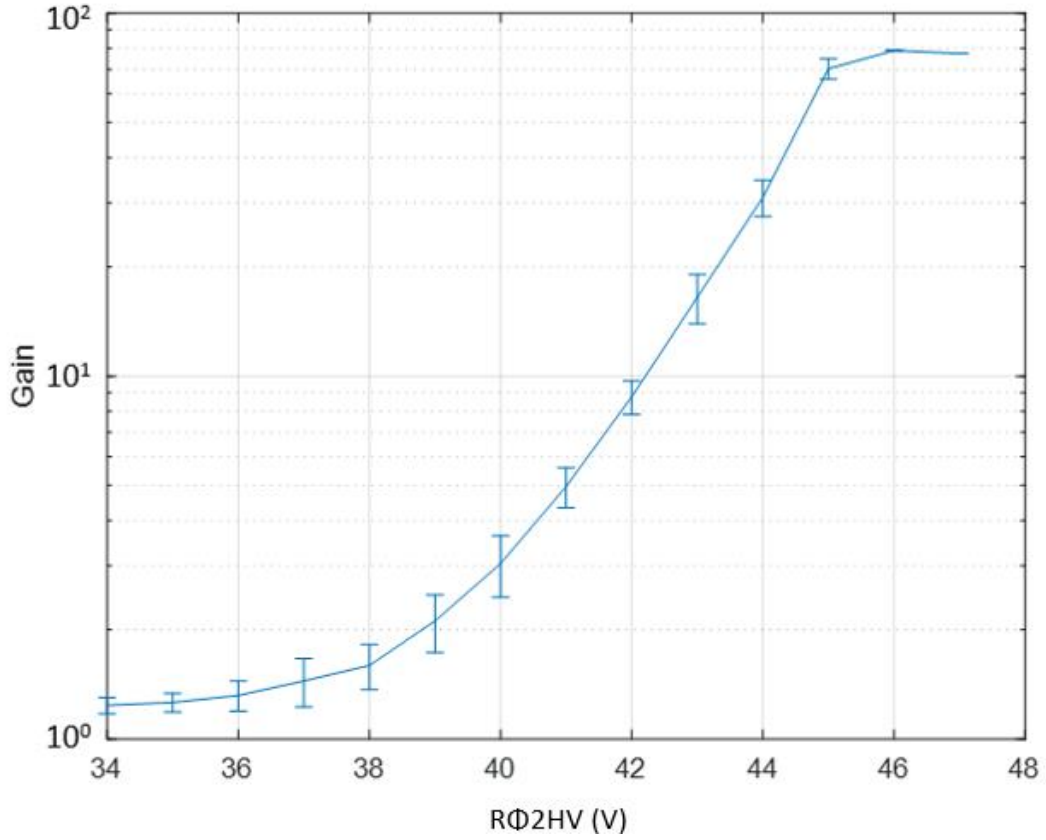

Figure 7-5: The observed variation in gain when the RΦ2HV voltage is adjusted with a calibration value set to the output value of an X-ray at gain of 1, (i.e. no increase of signal) with the devices operated at -80°C.In this instance the gain is calculated based on a pre-set event size of 5 x 3 pixels.

As can be seen even with a log plot the gain in the system increases drastically with a larger HV voltage. The levelling off observed at 46V and higher is due to the device reaching its maximum output values causing charge to spill into neighbouring pixels and producing a smearing on the output image. As the X-ray event is generally calculated based on a localised event, this smearing means some of the signal generated and spreading to neighbouring pixels is lost in the event calculation, with the levelling off being due to the event area saturating.

The saturation of pixels with large gains highlights the need to ensure the gain of the detectors in the mission are controlled to prevent larger signals affecting other pixels and causing a potential loss in usable scientific data.

7.3.2 The temperature dependence of gain

The resultant curve in section 7.3.1 was acquired whilst the temperature of the system was held at -80°C to ensure the temperature of the system was not a factor in the changes observed in the gain. The device datasheets highlight the variability of the EM gain with colder temperatures increasing the gain observed. During the OGRE launch, the temperature variation of the camera will ideally be kept to a minimum to prevent changes in the gain unless the gain voltage (RΦ2HV) is changed. Understanding the temperature dependence of the gain allows for some mitigation of the gain effect should the temperature of the system start to vary too much from the desired value.

The HV-gain test was repeated at multiple different temperatures in an identical manner to ensure the gain variations observed are due purely to the temperature of the system (Figure 7-6). As can be seen the gain at a set gain voltage on a cooler device is higher than that of a warmer device.

It has therefore been shown that to maintain a set gain value during the OGRE flight where a positive variation (if any) is most likely to be seen the gain voltage, RΦ2HV, can also be increased to counter the effect of the temperature change. The decision of whether this should be an automated process on-board the rocket or a change made manually from the ground control station is yet to be decided however once a desired gain is known similar curves to that seen in Figure 7-6 will be used to derive an equation to calculate the correct voltage for our target gain.

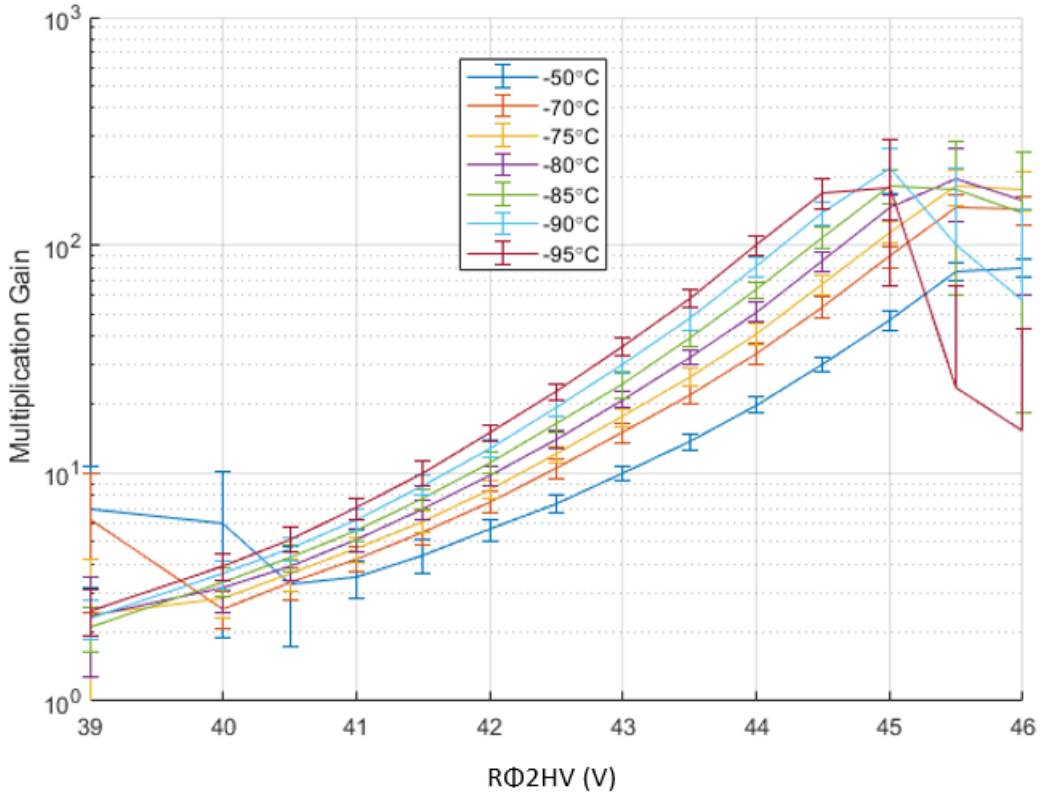

Figure 7-6: HV gain curves with a calibration value set to the output value of an X-ray at gain of 1, (i.e. no increase of signal) with the devices operated at seven different temperatures. The breakdown at the lower gains is due to other events detected as X-rays within the device which are not present due to the iron-55. The cooler operating temperatures reduce this effect. At the higher gains and colder temperatures, the curve breaks down as the system start to identify larger areas of oversaturation and picks up other multiplied sources which resemble X-rays of lower energies.

7.4 Sensitivity of noise sources

With the operation of the camera system it is important to definitively state that the results being observed are due to the desired observational target. At times noise in the device could reduce the reliability of a given observation thus it is of great importance to monitor how noise in the device can vary under different conditions allowing it to be minimised and for further refinement in the data should issues arise during collection.

7.4.1 Temperature and dark current

A form of noise inherent in CCDs, the dark noise is produced in all pixels and ideally would form a uniform background signal. If this dark current varies greatly then it could potentially obscure low-level signals that the observer would like to investigate.

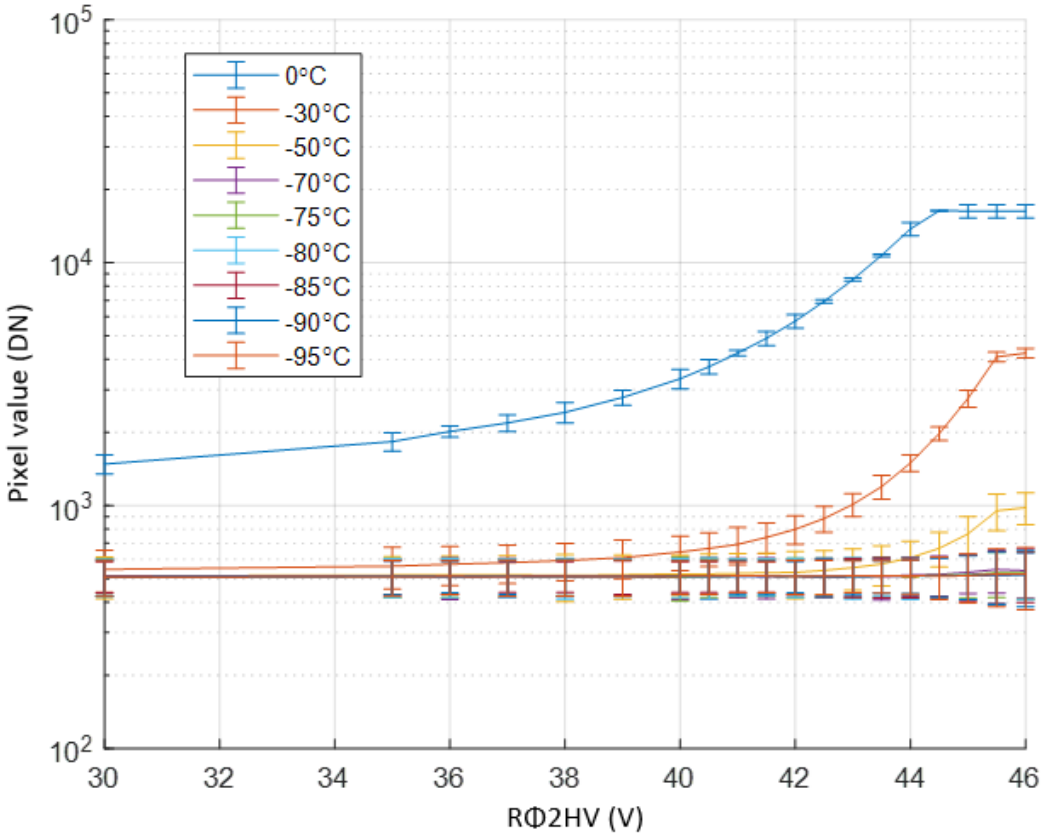

Figure 7-7: Plot of the mean of the raw image section pixel values with no X-ray source present in the testing chamber at varying gain voltages and operating temperatures.

The dark current generation rate is known to reduce with colder temperatures. Figure 7-7 shows the dark current observed for varying gain voltages and temperatures. At warmer temperatures, a curve can be observed showing the dark current is significant enough to undergo multiplication in the EM register to a degree it will impact any scientific observations, a condition which is not ideal. As the temperature decreases this curve becomes less pronounced until eventually the pixel values do not appear to vary with the gain voltage. This shows that whilst the EM gain can reduce the effects of readout noise,

dark current is still a big noise factor due to its generation before passing through the multiplication register and so must be minimised. The overlapping of the different temperature plots shows that the electrical offset has been found (a DN of ~520) and thus the expected dark current of the device could be obtained from this value once other noise sources are removed.

The other observation to be made is in the errors. For the temperatures giving a mostly flat line on the plot the variation can be seen to increase slightly. This is to be expected as any signal passing into the EM register will undergo impact ionisation if there is a significant enough gain voltage applied.

7.4.2 Effective readout noise variation

The readout noise is independent of the signal in a pixel and is instead added by the electronics of the output circuit and off-chip electronics. This should allow the read noise factor when using high gains to be significantly supressed as the added value relative to the charge packet will be reasonably small.

Figure 7-8 shows the mean of the over-scan region at different gain voltages and temperatures. As can be observed, there is no real variation in the device if the system is cooled. There are some odd effects in the over-scan region when the device is warm (0°C or -30°C) but generally the readout noise is well characterised.

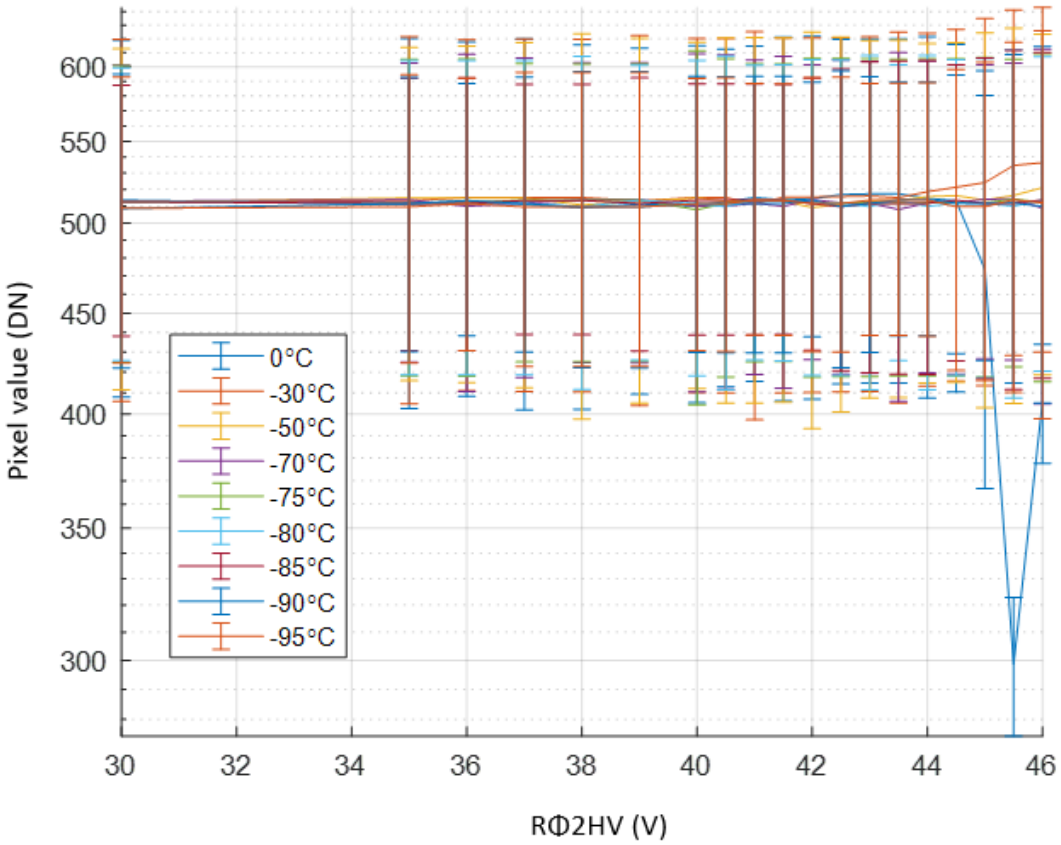

Figure 7-8: Plot of the mean of the over-scan region of the detector at varying gain voltages and operating temperatures.

7.4.3 Overall noise suppression

The observed offset value when looking at the image background (dark current signal) was approximately 520 and the over-scan noise can be observed to have a DN value of ~510. If it is assumed the dominant source of this difference is the dark signal, then a constant DN value of 10 is observed for the dark current.

Keeping in mind that if this value is constant at a given temperature regardless of the gain and looking at how the calibration value varies by gain voltage it is simple to see how the noise is supressed. Looking at Figure 7-4 when operating with a gain voltage of 43V the calibration value is 6 DN/e^-. This would therefore mean the dark current noise of 10 DN is equivalent to 1.6 electrons. This number will ideally be below 1e^- for the duration of the

mission. As the mission will launch with new, higher quality devices, this should be easily achievable.

7.5 Spatial resolution

7.5.1 Artificial reduction of the image area

The 1600 by 1600 pixel image area of the CCD207-40 is a desirable trait for many practical uses, however with the arc of diffraction focusing on only a fraction of the device many pixels will essentially be unutilised. If the images read out can be reduced in size without affecting the science, then this would be preferable for the timing and data aspects of the camera's operation. Two possible methods have been put devised to approach this with there being a possibility to combine both methods into one.

7.5.1.1 Windowing of the device

With the arc falling across the columns of the detector but missing many the rows it is possible to introduce windowing to reduce the image size. By emptying out certain rows without reading the data the final image size will be purely that of the window. This method of image reduction has the benefit that all the pixels seen in the final image have not been altered in any way and if the number of rows emptied out is known the y-position/ row number on the device can also be inferred as well as decreasing the overall readout time of the device allowing for a greater integration time.

One factor which may negatively impact the windowing of the images are non-desirable events that occur just outside the windowed region. If a highly energetic particle were to be incident near the window boundary, its effects may cause some interference with surrounding pixels. The windowing will remove said event from the image however the affected pixels will demonstrate additional charge over the expected amount. As the event itself has been removed from the image in a destructive manner (i.e. there is no recovering

the event data) there is no way the interference can be properly diagnosed. If the window allows for some degree of error around the arc position no science should be lost, and any undesirable interactions in the device can be observed which will make the classification and rejection of Capella X-rays more reliable. These error boundaries can be found by taking any sources of error from the system, such as alignment variation or instrument point spread functions into account (Figure 7-10). The exact position of these error boundaries will be better known upon construction of the optics and gratings modules and can easily be programmed in once known.

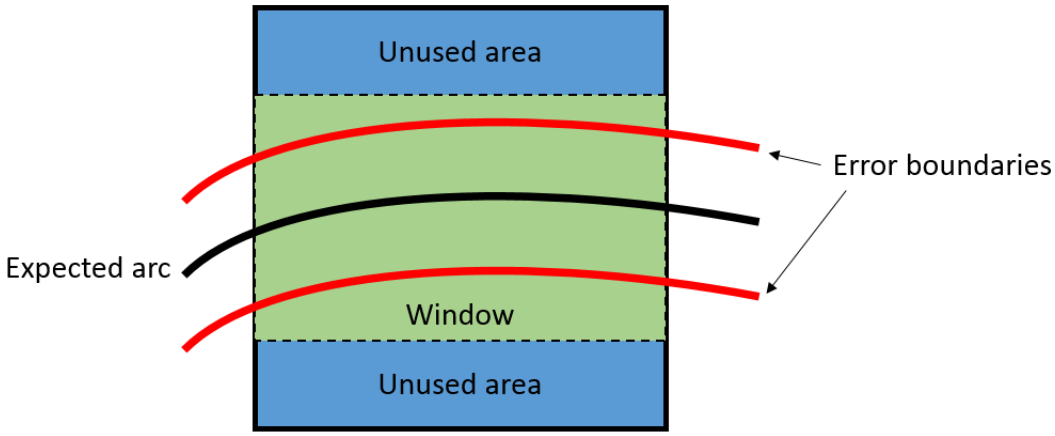

Figure 7-9: A schematic of how windowing could be applied to a device whilst taking error boundaries from misalignments and point spread functions into account. This example sees the final image size (the area in green) being 60% of the detectors image area.

7.5.1.2 Parallel binning

If the x-axis position is the only value obtained from the resultant images to be used in the calculation of the X-ray's energy value, the deviation of the signal in the y-axis is no longer of significant importance and could therefore be combined within a single pixel producing a smaller resultant image. Parallel binning involves moving rows into the readout register without reading out the prior row. Doing this multiple times effectively combines the charge packets of the rows. As an example, if five-pixel parallel binning with no windowing

were to be utilised, five rows would be moved into the readout register before the readout process begins. The readout process is as usual. The resultant image would then be, if using the CCD207-40 with an initial 1600 by 1600 image area, 1600 pixels by 320 pixels image.

The largest advantage with this style of image reduction is the now smaller image will take less time to process, save, and undergo on-board analysis than the full-size image. The image is still two-dimensional however most of the y-data will have been compressed down into a smaller region (Figure 7-10) meaning exact positional knowledge has been lost. The exact signal observed within each pixel has now also been combined so the values within each individual pixel have also been lost.

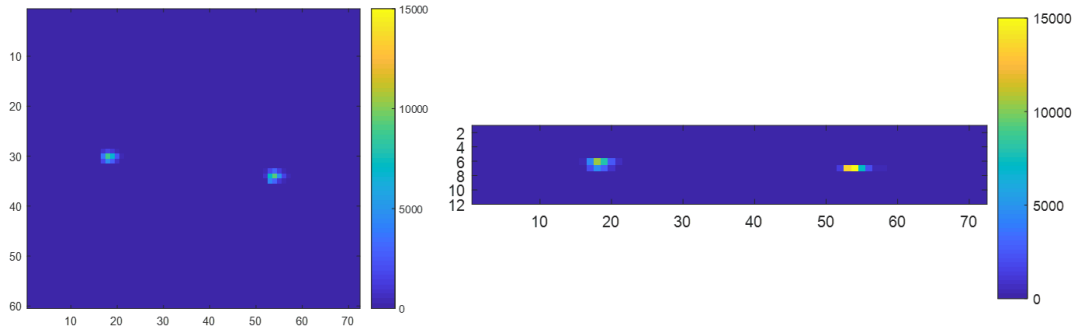

Figure 7-10: A regular readout method gives a characteristic X-ray pattern (left) whilst parallel binning combines the values in each column (right) creating another distinct pattern.

The original OGRE design featured a single arc of diffraction incident on each device with the device being oriented to match that of the dispersion angle, thus meaning the point spread function have a large variation in the y direction whilst having minimal variation in the x-direction. This would have allowed for parallel binning to be utilised assuming PSFs could be kept separate and the observed flux is sufficiently low that multiple events in the same place are low and thus saturation is avoided. With the new design, PSF's are now oriented at 30° meaning the y-position of the event is now of importance and so implementing parallel binning would reduce the energy resolution of the system. Whilst this will mean reading additional pixels and giving a shorter integration time, the resolution

is maintained allowing for a more accurate spectrometer. The readout time difference is small in comparison to a single frame operation and so very little data is likely to be lost when operating in this mode.

7.6 Timing resolution

Whilst ensuring the correct voltages are applied for operating the devices, it is also the timing of the voltage applications which allows for optimal running of a CCD. Ideally, the most amount of time spent creating an image will be in the step where the image is acquired, or the integration step, reducing the number of out of time events. The image acquisition time must be maximised against that of the other procedures needed in device operation however each of these additional steps are also key to ensuring the image quality is adequate so whilst reducing the amount of time on each step is desirable, it must be done in a manner which does not resolve in a quality degradation. To allow for an adequate pointing accuracy of the system, an image acquisition of 1Hz is desired by the OGRE team to check the system is operating as planned and for action to be quickly taken if needed.

7.6.1 The operational sequence of capturing an image

The process of generating a frame from the OGRE camera requires many millions of quick operations which must be carried out to keep the charge in discrete packets with care taken to ensure each pixel element is kept as is for the whole process. Figure 7-11 shows the process of reading out frames. Each operation, i.e. the steps in the clocking sequence which changes the voltages on the device, takes 15 ns, including the ‘no operation’, or NOP, command which is used to space out the operation of the system to ensure each voltage change occurs before moving onto the next step. These NOPS are also useful in spacing out the sequencer to ensure the previous command has been carried out and the effects of that have been implemented within the device before the next step is implemented.

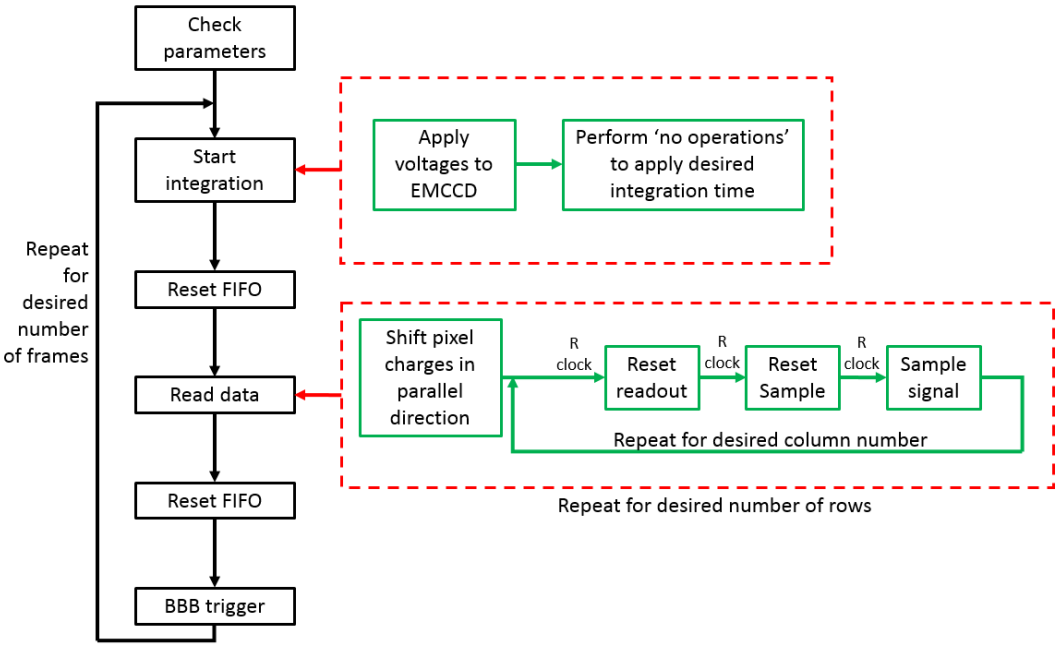

Figure 7-11: A flow diagram for the generation of frames in an EM-CCD

Keeping in mind that the devices used feature 1632 by 408 pixels and the readout requires an optimal 3 readout clock shifts per pixel, a minimum of 2 operations for each parallel shift (the first to move the charges over the pixel boundaries, the second to move into the next pixel) and 4 operations to transfer the pixel charges through the serial register and the number of operations can be seen to quickly add up (taking these numbers would give 60 ms just for the readout steps of all the pixels, not including the First In, First Out (FIFO) resets which aid in organising the manipulation of the data structure, and BeagleBone Black triggering). The addition of no operations to ensure the voltages are set at each of these points further increases the time taken by a large factor (e.g. two no ops would give 180 ms) and as this generally acts favourably in reducing charge loss between pixels is a desirable thing to keep. Thus if we are operating with the intention of generating one frame per second, the time to readout the image starts to take up a large percentage of our given time, e.g. with the 180 ms readout, we now have a maximum of 820 ms to collect photons from the source (if we could ignore FIFO and BBB triggering), and this cuts our actual observing time down further from the 3-6 minute window OGRE has.

For the standard readout sequence with the OGRE camera system with 2 ‘no operations’ implemented to allow for maximum integration time as well as the 1 Hz readout rate, it was found that the integration time needed to be set to ~500 ms. The uncertainty is due to differences in the processes carried out with the resets and triggering but this value generally gave 60 frames per minute when operated over periods of time like those used on the OGRE launch.

7.6.2 Effects of windowing and parallel binning

Windowing the device reduces the effective number of pixels to readout by altering the sequencer to only operate the readout sequence over a desired section of the device array. This allows the undesired pixel values to be dumped without being signalled. The readout is held open and the charge packets moved without clocking to empty out the register. Therefore, if we wanted to miss certain rows from our final image, each unwanted row is now moved through the system without the readout clocks on each pixel, reducing the amount of time spent on that row. This allows the time spent integrating to be increased, however the degree this can be done varies with the desired image size.

Whilst the time per final pixel has now increased, the reduction in overall time allows for the integration time on each desirable pixel to be increased allowing for more data collection. This is therefore a viable option when working with a spectrometer if the arc of diffraction allows for a simple cropping of the image area to be carried out without removing useful data.

With the OGRE prototype camera using a window the integration time could be increased to 620 ms whilst maintaining a 1Hz readout rate (60 images over one minute). Utilising the parallel binning with 10 vertical pixels combining into one allowed for an integration of 710 seconds at 1 Hz image generation rate. Whilst this method does allow for an increase integration time, the spatial data is lost and so can only be of use in very specific scenarios.

7.7 Summary

Whilst the iron-55 X-rays are of a greater energy than those OGRE intends to observe, the nature of the gain observed in these tests suggests the EM-CCD can detect the soft X-rays from Capella. The flight camera will benefit from higher quality detectors built upon the same architecture as the CCD207-10 so the so temperature dependence and the effects of varying the gain via changing RΦ2HV should be like that seen in this thesis. The noise and dark signal observed in the prototype system will also be less than reported in this section. Whilst a dark signal of $1.6e^-$ was observed here with a gain voltage of 43 V the final flight camera will have a better device which should already give a lower value than this as well as potentially operating at a greater gain voltage as the reduced energy of the photons will not see saturation occur at the same gain voltages observed when using iron-55 as a source.

The prototype systems timing will also be improved upon. The larger image sections of the CCD207-40 will require a longer readout time than that seen with the CCD207-10 reducing the integration time available further. The motherboard operation of the prototype camera will be further developed to allow for faster operations away from the detectors (FIFO resets and the BBB connections being the largest unknown area of time lost). Once a more precise focal plane is known the windowing of the devices will also greatly benefit the amount of time spent on collecting photons.

With the two gratings modules arranged at angles to each other and the y-component of the X-rays position being of importance its highly unlikely that any form of parallel binning will be utilised but if needs be it could be employed to further reduce the readout time as well as applying windowing.

8 X-ray event detection and data construction

For a large part of the project the EM-CCDs were going to be operated with parallel binning in use on the detectors due to earlier designs making the x-dimension the only value of real use for finding the photon energy. The exact number of pixels to be binned into a single output pixel had not been determined but it was likely to be 5- or 10-pixel binning. With the design overhaul of the OGRE project the idea of parallel binning has been scrapped as it is important to know the y position of the incident X-rays to better determine which of the two diffraction arcs incident on a device the X-ray is from.

Most of the event processing work focused on how these detections could best be done with binned data and was later edited to be used on a standard 2D image output. The results of both the binned and un-binned detections will be discussed in this section as well as differences in the two algorithms created.

8.1 Conditions for valid X-rays

Depending on the circumstances of an X-rays arrival at the detector surface as well as the method of operation being used on the detector itself, X-rays can appear in a variety of formats in the final acquired image. It is therefore important to look at each scenario to allow for the algorithm to correctly identify as many X-rays as possible.

8.1.1 Bright ‘central’ events

Most of the X-rays that will be observed will have the appearance of a bright central region with a fairly uniform charge distribution around this centre pixel (Figure 8-1, left). Of all the types of event to detect these have the most well-defined and characteristic properties to look for. It is generally assumed that the X-rays incident on the device will have an interaction depth in the silicon which means the charge packet does not diffuse to a great extent before being held under the electrodes.

When parallel binning is used (and assuming the entire event is binned into a single row) a line of pixels with a bright centre should be observed with significantly lower signals in the binned pixels above and below the event (assuming there are no other nearby local events), as can be seen on the right in Figure 8-1.

Figure 8-1: Example of an ideal X-ray readout on the CCD207-40 for a standard image output (left) and a binned image (right) showing the bright pixel (yellow) surrounded by some charge (light blue) larger than the background (dark blue).

8.1.2 Events split by pixel boundaries

If an X-ray interacts near the boundary between pixels then there is a good chance the charge will be fairly evenly split between the pixels. This smaller charge per pixel makes the event harder to observe over the image background however the combined charge of the split event should still be approximately that of a bright central event.

It is therefore important to ensure that the minimum threshold that is checked as a possible X-ray account takes the split into account for the lowest energy to be ideally observed. In this case if an X-ray were incident at the corner of four pixels and the charge distributed uniformly to each of the four pixels, the lowest threshold would be defined as a quarter of the predicted observed value for the least energetic event. Whilst this will

increase the number of pixels which are analysed as part of the event detection process this would maximise the number of potential X-rays to be observed. Care must also be taken to ensure that the same event is not counted multiple times. Checks are therefore put in place to ensure that the event is only output as an X-ray if the pixel has the largest signal in the local region. In the rare event of equal values, the top-leftmost pixel is prioritised as the event pixel.

With a standard output this type of event can occur between rows and columns and will give the same effect (Figure 8-2, left) however with parallel binning this situation will only arise in this manner when the charge is split between columns in the same pixel binning range (Figure 8-2, right). If the X-ray is incident between rows which border where the parallel binning occurs then a separate, unique event style is introduced to the algorithm.

Figure 8-2: An X-ray event split between columns in a standard output image (left) and a parallel binned image (right).

8.1.3 Events between parallel bins

With the standard output being able to define individual rows and columns, the position of an X-ray on the device should not cause any major issues. When parallel binning is utilised errors can occur between these parallel boundaries due to the charge of multiple rows being combined Figure 8-3. In the example seen in Figure 8-3 the X-ray event is distributed

mostly across three different pixels; a bright pixel, a neighbour in the serial direction, and a neighbour in the parallel direction. When binned the same pattern can still be observed due to the binning procedure missing some of the X-ray events and combining only background signal to the X-ray signal.

To ensure these events are still counted when using parallel binning the event detection window must consider the rows above and below the analysis pixel and ensure any charge that may have been split off is recorded.

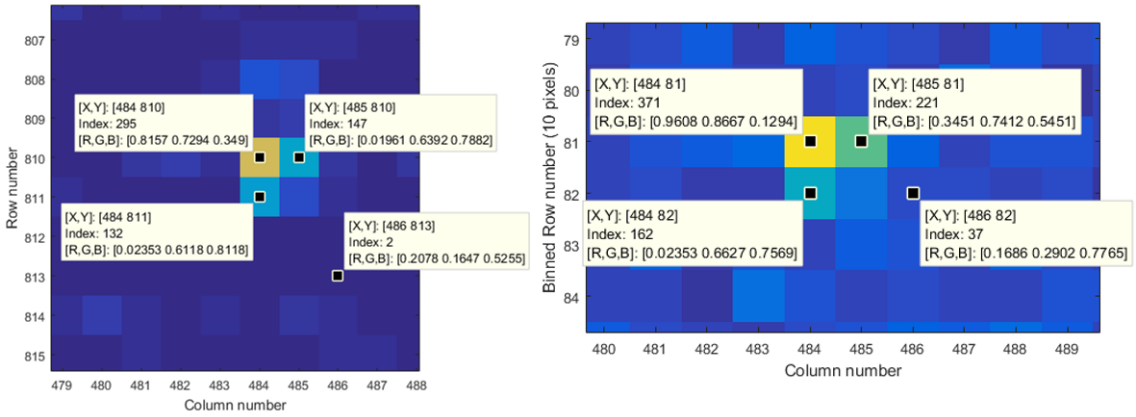

Figure 8-3: An event occurring at a parallel binning boundary as seen in a standard output image (left) and a parallel binned image (right) along with a pixel's data points (black dots) showing the pixel positions, values/index, and colour scale values. The binned image was generated by artificially binning (10 rows) the standard output image seen in this figure.

8.2 Strontium-90 events

The data catalogue for the strontium-90 tests includes four source presence types; a background count with no sources pointed towards the devices, an iron-55 source only directed to the device, a strontium-90 source only, and both the iron and strontium. The ideal analysis on each of these catalogues would be that an X-ray finding algorithm detects no events in either the background or strontium data sets and a roughly identical number in the iron and both source data catalogues. It is therefore important to know what the

strontium events look like to ensure there is enough distinction between the two event types.

8.2.1 Spectral comparison

Checking the spectrum of the iron-55 (Figure 8-4) and Strontium-90 (Figure 8-5) shows one area of concern with differentiating between the two, the overlapping of the spectral peaks. Whilst iron-55 has a very distinct, characteristic peak due to a well-known decay process, the strontium signal is incredibly broad and varied as it is a measure of interactions within the EM-CCDs silicon as a highly energetic particle passes through the medium. It is therefore clear that deeper analysis will be needed to separate these events rather than just using energy thresholds. It is therefore important to compare how each source presents itself in the images created.

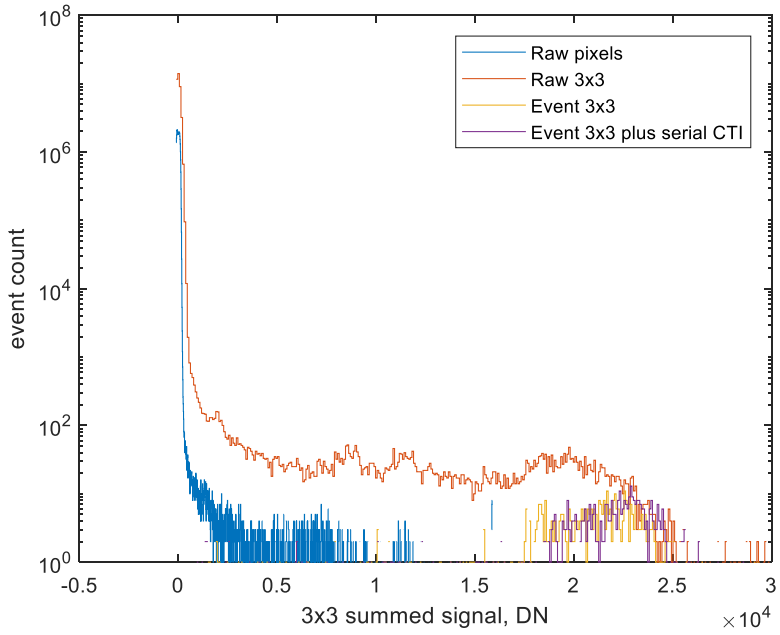

Figure 8-4: Spectrum of Iron-55 data with individual raw pixel values (blue), 3x3 window values (orange, one 3x3 window centred around each pixel), the found event values (yellow), and the event values with a Charge transfer Inefficiency correction value (purple, CTI issue explained later) at a temperature of -90°C and a gain voltage of 44V using 27 frames.

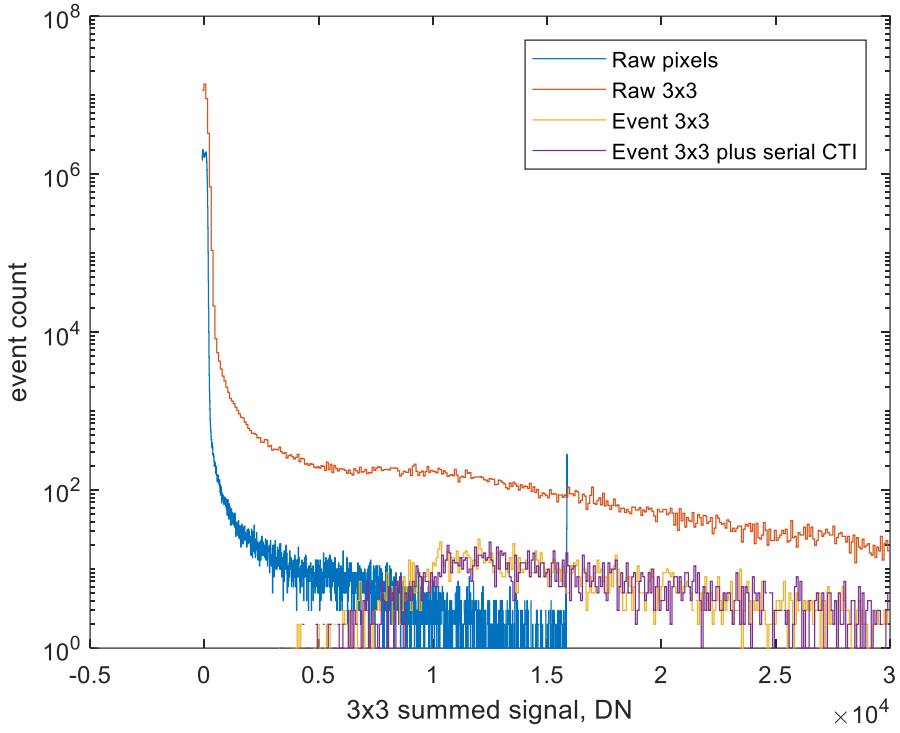

Figure 8-5: Spectrum of Strontium-90 with individual raw pixel values (blue), 3x3 window values (orange, one 3x3 window centred around each pixel), the found event values (yellow), and the event values with a CTI correction value (purple) at a temperature of -90°C and a gain voltage of 44V using 27 frames.

8.2.2 Event Comparison

Comparing both event types under identical operating conditions (a temperature of -90°C and a gain voltage of 44.2V in the following 2 figures) allows for a direct comparison of the events (Figure 8-6 and Figure 8-7). These figures were acquired using an event finder operating at a minimum detection value within a 3x3 window to ensure any spurious background signals were not misidentified.

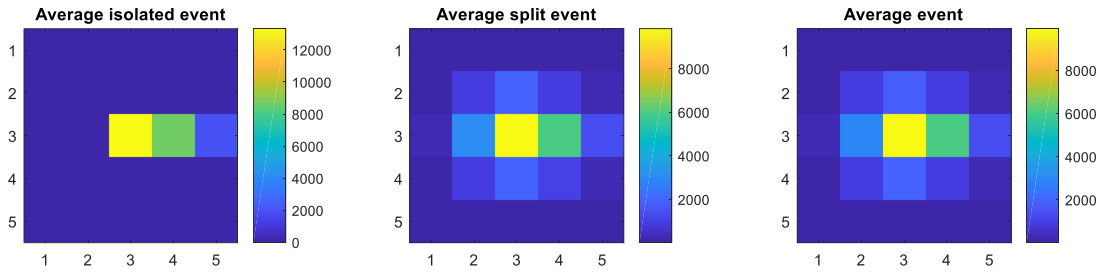

Figure 8-6: The average image output of an iron-55 X-ray detection when running at -90°C and with a HV of 44.2 V

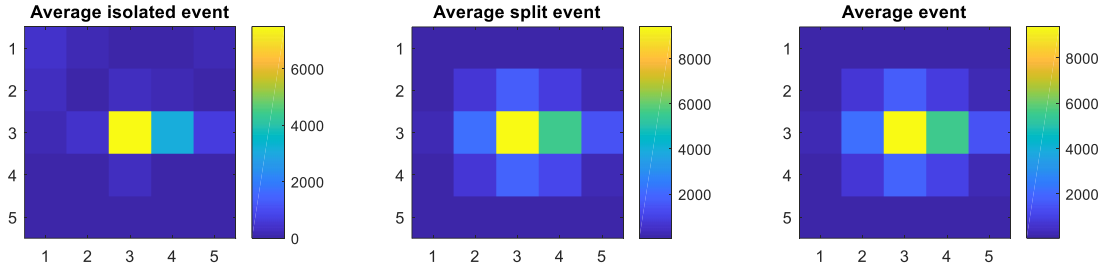

Figure 8-7: The average image output of a strontium detection when running at -90°C and with a HV of 44.2 V

Whilst not immediately apparent the isolated event signal of the average Iron-55 X-ray is sufficiently greater than that of the strontium event which also has a noisier looking background. This gives an additional testing criterion which could be used, a comparison of the central pixel value to the surrounding pixels.

Plotting the central pixel value against the ratio of the central value to the 3x3 signal gives Figure 8-8. It can be observed that the strontium events are incredibly varied, populating a large expanse of the plot area. The iron-55 however displays a curve demonstrating the split events at the lower central pixel ranges and a cloud at higher signal values where the isolated events are observed.

This curve should allow for an additional criterion in the event detection algorithm. In the case of detecting iron-55, the curve equation (with some degree of error) at a given

temperature and HV value could be used to reduce the chance of mismatching a strontium event for an iron X-ray.

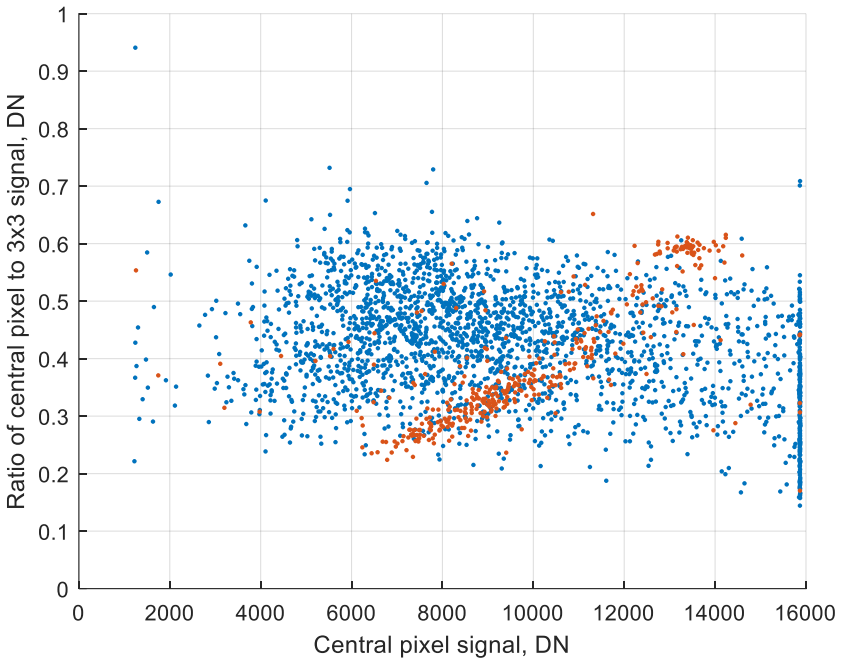

Figure 8-8: Comparison of the central pixel value to the surrounding pixels with an Iron-55 source (orange plots) and strontium source (blue points). The levelling of the data around 16000 is due to the device output reaching saturation.

8.2.3 Observed Charge Transfer Inefficiency (CTI)

The previous 3 figures demonstrate some CTI which is less than desirable. Ideally the isolated events seen in Figure 8-6 and Figure 8-7 would only feature the one bright 'isolated' central pixel but a clear trail can be seen going towards the later columns. Similarly the plot in Figure 8-8 should feature the isolated event cloud at a ratio value closer to 1, rather than the 0.6 seen.

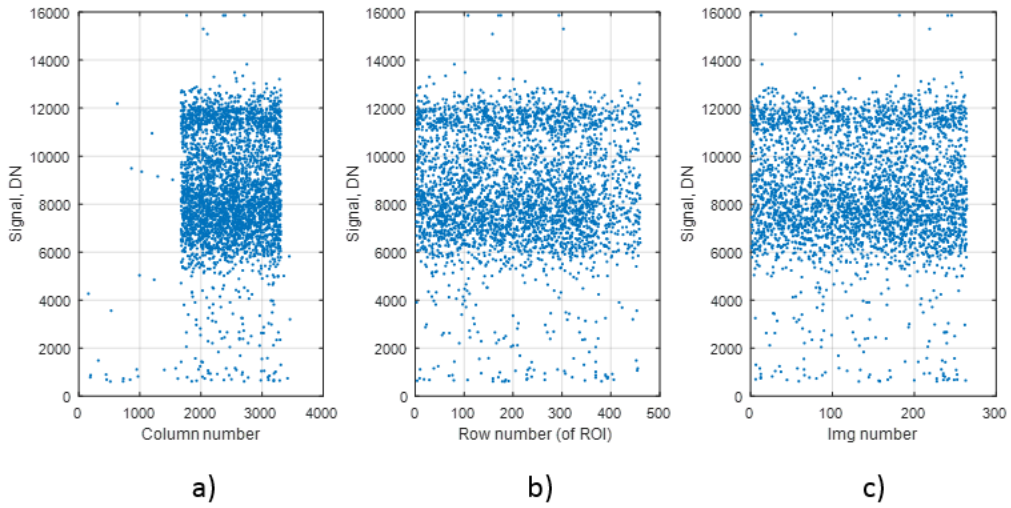

Figure 8-9: Plots of detected iron events vs: a) the column number, including the large under-scan region, b) the row number, and c) the image in the data catalogue used where the events were found.

Creating scatter plot of the event signal vs the positions of the events within the image area and the data catalogue produces Figure 8-9. Typical CTI would demonstrate a reduction across one of these plots as the efficiency of transfer decreases, appearing as a diagonal trend in any of these plots. These plots do not suggest CTI as the distinct thinner line for the isolated event style and the thicker split event regions both seem consistent across the figures. It is therefore speculated that the transfer issues occur outside of the image section of the device and somewhere along the readout path.

Whilst looking for a way to more precisely define the Iron-55 events the summed 3×3 signal of an event was compared to the ratio of the central pixel to the surrounding pixels for varying gain voltages (Figure 8-10). This should give a fairly vertical plot for each different voltage as the only variation in the x-direction is due to variations in the total X-ray energy. The figure instead suggested that at higher gains, the split events had an overall greater energy than the isolated events (see the green 44v plots in Figure 8-10). This could only occur if the charge within the multiplication register was not being properly

transferred, and so future work should be done to ensure the sequencer reduces the likelihood of CTI occurring in this section of the device.

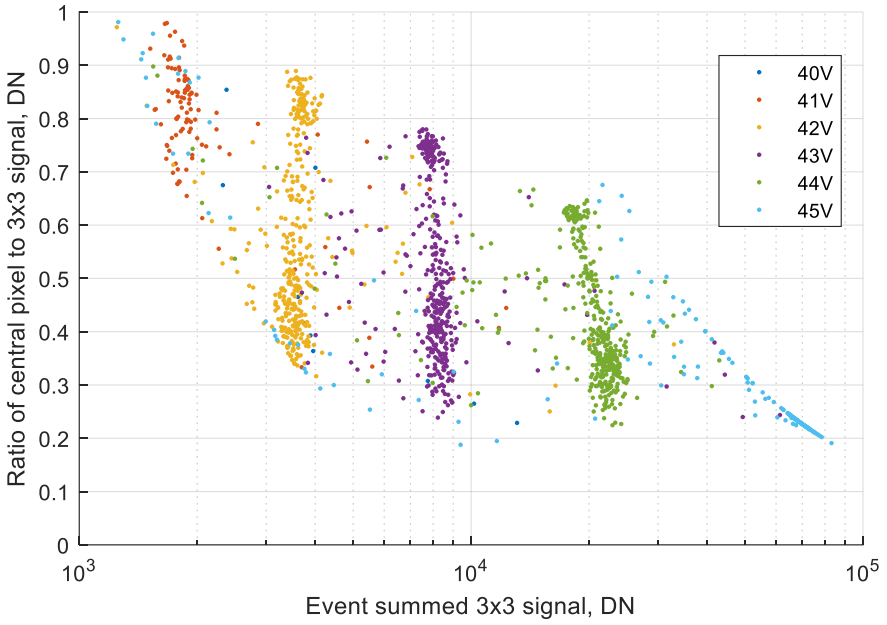

Figure 8-10: Plots of the event summed signal vs the ratio of the central pixel value to the summed event at varying gain voltages. The curve of the 45V data is due to saturation.

8.3 Implementation of the detection algorithm

The detection algorithm must follow a strict set of rules to correctly identify the X-rays and reduce the chances of a false detection. To maximise efficiency, the algorithm looks for the most obvious signs that the data is unusable first before heading onto the more technical requirements to determine an X-rays' presence. The overall processes used by the algorithm can be seen in Figure 8-11.

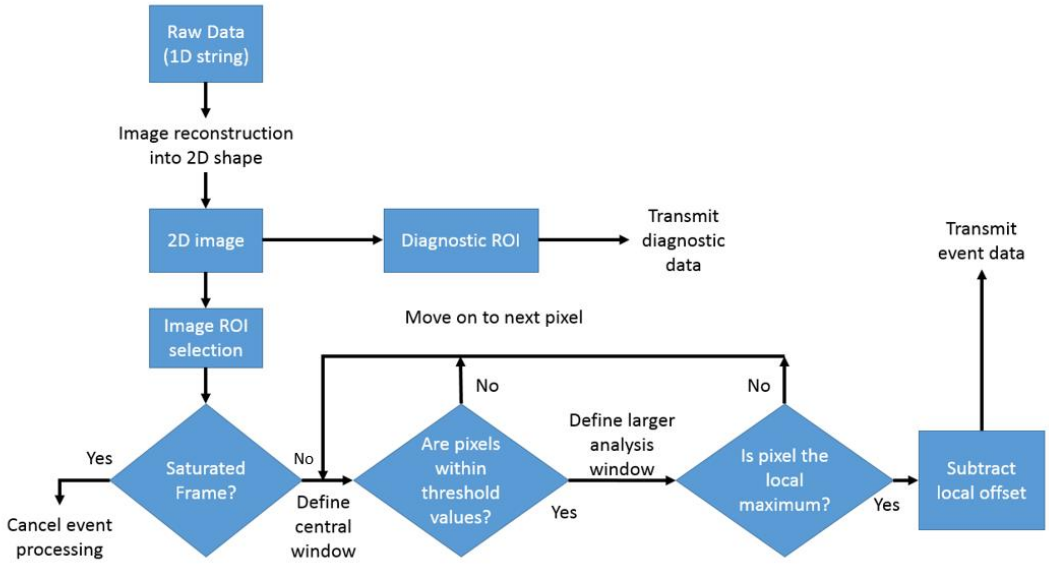

Figure 8-11: Flow diagram of the OGRE event detection algorithm.

8.3.1 Image reconstruction

The data is read out as a 1D string of pixel values so some processing is required to obtain the 2D image we require before the algorithm can be effectively used. As the image size is known this is a straightforward process which takes little time or computational power.

8.3.2 Regions of Interest (ROIs)

The total 2D output includes additional rows and columns which are used to identify noise within the image. The regions of interest are therefore the serial and parallel over-scans and under-scans, and the main image area at this point in the algorithm. Values from the serial over-scan are used to determine the amount of readout noise added to the image pixels and so a mean over-scan value is subtracted from each image section pixel to bring their values closer to that of the incoming photons effects.

8.3.3 Saturated Frame check

In the extreme case that the detectors are exposed to an exceptionally bright source (a possibility while the rocket is still orientating to Capella) the overall signal on the image will be very large. Checks on the mean of the image area values will allow a quick check on

whether the frame is usable for X-ray analysis or has been exposed to some other photon source which deems the frame unusable for analysis.

8.3.4 Define central window and threshold check

The pixel to be analysed is assigned an initial window of its local pixels (3 columns on 1 row for the binned algorithm, 3x3 for the un-binned algorithm), with the analysis pixel at the centre. A low value threshold is used to determine the minimum value a pixel can have to be classified as a possible X-ray. The analysis pixel value is checked against this threshold value with a pass/fail system being used to see if the algorithm continues. If the value is large enough, the local pixels are also checked along with the analysis pixel.

If the total values of all the pixels in the initial window are too high then the signal is likely to be from a non-target source, i.e. a cosmic particle traveling through the device. This high threshold value is based on the gain of the system and set based on the energy range being observed. With the OGRE energy range, we are hoping to see X-rays with a maximum of 1200 eV so a signal equating to a more energetic photon is clearly outside the OGRE energy range and thus from an undesirable source.

8.3.5 Local maximum check

The high threshold can allow for multiple bright pixels within the initial window and for it still to be a valid X-ray event. To ensure that each of these bright pixels are not classified as their own X-ray a local maxima check is established. To potentially be an X-ray location pixel, the analysis pixel must have the largest signal in its local 3x3 environment (the analysis window is expanded in the parallel binning algorithm to account for this). With the expected photon count on each device expected to be low there is little chance of an event pile-up so this 3x3 exclusion factor is unlikely to misidentify two X-rays as a single event.

8.3.6 Comparison with the local offset

The window around the analysis pixel is expanded again (to 5 columns by 3 rows for the binning algorithm and 5 columns and 5 rows for the standard output algorithm) to allow for checks in the events value compared to its region on the device. The median value of the border pixels (Figure 8-12) is taken and compared to the value of the event pixels, here treated as the sum of the pixels found in the earlier high threshold check. The median is used to allow two X-rays to fall close to each other (outside of the 3x3 region around the analysis pixel) without causing a failure at this step. This allows a distinction to be made regarding the possible source of the event being analysed. X-ray events are expected to be small and self-contained whilst cosmic events will likely produce larger signals if they pass through the detector mostly perpendicular to the detector, or streaks if passing through at an angle. This check should mitigate falsely detecting either of these cosmic style events as an X-ray.

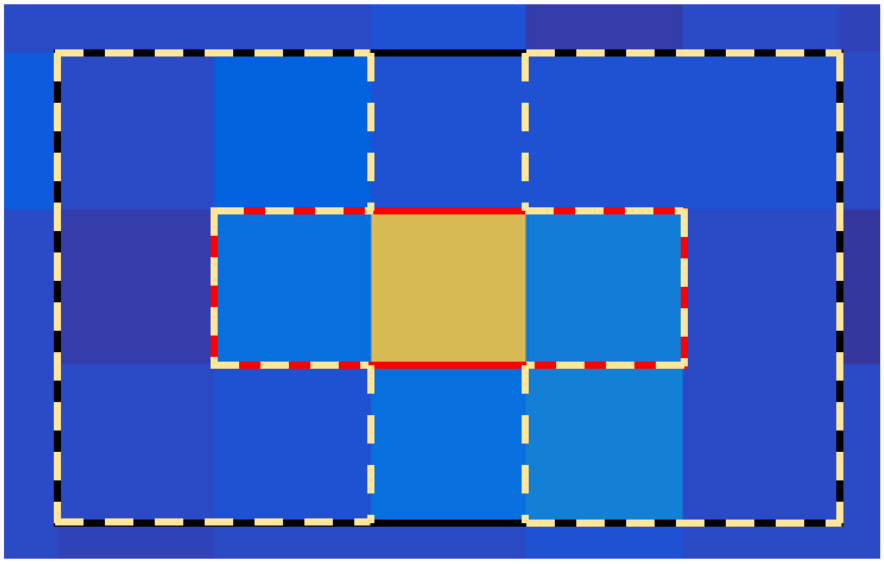

Figure 8-12: Analysis window for the parallel binning event algorithm. The red box shows the initial window where the high threshold check takes place and the regions bordered by a white dash are the pixels used to find the local offset.

8.4 Parallel binning with gain

A benefit of using an EM-CCD for the OGRE cameras is that the charge packet generated by a photon within the device is multiplied before the readout noise is added effectively negating its impact and giving a better signal to noise ratio. Any dark signal within the device background is still multiplied though so the gain is still a factor affecting the noise in the image.

When parallel binning it is important to remember that the binning applies before the multiplication register and thus is a larger, combined charge than that seen in standard readout before the gain has an effect. It is therefore apparent that as the gain increases the deviation in the background values is likely to increase accordingly. If the X-ray energy is sufficiently large than the background this should not prove to be a problem, however in the interests of the project it is a factor which should be investigated.

Another factor to look out for is event pile-up within a bin. If 10-pixel binning is applied multiple events could be condensed down into a single pixel, the resultant charge packet being larger than that of a single X-ray event. When put through the multiplication register there is a greater chance of this exceeding the full well capacity of the pixel or exceeding the capabilities of the ADC. If the only required output from the device was therefore the x-position along the device, as in a previous OGRE design, the number of pixels to bin should be planned carefully to ensure proper device operation is possible without negatively impacting the results.

8.5 X-ray counting with varying gain

A variety of issues surround the accuracy at which X-rays are observed as the gain increases. For a given experimental setup it can be assumed that if the arrangement of the equipment is not changed the count from the source should be fairly constant across all

tests, i.e. the number of photons that are incident on the device does not vary. As the gain on the device increases the number of events readily observable will increase until it reaches this approximate constant value. As the gain increases further it is possible that false matches could be made by the event algorithm where background signal that has undergone a large gain could be misidentified as an X-ray. The ideal scenario is therefore that as the gain increases the number of observed events increases until it plateaus and does not increase any further. Ensuring this characteristic is observed in the device is one key check to ensuring an accurate count rate.

8.6 Constructing the telemetry strings

One thing of great importance is being able to send the data from the rocket to the ground via telemetry to ensure the data collection is proceeding as planned. The telemetry can send only a finite amount of data per second so care must be made to ensure there is not a data pile-up in the telemetry stream.

8.6.1 Camera data rate limitations

The baud rate of the camera is the number of bits that can be sent out per second and may limit the amount of data that can be telemetered. This is known to be 57.6 kb/s on each RS422 output on the OGRE camera.

The BBB's Universal Asynchronous Receivers/Transmitters (UARTs) have a maximum programmable baud rate of 3.68 MHz with a line driver/ buffer specified up to 20 MHz. The output buffer size on each BBB is set up to be 600 bits.

The WFF93 telemetry stack can handle between 78 kb/s to 10 Mb/s so could potentially handle maximum capacity readouts from each of the four event RS422 channels of the OGRE camera.

The BBB processor has FIFO Buffers for Transmit and Receive (256 Bytes). If this applies to the RS422 UART then using a very slow transmit speed with high event processing speed should stack all the X-ray events in the FIFO for transfer without causing any issues.

Currently the design of the OGRE camera allows for a telemetry channel for each of the detectors with a maximum transfer rate of 78 kb/s. This accommodates the 57.6 kb/s each RS422 can output which is the limiting factor in the complete telemetry system.

8.6.2 Frame number

A unique number should be given to each frame read out by the detectors. The OGRE camera will operate for 15 minutes before the launch and then approximately 30 minutes of flight time whilst operating with a readout of 1 Hz giving a total of 2700 frames. 12 bits of data can be used to define up to 4096 unique frame numbers.

8.6.3 X-ray position

The position of the X-ray Analysis Windows in the CCD, i.e. the central pixel and X-ray location, must be communicated. The maximum image size will have 1648 columns and 1608 rows for a total of 2,649,984 pixels, of which the photons could be detected over any of the 2,560,000 image pixels.

The row and column number will be sent individually in 11 bits (allowing a value up to 2047). If the row and column numbers were combined and only the position of the X-ray Analysis Window in a 1D array was communicated, the position could be encoded within a 22-bit string (up to 4,194,303). Therefore, column and row numbers will be sent separately to allow for more convenient processing on the ground into useful data.

8.6.4 Event data

The pixel values of an X-ray Analysis Window will be sent to the ground for data return. The camera has a 14-bit output range. A nominal choice is to transfer every pixel value from

the 3x5 Analysis Window, equivalent to 15 pixels or 210 bits. Knowing how the output string is created allows the image to be reconstructed on the ground without having to send the x co-ordinates of each pixel along with its value.

8.6.5 Cyclic Redundancy Check (CRC)

A CRC can be performed and appended to the end of the string so that the validity of the data string can be checked after being telemetered. The CRC is calculated using the contents of the event string. The CRC length has been nominally set at 16 bits. There is an option to not include a CRC at all, but this could be considered bad practice.

8.6.6 Total string length

Combining all these sections of the string gives an overall event string per event of length 257 bits (Table 8-1).

Table 8-1: Breakdown of the OGRE event string outputs and the required bit lengths

Section	Number of bits required
Frame number	12
X-ray position (x and y co-ordinates)	22
Event pixel values (10x5 image)	210
CRC	16
Total length per event	260 = 32.5 bytes ⇨ 33 bytes

If the OGRE camera were to detect the expected 2000 X-rays over five minutes there would be an average of 6.7 events per second equating to roughly 1.742 kb/s, a rate that is significantly less than the telemetry stack and camera output rates (8.6.1). The system therefore allows a maximum of 221 events to be output per device per second which greatly exceeds the expected flux.

A limit on the number of events to be sent to the ground may have to be implemented. If an exceptionally large number of events were detected due to an error in the detection algorithm it is possible that event data could exceed the output rate per second required. A condition will therefore be implemented preventing excessive numbers of events being sent, e.g. a maximum of 200 events per second, with a warning passed to the ground when this cut off has been applied.

8.6.7 Fourth detector checks

The fourth detector does not have a fixed purpose yet, with it being used to calibrate X-rays using an iron-55 source during the flight, or to observe the optical photons incident on it to ensure the alignment and pointing are reliably accurate. Regardless of what the detector observes the same string structure as used on the X-ray event outputs will be used as they will still be able to send the useful data back to the ground without impacting the telemetry system.

8.6.8 Diagnostic String

The OGRE camera motherboard can also output and receive certain values via the telemetry system. It is possible that the operating parameters and voltages could be controlled from the ground via the telemetry system in case the values need to be adjusted mid-flight (e.g. changing the gain voltage due to a drastic change in the temperature). The actual details of a diagnostic string can be implemented at a much later time when it is known exactly which outputs/inputs are desired.

8.7 Summary

The understanding of how X-rays appear within the EM-CCD image area is paramount to a live analysis during the launch of OGRE. The spectrometer nature of the payload means most signals observed by the devices will be due to the X-rays which successfully passed through the mirror and gratings modules and the chosen optical blocking filter. It is

therefore the more extreme, and unlikely events that will need to be ruled out if they happen to occur during the flight.

The event detection algorithms have shown they care capable of finding the key features of an X-ray event and the tests with the strontium-90 and iron-55 have demonstrated that utilising a ratio between the central pixel and the surrounding pixels allows for a well-defined characteristic curve of a given X-ray energy. As the X-rays incident upon the OGRE camera should be in known positions due to the photon energy and the gratings modules it is therefore possible to add conditions to the event detections where this ratio and the central pixel value must fall within certain limits to be a Capella photon incident upon a given region of the image section. Further understanding of the expected focal plane would be needed but on ground testing prior to the flight could allow for this to be implemented.

The sending of findings to the ground via telemetry should be of little issue however the exact usage of the fourth detector is still to be determined. A further event algorithm may be required to monitor where on the device the optical events are upon the fourth detector which in turn could be used to send back data on the rockets pointing accuracy, information which is highly desirable to prevent loss of data collection due to misalignments of the system with the target.

With the low expected flux of the system and an on-board processing unit for each of the flight detectors the OGRE camera should be capable of fast analysis throughout the flight time with no data pile-up and useful information to be fed to the ground team for the duration of the launch day.

9 Conclusion

The main research aim of this thesis was to determine if the EM-CCD camera proposed for the OGRE project would be suitable for use in an X-ray spectrometry payload. Modelling and testing have suggested that the mission could benefit from this systems usage.

9.1 Model of the payload

The model was created using ideal conditions with further expected inaccuracies to be introduced later to give an idea of the expected number of X-rays to be observed. The model highlighted several things:

- Silicon is very effective for use in soft X-ray mirrors however the nature of manipulating X-rays makes large collecting areas a difficult issue.
- The off-plane gratings are of a significant improvement over previous grating systems and the current system works efficiently for the OGRE energy region.
- An optical blocking filter should be utilised as it is not the main limiting factor in the reduction of X-ray count and its capabilities of preventing large energy photons which could be detrimental to the device's operations should not be overlooked.
- The given system overall is a significant improvement over prior systems, like Chandra, with the main crux being the reduced observation time due to the nature of sounding rocket missions.
- An increased collecting area to make up for the reduced time should allow for a successful mission.

These results were directly used to allow for a redesign of the OGRE system. Further developments of a model are to be carried out later with the added advantage of utilising ray tracing to give a better idea of flux reduction due to misalignment. The fact the ideal model did not meet the minimum success conditions was of some great concern however

the production of a new design still using the three key technologies originally intended for use in OGRE should see a successful mission launch.

Outside of the scope of this thesis but still related to this new design;

- The optics generated by NASA's Goddard Flight Facility have already seen advancements in fabrication and accuracy since the model discussed in this thesis was initially created. These new optics offer increased structural rigidity allowing a greater collecting area by support reduction and a thinner reflecting medium.
- The team at Penn State University continue to test the diffraction gratings they produce improving upon their grating accuracy and production quality with every iteration. With further sounding rocket missions carried out frequently their expertise in mission preparation will only develop positively and with a greater understanding on the craft limitations and mission structures, their learnings will be implemented in all their future projects, increasing their reliability, and reducing the risk of an unsuccessful launch.

9.2 The EM-CCD camera

The testing of the prototype camera system in laboratory conditions to determine its suitability for soft X-ray observation found that the camera system, once fully optimised for the specifics of the launch payload design, should be capable of allowing the observations of the Capella x-ray spectrum to accuracies not previously seen.

- X-ray events incident upon the CCD207-10 have been observed in varying conditions which will allow for finer controlling of the system to meet mission requirements.
- Gain was observed to vary significantly with the temperature of the device and the RΦ2HV voltage used. As gain is desired to be maintained at a constant value for

the duration of the project it is therefore possible to determine how the voltage could be adjusted if the temperature changes during the flight.

- The EM-register significantly reduces the effects of noise present in the device even in an engineering grade detector that is not recommended for flight use. A value of 1.6 electrons/s was observed as a dark signal at a high gain which would ideally have been a sub-electron value, however with the flight system using better devices and potentially higher gains it is highly likely the sub-electron noise will be observed on the flight camera system.
- The CCD207-10 is sufficient in terms of pixel size and image area to allow proper spatial resolution of the point spread functions expected due to the optical and grating arrangement of the OGRE payload.
- Windowing of the devices will provide a significant benefit to maximise the integration time of the system and thus reduce the number of out-of-time events which will occur during the OGRE test flight.

Overall the tests on the CCD207-10 and the OGRE prototype camera highly suggest the final flight camera partnered with the CCD207-40 should allow for good observations of the Capella soft X-ray spectrum.

9.3 Event detection

After many X-rays had been observed an algorithm capable of automatically identifying X-rays incident in the image region was constructed and tested with varying sources of signal and for different operational parameters.

- Events were observed to either be centrally focussed or split across pixels. Determining the distribution of this charge allows for a better idea of the location of incidence. Each type is very distinctive in properties and the system can pick up both events.

- Observational differences between strontium-90 and iron-55 events showed that utilising the ratio of a central testing value and its surrounding pixels can give a distinct relationship allowing for more precise determination of the observed signals source.
- Parallel binning could be utilised in some projects where exact y positions in the image area are not required, however due to the high gain nature of using EM-CCDs care should be taken not to oversaturate the device by compiling multiple large-signals into one binned pixel.

Further refinement will be needed to ensure the soft X-rays in the OGRE energy range are observed to a high degree of accuracy with positions reported to the telemetry string to allow for a good idea of the payload's performance during the flight.

9.4 Future work

The main principles which will require further testing is the exact nature of the photon dispersion upon the EM-CCDs and how the integration time can be optimised. Ideally the system will take time to read out only the pixels which are desirable for data collection allowing the undesirable pixels to be quickly dumped without taking the time to read their values. The exact nature of this will be dependent on the final arrangement of the rest of OGRE's key components and it may be possible to adjust the readout sequence to more closely fit that of the expected arcs of diffraction incident upon each detectors surface, plus some room for variance. Whilst this may save very little time per captured frame, with a maximum observational time of 6 minutes the optimisation of data collection time is a necessity.

The energy of the photons observed from Capella will also vary from that of the iron-55 and strontium-90 used in the lab. The photons used to create the current event detection system are of a higher energy meaning a larger gain voltage will be needed to observe

similar signals. This will therefore require adjustments to the algorithms to ensure the desired event energy ranges are fulfilled and may require testing at a facility which could allow for photons within the OGRE energy range to fall incident upon the devices.

The ideal operation of the camera system is for the event detection to be completed on-board the rocket during flight with any desirable X-ray detection results transmitted to the ground for a 'live' feed of the projects performance. The full data files will be saved on-board onto solid media to allow for further analysis upon retrieval. The camera system will therefore need to work with a graphical user interface on the ground to best show the telescopes current performance and would ideally allow for transmissions back to the camera system mid-flight to allow for changes to operating parameters in the event of any complications. The delicate intricacies of the OGRE camera system must therefore be further refined to ensure it meets the needs of all the teams working on this project, especially when the limited data collection time is considered.

With OGRE scheduled for launch in 2021 there are still a couple of years before the exact capabilities of each key technology is seen and their benefits in future missions will be clearer. Upon a successful launch within a couple of years upon this thesis's submission a more precise idea of the capabilities, and limitations, of each part of the X-ray telescope will be known increasing the technology readiness level and suggesting suitability for further use. EM-CCDs are already selected for NASA's WFIRST mission in the mid-2020s and the verification of this technology will likely be of interest to many participants in this project, allowing clearer ideas of how to ensure their project launch is successful.

Future missions are always in the works and whilst advancements in astronomy can come quickly upon the launch of a new mission, it takes a lot of time to ensure the instrument is ready for use in the harsh environment of space. This time means that whilst the technology on the launchpad is outdated compared to the most recent advancements in

technology, it is flying with a good deal of trust that the project will proceed as intended. The latest equipment will be picked up and tested for years before that flies on a mission by which time technology capabilities far exceeding previous missions will be available for testing. This leapfrogging of technology advancement, astronomical desires, and thorough testing should see the space industries constantly balancing a large variety of projects for the foreseeable future. In ten years', time, new devices will likely be available for X-ray observations which will build off the successes hopefully observed from large projects like WFIRST, to the smaller but still essential missions, like OGRE.

10 Bibliography

Agrawal, P. C., G. P. Garmire, G. R. Riegler, and I. R. Tuohy. 1976. “X-Ray Telescope For Sounding Rocket-Borne Observations.” *SPIE 0093, Advances in Precision Machining of Optics.* doi:10.1117/12.955122.

B.L. Henke, E.M. Gullikson, and J.C. Davis. 1993. *X-ray interactions: photoabsorption, scattering, transmission, and reflection at E=50-30000 eV, Z=1-92.* Vol. 54. Atomic Data and Nuclear Data Tables,. doi:10.1006/adnd.1993.1013.

Barry, B. L. 2008. “The evolution of concepts of colour vision.” *Neurociencias.*

Bohr, N. 1913. “On the Constitution of Atoms and Molecules, Part 1".” *Philosophical Magazine* 26: 1 - 24.

Boyle, W.S., and G.E. Smith. 1970. “Charge Couple semiconductor devices.” *The Bell System Technical Journal.*

Buck, A. L. 1981. “New Equations for Computing Vapor Pressure and Enhancement Factor.” *Journal of applied meteorology* 20 (12): 1527-1532. doi: 10.1175/1520-0450.

DeRoo, C. T., R. L McEntaffer, D. M. Miles, T. J. Peterson, H. R. Marlowe, J. H. Tutt, B. D. Donovan, B. Menz, V. Burwitz, and G. Hartner. 2016. “Line spread functions of blazed off-plane gratings operated in the Littrow mounting.” *Journal of Astronomical Telescopes, Instruments, and Systems.*

e2v technologies . 2011. “CCD97-00 Back Illuminated 2-Phase IMO Series Peltier Pack Electron Multiplying CCD Sensor.”

e2v technologies. 2006. “An overview of the ageing characteristics of L3Vision sensors, Low Light Technical Note 5.”

e2v technologies. 2007. “CCD207-00 & CCD207-10 Back-Illuminated 2-Phase IMO Series Datasheet.”

e2v Technologies Ltd. 2015. *CCD201-20 Back-illuminated 2-Phase IMO Series Electron-multiplying CCD Sensor data sheet.* Chelmsford, March.

e2v Technologies Ltd. 2004. *CCD60 Back Illuminated Electron Multiplying CCD Sensor data sheet.* Chelmsford, May.

Evagora, A M, N J Murray, A Holland, D Burt, J Endicott, and ,. 2012. “Novel method for identifying the cause of inherent ageing in Electron Multiplying Charge Coupled Devices.” *Journal of Instrumentation* 7. doi:https://doi.org/10.1088/1748-0221/7/01/C01023.

F. Jansen, D. Lumb, B. Altieri, J. Clavel, M. Ehle, C. Erd, C. Gabriel, M. Guainazzi, P. Gondoin, R. Much, R. Munoz, M. Santos, N. Schartel, D. Texier and G. Vacanti. 2001. “XMM-Newton observatory.” *A&A Volume 365: First Results from XMM-Newton.* doi:10.1051/0004-6361:20000036.

Gaetz, T.J., and D. Jerius. 2005. *The HRMA User's Guide.* Cambridge: Chandra X-ray Center.

Gaskin, J., R. Elsner, B. Ramsey, C. Wilson-Hodge, A. Tennant, S. Christe, and A. Shih. 2015. *SuperHERO: Design of a new hard-X-ray focusing telescope.* 2015 IEEE Aerospace Conference, Big Sky, MT, USA, 2015. doi:10.1109/AERO.2015.7119097.

Giacconi, R. 2003. “Nobel Lecture: The dawn of x-ray astronomy.” *Rev Mod Phys.*

Giacconi, R. 1980. “The Einstein X-ray Observatory.” *Scientific American.*

Ingley, R, D R Smith, and A D Holland. 2009. “Life testing of EMCCD gain characteristics.” *Nuclear Instruments and Methods in Physics Research Section A: Accelerators, Spectrometers, Detectors and Associated Equipment* 600 (2): 460-465.

J. H. Tutt, R. L. McEntaffer, B. Donovan, T. B. Schultz, M. P. Biskach, K. Chan, J. D. Kearney, J. R. Mazzarella, R. S. McClelland, R. E. Riveros, T. T. Saha, M. Hlinka, W. W. Zhang, M. R. Soman, A. D. Holland, M. R. F. Lewis, K. Holland, N. Murray. 2018. "The Off-plane Grating Rocket Experiment (OGRE) system overview." *SPIE 10699, Space Telescopes and Instrumentation 2018: Ultraviolet to Gamma Ray.* doi:10.1117/12.2311813.

Janesick, J. J. 2000. *Scientific Charge-Coupled Devices.* SPIE.

Janesick, J. R., T. Elliott, S. Collins, T. Daud, D. Campbell, and G. Garmire. 1987. "Charge-Coupled Device Advances For X-Ray Scientific Applications In 1986." *Optical Engineering* 26 (2): 156-166.

Jerram, P., P. J. Pool, R. Bell, D. J. Burt, S. Bowring, S. Spencer, M. Hazelwood, I. Moody, N. Catlett, and P. S. Heyes. 2001. "The LLCCD: low-light imaging without the need for an intensifier." *SPIE 4306, Sensors and Camera Systems for Scientific, Industrial, and Digital Photography Applications II.* 178-186. doi:10.1117/12.426953.

Keller, C.U. 1995. "X-rays from the Sun." *Experientia.*

Kridner, J. 2017. *BeagleBone Black System Reference Manual.*

Lewis, M. R. F., M. R. Soman, A. D. Holland, N. J. Murray, D. Hall, D. P. Weatherill, J. H. Tutt, et al. 2016. "Development of the X-ray camera for the OGRE sub-orbital rocket." *SPIE High Energy, Optical, and Infrared Detectors for Astronomy VII.*

Li, F., and A. Nathan. 2005. *CCD Image Sensors in Deep-Ultraviolet.* Springer-Verlag Berlin Heidelberg.

Lumb, D. 2017. *Capella data from Chandra via private communication*

Mankins, J. C. 1995. *Technology Readiness Levels.* NASA, Office of Space Access and Technology, Advanced Concepts Office.

McClelland, R. S. 2016. “Meta-shell Approach for Constructing Lightweight and High Resolution X-Ray Optics.”

McCoy, J., T. Schultz, J. Tutt, T. Rogers, D. Miles, and R. McEntaffer. 2015. “A primer for telemetry interfacing in accordance with NASA standards using low cost FPGAs.” *SPIE 9601, UV, X-Ray, and Gamma-Ray Space Instrumentation for Astronomy XIX.* doi:10.1117/12.2186455.

McCoy, J., T. Schultz, J. Tutt, T. Rogers, D. Miles, and R. McEntaffer. 2015. “A primer for telemetry interfacing in accordance with NASA standards using low cost FPGAs.” *SPIE 9601, UV, X-Ray, and Gamma-Ray Space Instrumentation for Astronomy XIX* 960106. doi:10.1117/12.2186455.

Mcentaffer, R., C. DeRoo, T. Schultz, B. Gantner, J. Tutt, A. Holland, S. O'Dell, et al. 2013. “First results from a next-generation off-plane X-ray diffraction grating.” *Experimental Astronomy.*

Mewe, R. & Gronenschild, E. & Heise, John & Brinkman, A. & Dijkstra, J. & Westergaard, Niels & Schnopper, Herbert & Seward, Frederick & Chlebowski, T. & Kuin, N. 1982. “X-ray spectrum of Capella and its relation to coronal structure and ultraviolet emission.” *The Astrophysical Journal.*

Miles, D. M., R. L. McEntaffer, T. B. Schultz, B. D. Donovan, J. H. Tutt, D. Yastishock, T. Steiner, et al. 2017. “An introduction to the water recovery x-ray rocket.” *SPIE 10397, UV, X-Ray, and Gamma-Ray Space Instrumentation for Astronomy XX.* doi:10.1117/12.2274249.

Moody, I. n.d. “White paper.”

NASA Goddard Space Flight Center. 2015. “NASA Sounding Rockets User Handbook.”

Newton, I. 1704. *Opticks: or, A Treatise of the Reflexions, Refractions, Inflexions and Colours of Light.*

Pfeiffer vacuum. 2006. “HiPace 80 Operating instructions.”

Robbins, M. S., and B. J. Hadwen. 2003. “The noise performance of electron multiplying charge-coupled devices.” *IEEE Transactions on Electron Devices* 50 (5): 1227-1232. doi:10.1109/TED.2003.813462.

Rogers, T., R. McEntaffer, T. Schultz, B. Zeiger, P. Oakley, and W. Cash. 2013. “The OGRESS sounding rocket payload.” *SPIE 8859, UV, X-Ray, and Gamma-Ray Space Instrumentation for Astronomy XVIII.* doi:10.1117/12.2023762.

Rogers, T., T. Schultz, J. McCoy, D. Miles, J. Tutt, and R. McEntaffer. 2015. “First results from the OGRESS sounding rocket payload.” *SPIE 9601, UV, X-Ray, and Gamma-Ray Space Instrumentation for Astronomy XIX.* doi:10.1117/12.2183237.

Smith, P. 2016. *Thesis.*

Soesbe, T. C., M. Lewis, E. Richer, N. Slavine, and P. Antich. 2007. “Development and evaluation of an EMCCD based gamma camera for preclinical SPECT Imaging.” *IEEE Transactions on Nuclear Science* 54 (5): 1516 - 1524. doi:10.1109/TNS.2007.906408.

Stanton, A. 1896. “Wilhelm Conrad Röntgen On a New Kind of Rays: translation of a paper read before the Würzburg Physical and Medical Society, 1895.” *Nature.*

Takahashi, T., M. Kokubun, K. Mitsuda, R. Kelly, T. Ohashi, F. Aharonian, H. Akamatsu, et al. 2016. “The ASTRO-H (Hitomi) x-ray astronomy satellite.” *SPIE Astronomical Telescopes + Instrumentation.* doi:10.1117/12.2232379.

Tutt, J. H., A. D. Holland, N. J. Murray, D. J. Hall, R. D. Harriss, A. Clarke, and A. Evagora. 2012. “The Noise Performance of Electron Multiplying Charge-Coupled Devices at X-ray energies.” *IEEE Transactions on Electron Devices* (IEEE) 59: 2192 - 2198. doi:10.1109/TED.2012.2200488.

Tutt, J. H., R. L. McEntaffer, B. D. Donovan, T. B. Schultz, M. P. Biskach, K. Chan, J. D. Kearney, et al. 2018. “The Off-plane Grating Rocket Experiment (OGRE) system overview.” *Space Telescopes and Instrumentation 2018: Ultraviolet to Gamma Ray.*

Weisskopf, M. C., H. D. Tananbaum, L. P. V. Speybroeck, and S. L. O'Dell. 2000. “Chandra X-ray Observatory (CXO): overview.” *SPIE 4012, X-Ray Optics, Instruments, and Missions III.* doi:10.1117/12.391545.

Zeiger, B., A. Shipley, W. Cash, T. Rogers, T. Schultz, R. McEntaffer, and M. Kaiser. 2011. “The CODEX sounding rocket payload.” *SPIE 8076, EUV and X-Ray Optics: Synergy between Laboratory and Space II.* doi:10.1117/12.887058.